Abstract

Title of dissertation: DESIGN, DEVELOPMENT, ANALYSIS, AND CONTROL OF A BIO-INSPIRED ROBOTIC SAMARA ROTORCRAFT

Evan Robert Ulrich
Doctor of Philosophy, 2012

Dissertation directed by: Dean of The A. James Clark School of Engineering
Professor of Aerospace Engineering
Darryll J Pines

THIS body of work details the development of the first at-scale (>15 cm) robotic samara, or winged seed. The design of prototypes inspired by autorotating plant seed geometries is presented along with a detailed experimental process that elucidates similarities between mechanical and robotic samara flight dynamics. The iterative development process and the implementation of working prototypes are discussed for robotic samara Micro-Air-Vehicles (MAV) that range in size from 7.5 cm to 27 cm. Vehicle design issues are explored as they relate to autorotation efficiency, stability, flight dynamics and control of single winged rotorcraft.

In recent years a new paradigm of highly maneuverable aircraft has emerged that are ideally suited for operation in a confined environment. Different from conventional aircraft, viscous forces play a large role in the physics of flight at this scale. This results in relatively poor aerodynamic performance of conventional airfoil and rotorcraft configurations. This deficiency has led to the consideration of naturally occurring geometries and configurations, the simplest of which is the samara.

To study the influence of geometric variation on autorotation efficiency, a high speed camera system was used to track the flight path and orientation of the mechanical samaras. The wing geometry is planar symmetric and resembles a scaled version

of *Acer diabolicum Blume*. The airfoil resembles a scaled version of the maple seed with a blunt leading edge followed by a thin section without camber. Four mechanical samara geometries with equal wing loading were designed and fabricated using a high precision rapid prototyping machine that ensured similarity between models. It was found that in order to reduce the descent velocity of an autorotating samara the area centroid or maximum chords should be as far from the center of rotation as possible. Flight data revealed large oscillations in feathering and coning angles, and the resultant flight path was found to be dependent on the mean feathering angle.

The different flight modalities provided the basis for the design of a control system for a powered robotic samara that does not require high frequency sensing and actuation typical of micro-scaled rotorcraft. A prototype mechanical samara with a variable wing pitch (feathering) angle was constructed and it was found that active control of the feathering angle allowed the variation of the radius of the helix carved by the samara upon descent. This knowledge was used to design a hovering robotic samara capable of lateral motion through a series of different size circles specified by precise actuation of the feathering angle.

To mathematically characterize the flight dynamics of the aircraft, System identification techniques were used. Using flight data, a linear model describing the heave dynamics of two robotic samara vehicles was verified. A visual positioning system was used to collect flight data while the vehicles were piloted in an indoor laboratory. Closed-loop implementation of the derived PID controller was demonstrated using the visual tracking system for position and velocity feedback.

An approach to directional control that does not require the once-per-revolution actuation or high-frequency measurement of vehicle orientation has been demonstrated for the first time. Lateral flight is attained through the vehicles differing responses to impulsive and step inputs that are leveraged to create a control strategy that provides full controllability. Flight testing revealed several linear relationships,

including turn rate, turn radius and forward speed. The steady turn discussed here has been observed in scaled versions of the robotic samara, therefore the open-loop control demonstrated and analyzed is considered to be appropriate for similar vehicles of reduced size with limited sensing and actuation capabilities.

DESIGN, DEVELOPMENT, ANALYSIS, AND CONTROL OF A BIO-INSPIRED ROBOTIC SAMARA ROTORCRAFT

by

Evan Robert Ulrich

Dissertation submitted to the Faculty of the Graduate School of the
University of Maryland, College Park in partial fulfillment
of the requirements for the degree of
Doctor of Philosophy
2012

Advisory Committee:

Professor Darryll J. Pines, Chair/Advisor
Professor James Baeder
Professor Allison Flatau
Professor Inderjit Chopra
Professor Michael Coplan Dean's Representative

Contents

List of Tables

List of Figures

Nomenclature

Roman Symbols

c	Chord length
s	Span length
a, b	Fourier series coefficient
x	Inertial x location
y	Inertial y location
z	Inertial z location
u	Body-fixed longitudinal velocity
v	Body-fixed lateral velocity
w	Body-fixed heave velocity
p	Body-fixed roll rate
q	Body-fixed pitch rate
r	Body-fixed yaw rate
I_x, I_y, I_z	Principal moments of inertia
r_{CG}	Radius of precession of the center of mass
Y_C	Wing area centroid distance from center of mass
R	Length of wing
R_o	Rossby Number
Re	Reynolds Number
R_{BF}	Convert frame ($\mathbf{F}$) to frame ($\mathbf{B}$)
R_{xy}	In/out cross spectral density
R_{xx}	Input auto-spectral density
R_{yy}	Output auto-spectral density
K_d	Derivative gain
K_p	Proportional gain
K_i	Integral gain
K	Static gain
T_{pl}	time constant
$W(s)$	Heave transfer function
Y	Control output
F_G	Gravity force
F_P	Propulsive force
F_{W_L}	Lift force
F_{W_D}	Drag force

F_{CF}	Centrifugal force
dy	Differential element
A	Dynamics matrix
B	Control matrix
C	Output matrix
X	State vector
$G_p(s)$	Plant transfer function
$K(s)$	Controller
Y_d	Reference value
m	Mass of robotic samara
m_w	Mass of wing
$L(y)$	Lift per unit length
$m(y)$	Mass per unit length
Z_w	Heave stability derivative
Z_{θ_0}	Collective pitch stability derivative
$\dot{w}$	Heave acceleration
r_{turn}	Virtual body turn radius

Greek Symbols

ϕ, θ, ψ	Euler angles
β	Coning angle
ν	Signal noise
κ	Measurement model
χ	Deterministic signal
Ω	Rotation rate
ρ	Density of air
$s(\hat{\theta})$	standard error
γ_l	Lock number
γ	Flight path angle
θ_0	Control Input
λ_i	Uniform inflow
$\Theta(s)$	Collective pitch transfer function
ϵ_i	Infinitesimal quantity
$\dot{\psi}_{cg}$	Virtual body turn rate

Acronymns

MAV	Micro Air Vehicle
PID	Proportional-Integral-Derivative Controller
LEV	Leading Edge Vortex
CG	Center of Gravity
MSE	Mean Equared Error

Chapter 1

Introduction

1.1 Historical Background

Observing the silent flight of a winged seed escaping its parents shadow is almost certainly a universal human experience. An encounter with one of Natures helicopters probably inspired the first manifestation of mankind's ideas of vertical flight. The earliest known concept dates back to fifth century BC Chinese tops made of feathers attached to a stick, which when spun between the hands to generate lift can then be released into free flight. The first concept of a Man carrying device would come nearly two thousand years later with Leonardo Da Vinci's "aerial screw" in 1483. It would take another 420 years for the Wright brother to make their historic flight at Kitty Hawk, and another 30 years for the first helicopter flight. Though many attempts were made at producing a vehicle that would take man to the skies, no major progress was made until aerodynamics was studied methodically and scientifically by Sir George Caley in 1804. Inspired by nature he studied the cross sections of bird wings and as early as 1808 studied the flight and geometries of samara's of the sycamore tree [1].

Otto Lilienthal, a german civil engineer, made important contributions to the development of modern aircraft controls through his work on pilot controlled gliders.

He designed, built and tested eighteen different models of gliders, and ultimately provided the inspiration for the Wright brothers to invent the first airplane. The systematic use of scaled models to converge on optimal aerodynamic properties for full size prototypes is the method pioneered by Caley, Lilienthal, and the Wright brothers and was the key to the first powered, heavier than air, controlled, sustained flight piloted by a human on December 17, 1903. It is interesting that the wind tunnel used by the Wright brothers tested wing sections at Reynolds numbers near 100,000 which falls into the range of natural fliers. Flight in this low Reynolds number regime would not be studied again until the 1990's when technology had advanced enough to make mechanical small scale flight possible. The maturation of technologies ranging from electronics to energy conversion and storage has spurred new interest in low Reynolds number aerodynamics as understanding this complex flow regime is required for the development of bird and insect scale mechanical flight.

1.2 Motivation and Problem Description

1.2.1 Motivation

Small scale flight pervades everyday life in the form of plants, birds and insects and has spurred countless attempts at constructing mechanical analogues. The technical challenges associated with design and construction of such a device have been largely insurmountable as success has been impeded by limited low cost and light weight power storage, efficient propulsion, electronics, and a general lack of fundamental understanding of the aerodynamics. The term Micro Aerial Vehicle's (MAVs) was first introduced in 1992 at the Defense Advanced Research Projects Agency or (DARPA) workshop titled "Future Technology - Driven Revolutions in Military Operations". This led to a series of feasibility studies and a list of design requirements for the development of inexpensive flying robots with no dimension exceeding 6 inches (15.24

cm), an endurance of an hour, a weight of 100 grams and a payload of 20 grams. A vehicle of this nature would be easily transported and deployed in a situation that would otherwise risk human life. Additionally these small flying robots would be capable of providing situational awareness by going places that are inaccessible to humans or larger vehicles.

1.2.2 Problem Description

Physics of Small scale flight: Problems with Aerodynamic performance

The size and mass of an MAV is several orders of magnitude smaller than existing man-made vehicles, though it is Natures primary domain, Figure 1.1.

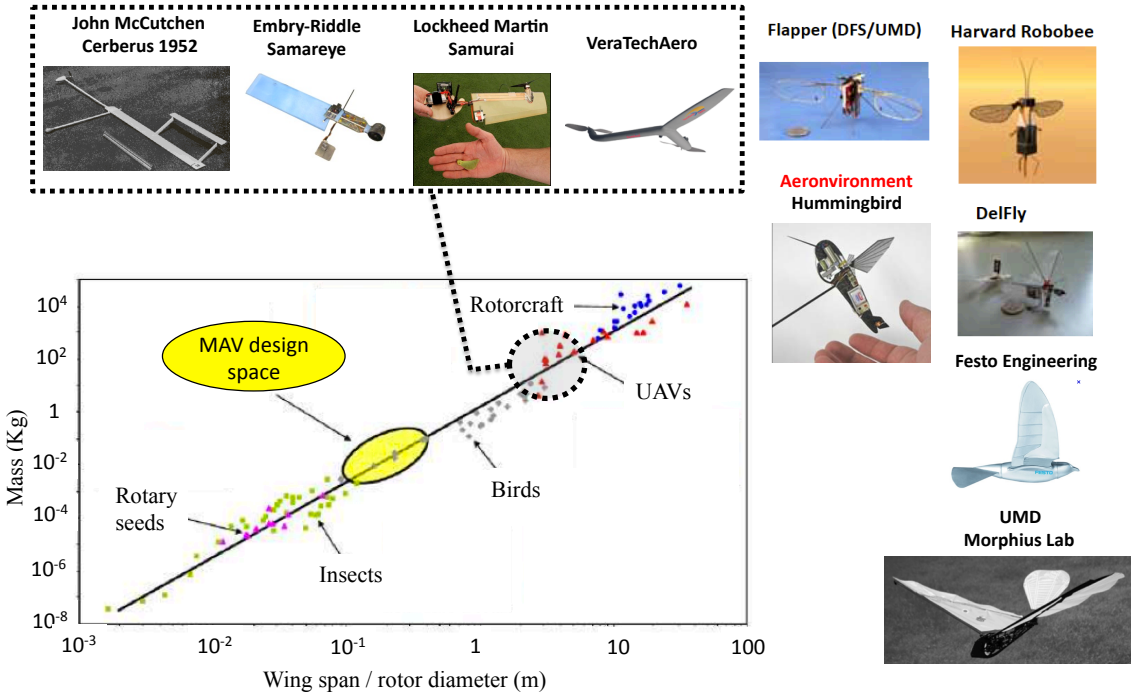

Figure 1.1: MAV flight regime: Mass vs. Size.

To design successful MAV's is it necessary to master a flight regime that differs significantly from that of traditional aircraft. Flow over the wing of a full scale aircraft has been studied thoroughly and is typically laminar. The flight envelope

of the aircraft is specified to avoid flow separation that can lead to stall and aileron reversal. Avoiding this performance degradation is essential as departing from the designated flight envelope risks a loss of control authority and the aircraft. Compared to full scale flight, there is relatively limited understanding of the highly turbulent and easily separated flow over the wing of an MAV. A substantial challenge in modeling the dynamics of micro-scale flight is the general lack of knowledge of the complex low Reynolds number flight regime they inhabit. At $Re < 100,000$ viscous forces are non-trivial and the inherently three-dimensional flow of rotary and flapping wing vehicles cannot be adequately modeled using two-dimensional airfoil data, as lift production at this scale exceeds prediction [2]. The trend of relative magnitude of Reynolds number as a function of gross weight is shown in Figure 1.2 for various aircraft.

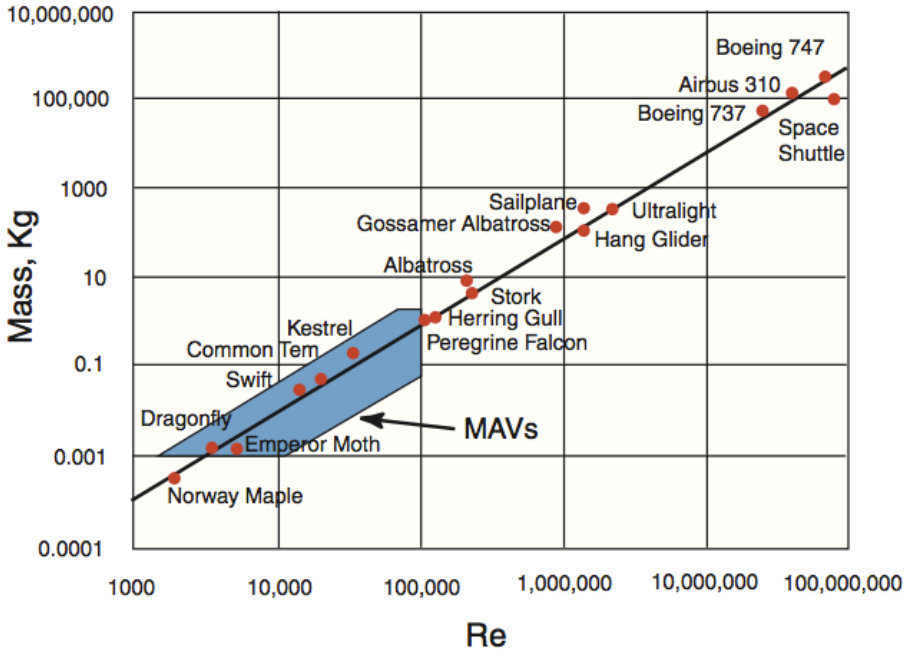

Figure 1.2: Reynold number vs. Mass.

Difficulties in accurately modeling low Reynolds number aerodynamics preclude the use of many modern design tools used in the development of new aircraft. Aerial systems which satisfy the dimensional constraints outlined by the DARPA MAV initiative include fixed-wing, rotary-wing and flapping-wing vehicles. The simplest and

most mature of these platforms are fixed-wing vehicles which boast speed, simplicity and well-known dynamics, however the limitation imposed by forward flight restricts functionality in cluttered environments that can be traversed by rotary and flapping-wing platforms. However, like full scale aircraft, the symmetry and mechanical complexity common to MAV's make them highly susceptible to imbalances and intolerant to object impingement in flight.

The key technical challenges of attaining vertical flight are the same today as they were in the development of the first helicopters, [5].

i.) Basic aerodynamics of vertical flight.

ii.) Lightweight motor/engine.

iii.) Structural and motor weight.

iv.) Rotor-torque reaction.

v.) Stability and control.

vi.)Vibration.

vii.)Safe recovery to the ground in the event of engine failure.

There are no easy solutions to these problems and compromises must be made for typical helicopter configurations. The proposed mission profile requires long duration hover in addition to short periods of forward flight, and so the focus of the design should be in minimizing the power required for hover. The difficulty in attaining improvements in flight performance of rotary wing vehicles is the large hover power requirements. It is possible to optimize for hover but the design constraints are in opposition to those required for efficient forward flight.

Problems encountered in scaling traditional rotorcraft include a disproportionate drop in aerodynamic performance relative to the decrease in vehicle complexity, resulting in aircraft that are limited in performance compared to their full-scale coun-

terparts. The relative performance of a representative set of MAV's is shown in Table 1.1. The table shows that the trend of current fixed-wing and rotary-wing designs use battery power for energy with conventional airfoil shapes for achieving lift, and propellers/rotors for achieving thrust. This implies the use of conventional steady-state aerodynamics in the production of propulsive forces. The complex flapping motion used by the CalTech/Aerovironment Microbat is a departure from convention and the lift generated for flight falls into the realm of unsteady aerodynamics. Despite the various design efforts the flight endurance of the vehicles listed in the table falls short of the desired 60 min and is testament to the difficulty of the task.

Table 1.1: Performance of representative MAVs, [2]

Vehicle properties	Black Widow	Hoverfly	LUMAV	MicroSat	Microbat	MICOR
GTOW, g	80	180	440	110	10.5	103
Cruise speed, m/s	13.4	15-20	5	13.4-15.6	5	2
Wing loading, N/m^2	40.3	-	-	70.9	40	-
Disk loading, N/m^2	-	70	185	-	-	25
Wing span, cm	15.24	18	15.24	22.86	15.24	15.24
Max L/D	6	N/A	N/A	6	N/A	5
Endurance, min	30	13.2	20	25	$2min\ 16s$	3
Hover endurance, min	N/A	7.3	N/A	N/A	N/A	3
Power Source	Battery	Battery	IC Engine	Battery	Battery	Battery
Energy density, $W-h/kg$	140	140	5500 methanol	150	100	150
Hover power, W	24.5	70	N/A	N/A	11	
Hover FM	N/A	0.39	0.41	N/A	N/A	0.55

The scope of the design problem can be understood with a comparison of full scale aircraft to MAV's by a breakdown of the component mass versus payload capacity. Pines, *et al* [2], found the propulsion system of small-scale fliers typically exceed 60%

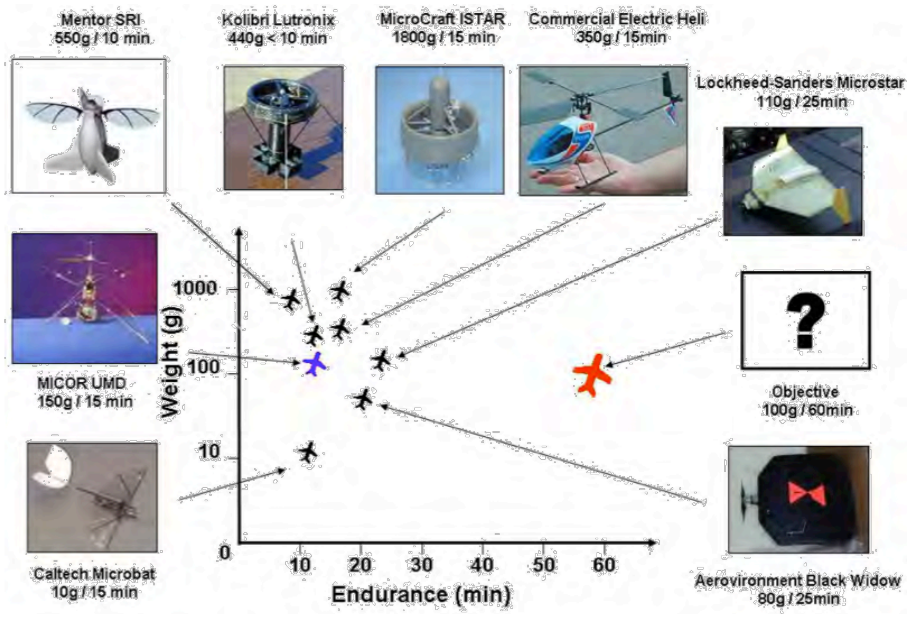

Figure 1.3: Relative performance of various MAVs.

of the total vehicle mass, compared to a jetliner which boasts a propulsion system with a 40% mass fraction. The 20% savings at full scale is used entirely for payload as the Boeing 767 payload mass fraction is 29%, compared to 9% for small-scale flight vehicles, Table 1.2.

Table 1.2: Weight data (In terms of percent of GW).

	Black Widow [40] (Aeronvironment)	MICOR [42] (UMD)	Microbat (Caltech)	Boeing 767
Gross Weight	GW	GW	GW	GW
Structure	18	12	24	35
Fuel/Propulsion	64	70	58	39
Avionics	9	9	18	9
Payload	9	9	0	17

1.3 Literature Review

Three main topics of research pertain to the present investigation, low Reynolds number airfoil aerodynamics of autorotating samaras or rotary winged seeds, and small-scale mono-wing rotorcraft design and control. The flight and geometries of

samara's of the sycamore tree were first studied in the early 1800's, and has progressed more recently with the availability of high speed photography which allows for precise but not continual observation in flight. Prediction of aerodynamic loads on samaras is complicated by the low Reynolds number flight regime in which they operate. Flow separation, laminar separation bubbles and dynamic stall are the least well understood aerodynamic phenomenon. The first mono-wing rotorcraft were built in the 1950's, and incremental progress has been made without major modification of the layout of the original aircraft. Progress is inhibited by a lack of design tools typically available to aircraft designers and poor performance and instability have limited the usefulness and interest in this method of vertical flight. The following literature review presents the main contributions of the various topics of interest.

1.3.1 Low Reynolds number aerodynamics

The performance of micro-rotorcraft to date, is vastly inferior to their full scale counterparts. The main contribution to this inadequacy can be linked to the scaling of the Reynolds number Re, which is defined as the ratio of inertial to viscous forces in a given fluid. The Reynolds number for steady state aerodynamics is defined as the product of a characteristic airfoil chord length and velocity divided by the dynamic viscosity μ of the fluid, this relationship is written as:

$$Re = \rho V c/\mu \tag{1.1}$$

This parameter characterizes the nature of the fluid flow over a body. The lift-to-drag ratio (L/D) is often taken as a measure of a wings overall aerodynamic efficiency. This parameter, although a function of geometry, is highly dependent on the conditions of the flow in which it is immersed. Previous studies have found that the L/D performance of airfoils dramatically changes for $Re<10^5$ illustrating the effect of the

highly viscous laminar flow physics inherent to low Re flow, [3]. The development of the tools necessary to understand the aerodynamic phenomenon for these flow regimes is still in its infancy. A major component of this difficulty lies in the complexity of modeling a flow field governed by low Re which can vary by several orders of magnitude along the span. In a recent study Bohorquez *et al* [4] used blade element momentum theory (BEMT) coupled with a uniform inflow model to determine the two-dimensional lift and drag properties for rotor blades at $Re < 3e^4$. The estimated maximum L/D ratios ranged from $4 - 10$, which are at least an order of magnitude lower than conventional rotorcraft, [4].

Given the poor performance of conventional blade motion and design as applied to micro-rotorcraft, it is only natural to look for unconventional means to increase performance. Millions of years of evolution produced countless creatures which are capable of impressively efficient hover and flight at the Reynolds number of interest. It is not surprising then that researchers have turned to nature for possible solutions. Among these possibilities is the use of unsteady wing/blade motions. Recent studies by Dickenson and colleagues suggest that several unsteady mechanisms may be responsible for the large force generation observed in insect flight, including delayed stall, wake capture, and rotational circulation, [3].

The effects of delayed stall can be understood by examining the boundary layer on an airfoil. The boundary layer state on an airfoil has profound effects on its performance characteristics. The three potential boundary layer conditions are laminar, turbulent, and transitional. The flow in a laminar boundary layer is smooth and free of any mixing of fluid between layers of the fluid. The parameter is defined as the boundary layer thickness, and is the value of (y) for which 99% of the external flow velocity is recovered (i.e., $U = 0.99Ue$). The force produced from the boundary layer surface interaction is a viscous stress; this occurs whenever there is relative motion between adjacent fluid elements. These stresses produce a resistance that tends to

inhibit the motion of the fluid.

The viscous shear stress τ, is related to the absolute viscosity μ, by

$$\tau = \mu \frac{\partial \mu}{\partial y} \tag{1.2}$$

where $\frac{\partial \mu}{\partial y}$ is the rate at which the (y) component of velocity increases perpendicular to the surface.

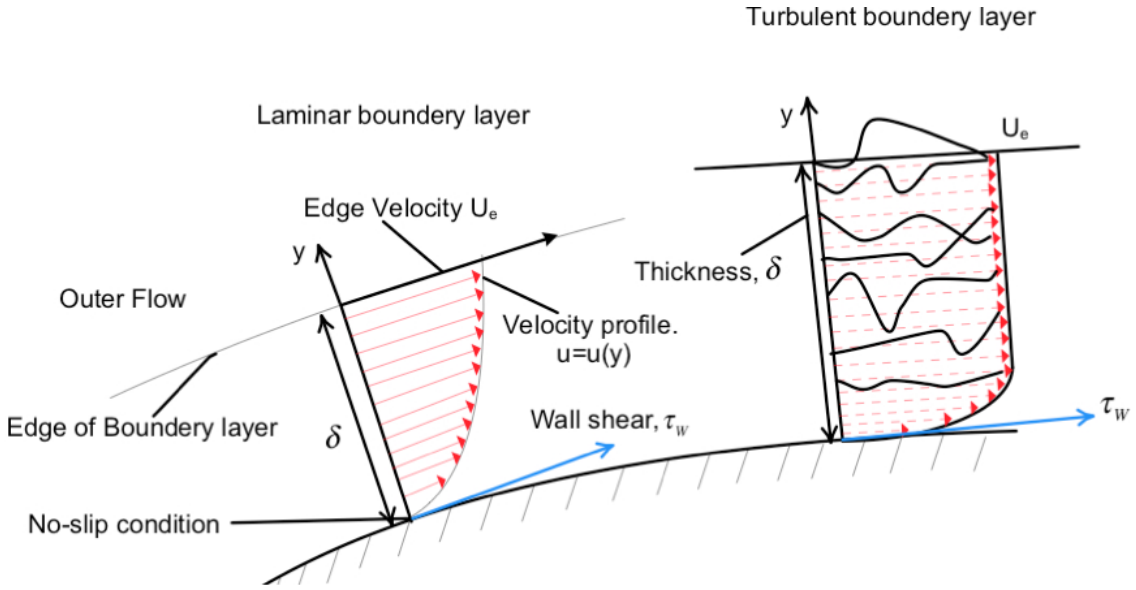

Figure 1.4: Development of a boundary layer on a solid surface.

Figure 1.5 illustrates the development of the boundary layer on a surface. It can be seen that the resultant shear stress produced from the laminar boundary layer is in fact less than that of the turbulent boundary layer, as the velocity gradient is substantially higher for the turbulent flow. A turbulent boundary layer is characterized by larger velocities close to the surface, as well as a great deal of mixing between successive layers. This produces a momentum transfer through the boundary layer leading to larger velocities closer to the surface. In addition to higher viscous shear on the surface of an airfoil, a fully turbulent boundary layer will result in a higher overall profile drag compared with an airfoil with a fully laminar boundary layer.

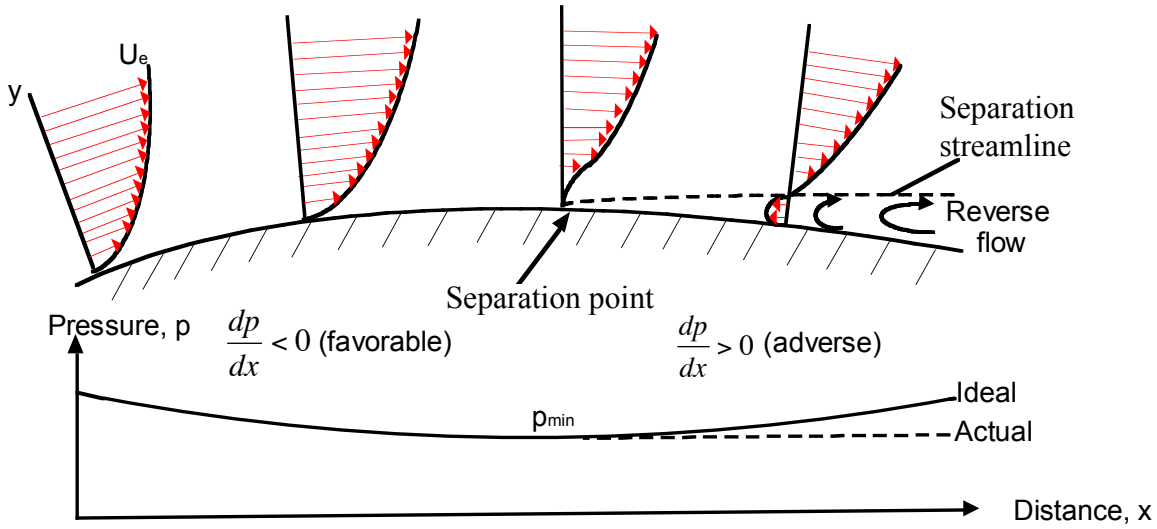

Figure 1.5: Boundary layer separation point.

It has been found that the developing boundary layer on an airfoil is sensitive to pressure gradients. A simplified form of the Navier-Stokes equations is sufficient to observe this sensitivity in the boundary layer. Looking at the x-component of the boundary layer the momentum equation becomes:

$$u\partial u/\partial x + v\partial u/\partial x = -(1/\rho)\partial p/\partial x + v\partial^2 u/\partial y^2. \tag{1.3}$$

The pressure gradient denoted by , $\partial p/\partial x$ when positive, $\partial p/\partial x > 0$, the pressure force is in the direction which decelerates the flow. The intensity of the force on the fluid is at its maximum near the surface of the airfoil, where the velocity is low; hence $\partial \mu/\partial y$ near $y = 0$ becomes smaller the longer the adverse pressure gradient persists. At some point downstream, as shown in Figure 1.6, the magnitude of $\partial \mu/\partial y$ is equal to zero at $y = 0$, at and beyond this point the flow reverses near the surface, this point is called the separation point, as the flow breaks away and leaves the surface, this can be seen in Figure 1.6.

Turbulent boundary layers are much less susceptible to flow separation as compared to laminar boundary layers; this results from a more substantial mixing and

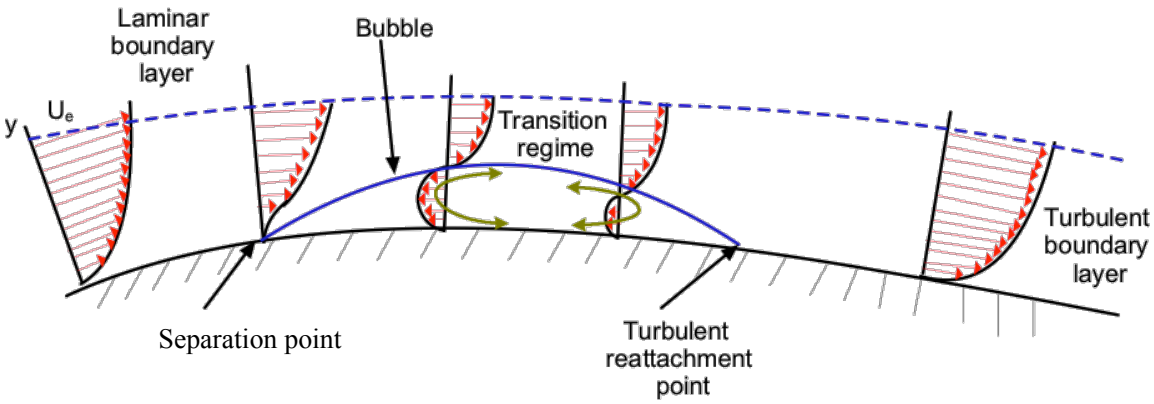

Figure 1.6: Formation of laminar separation bubble.

interlayer momentum transfer of the fluid, [5]. At increasing angles of attack, the increasing intensity of the adverse pressure gradient will ultimately cause the turbulent boundary layer to separate. The occurrence of stall results from a progressive turbulent trailing edge flow separation.

A method proposed by Kim et el [6] to retain attached flow via unsteady blade motions has been studied in detail. In these unsteady motions, the mechanism of delayed stall is related to the shedding of a concentrated vortical disturbance from the leading edge region of the airfoil. The disturbance is shed downstream over the airfoil chord, which has an energizing effect on the boundary layer. This increased energy enables the now turbulent boundary layer to remain attached at higher angles of attack. In this study a two bladed rotor with active twist, capable of 2.3^o tip deflection, produced unsteady blade motions capable of delaying the onset of stall. The unsteady motion substantially increased the airfoil performance in the stall/post stall region when the blade was actuated at its natural frequency of 220 Hz, causing the most substantial tip deflection, [6].

The flexible wing concept proposed by Lian *et al* [7], is advantageous for passive shape adaptation, which can result in delayed stall. It has been shown that under modest angles of attack rigid and membrane wings demonstrate similar lift characteristics. The key difference is the delay of stall to a substantially higher degree angle

of attack, than that of the rigid wing. Typical rigid wings stall between 12 and 15 deg, however flexible wings deform in such a way as to reduce the effective angle of attack, delaying the onset of stall, resulting in stall angles between 30 and 45 deg, [7].

A study conducted in Japan at the University of Tokyo by Tsuzuki *et al* aimed to study vehicle concepts for martian missions dealt mostly with Reynolds numbers below 100,000, [8]. In the current realm of study it is known that Reynolds number is the primary scaling parameter. The Reynolds number can be varied at a constant rotor size by varying the spin rate Ω. In 2D hovering rotor aerodynamics varying the Reynolds number in this fashion is acceptable, however the 3D flow field enclosing the rotor blade at large collective pitch angle has a significant impact on hover performance. It is believed that this effect is caused by leading edge vortices (LEVs), stabilized by the spanwise radial flow, inherent in the rotary movement. The effect is high-thrust production with stall delay phenomena at the large collective pitch.

It is however reasonable to expect the stability of the LEVs to be effected by the centrifugal and Coriolis forces and their contribution to the radial flow. As both the centrifugal and Coriolis forces depend on Ω, it follows that the aerodynamic performance at large collective pitch angles will be sensitive to Reynolds number as well as spin rate, Ω. A well known indicator used to asses the affects of the Coriolis force in a rotational flow field is known as the Rossby number, it is defined as the ratio of Inertial to Coriolis force:

$$Ro = \frac{\rho V^2/L}{2\rho V\Omega} = \frac{V}{2L\Omega}. \tag{1.4}$$

Tsuzuki *et al*'s experiments demonstrate the limitation of the use of 2D aerodynamic methods for the analysis of flows in this flight regime, as they are inherently three-dimensional. Applying such methods as Blade Element Theory would severely under estimate the performance of the rotor at and above the static stall angles of

attack, as the rotors continued to produce thrust, and often had the most significant thrust at the highest collective pitch angles evaluated. It would seem the stability of the LEVs is sensitive to the rotor spin rate, and so as well to the Rossby number, Coriolis, and centrifugal force components.

1.3.2 Rotary winged seeds

The species of tree *Acer* are primary succession plants adapted to nutrient poor habitats in temperate climates [9]. The seeds of the *Acer* utilize the aerodynamic phenomenon known as autorotation. Autorotation is defined as rotational motion induced by aerodynamic loads. Many groups of samara exist and are categorized in a survey by Lugt [10]. The functional significance of the samara is to minimize the descent velocity of the seed carrying fruit, the samara or winged seed. The slower the descent of the samara, the more likely the seed will land outside the resource starved shadow of the parent tree. Motion of the samara in nature is induced from a strong gust of wind that detaches the samara from its branches dispersing the seeds over distances ranging from meters to kilometers [11, 12]. Without horizontal winds the samara has been observed to follow a vertical descent path about a vertical axis, although some samara do additional rotate about their longitudinal axis. The two main groups of samara motion are shown in Figure 1.7.

The flight of rotary winged seeds have been studied since the early 1800's, and was noted in the journal of Sir George Caley [1]. Initial experimentation sought to quantify seed dispersal characteristics and flight path as a function of morphological details, for the study of population dynamics. A representative work of this type was done by McCutchen where an experimental comparison was done between samaras that roll about their longitudinal axis and those that do not [13]. Though a theoretical analysis was not presented he concluded that those that rotate about their longitudinal axis descend faster but are very stable.

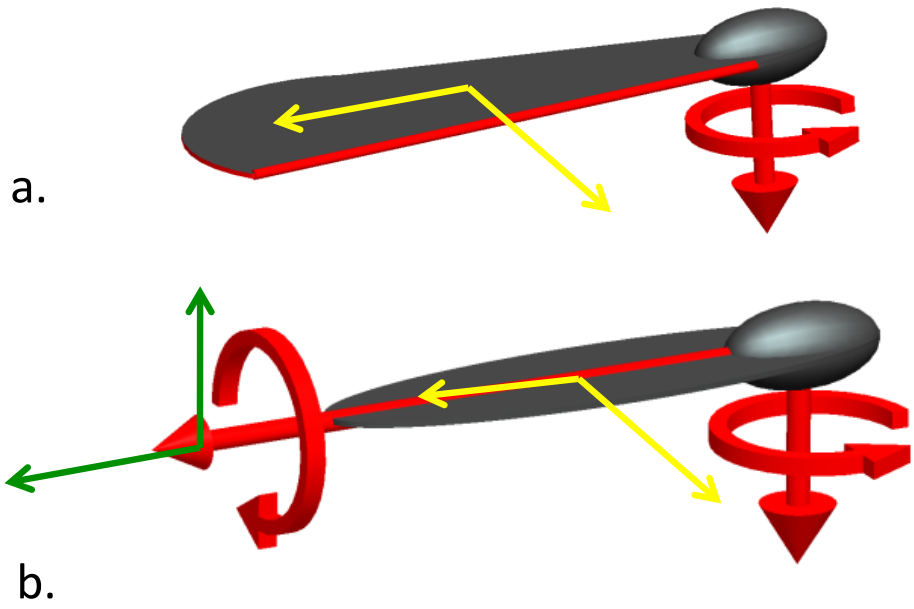

Figure 1.7: Two main classes of samara.

A similar study was performed by Green where over 200 samaras from seven species of trees were photographed, [14]. The characteristics of the flight gathered included: rate of descent, angular velocity, and orientation. The data gathered were used to compare the aerodynamic behavior of samaras, helicopters, and theoretically ideal rotors. The square root of the wing loading showed high correlation with the rate of descent. Additionally differences between samaras that rotate about their longitudinal axis and those that do not were compared.

Azuma and Yasuda [15,16] studied wing surface characteristics and found that the performance of the samara is substantially effected by modifications. Natural samaras were compared to those that had some surface modification including: a smoothing of the surface, and elimination of the leading edge thickness. Each were found to decrease the spin rate and increase the descent velocity. The location of the leading edge roughness, or thickness was as well explored by fixing $0.6mm$ circular rods in different patterns to either side of the fabricated rectangular wing samaras. In each case the samaras with some leading edge thickness outperformed those which did not.

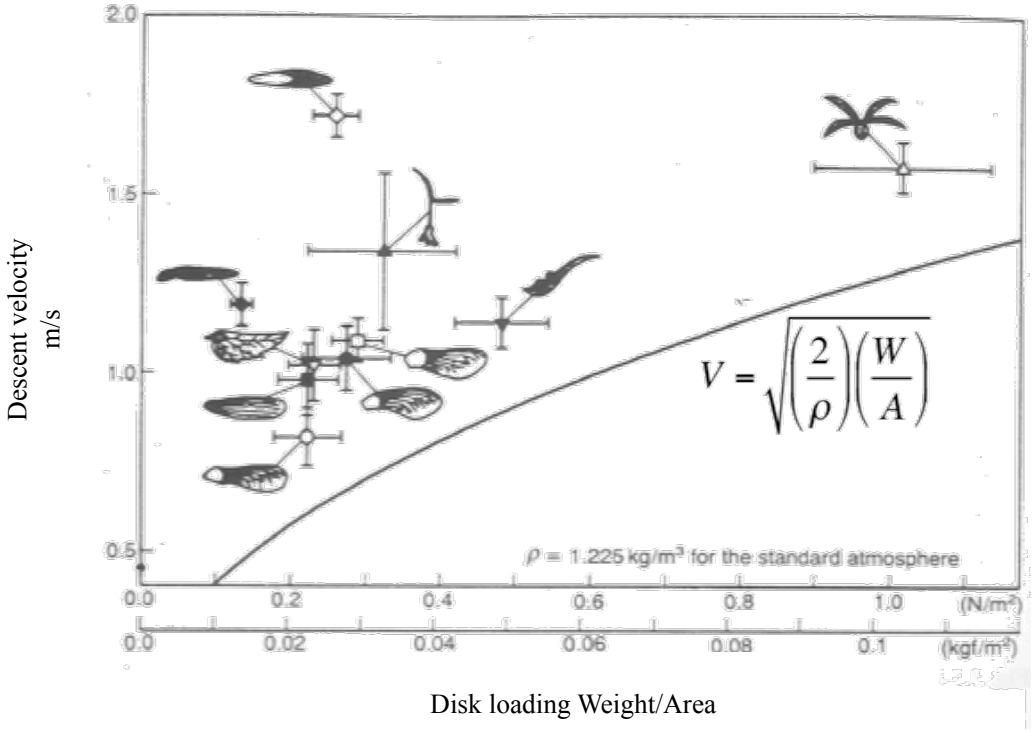

Figure 1.8: Disk loading vs descent velocity.

Chordwise camber was as well studied where it was found that a downwardly convex chordwise chamber with some leading edge thickness substantially out performed samaras with just the chord wise camber by increasing the spin rate and decreasing the descent velocity by as much as 33%. In another study by Azuma and Yasuda the stable locations of the placement of the center of gravity were explored in addition to some simple geometric variation of the wing.

A detailed investigation by Norberg presented a simplified aerodynamic analysis of the samara motion based on momentum theory. Vertical descent and descent with sideslip was included in his analysis and there was a qualitative discussion of entrance into and stability of autorotation. New experimental results along with some theoretical calculations for two kinds of samara were presented, [17].

Surveys on the subject of airborne dispersal of fruits and seeds were presented by Burrows [18] and Ward-Smith [1]. Among the various flight techniques discussed the

autorotation of the samara was noted as one of the more efficient, though theoretical background was very limited and mostly qualitative.

A dynamic model was proposed by Seter and Rosen that allowed prediction of terminal velocity and some in-flight characteristics based on simplifying assumptions. The model was validated by drop tests recorded by cameras placed around the test area, [20, 21]. Solution of the non-linear model requires forcing the roll and pitch to zero, hence the coning and feathering angles are presumed to be constant in steady autorotation. The unknown initial conditions, and limited accuracy of the method of data capture contributed to the errors reported between experiment and simulation. The methods used may have not been precise enough to capture wing oscillations that could be significant in the presence of horizontal winds.

The low Reynolds number flight of the samara was shown by Lentink, *et al* [24] to be similar to that found in some species of insects and birds. Initial experiments used thin plastic models suspended and spun in a vertical wind tunnel while high speed cameras took sequential images of the flow. The experiment used to confirm the presence of leading edge vortices on the samara wing involved construction of a dynamically scaled model immersed and actuated by a robotic arm. They found the leading edge vortex that forms near the base depends not only on the wing shape and Reynolds number, but the wing's angle of attack as well. Specifically the aerodynamic efficiency increases with decreasing angle of attack as the LEV is more compact. Additionally, they found that the 100% higher efficiency of autorotating seeds descend only 30% faster than gliding or straying seeds despite the 450% higher wing loading.

Autorotation has found use in a practical payload delivery device that implemented a flexible samara-wing to decelerate a payload. Analysis of the steady-state characteristics of this device was presented by Crimi [25]. The flexible wing depended on the centrifugal force for stiffening and was modeled with 11-degrees of freedom and

modeled both inertial and aerodynamics forces in detail.

1.3.3 Micro Air Vehicles: The Monocopter

Nature's rotorcraft, the samara, is highly efficient and extremely simple and the design of a rotorcraft based on this asymmetric all-rotating platform represents a paradigm shift in aircraft design. Flight of a monocopter differs from full scale helicopters as there exists no stationary frame of reference from which control inputs can be applied. The first monocopters were built before the availability of microelectronics and many were flown without control. Knowledge of the vehicle's orientation relative to the desired flight path is required for aircraft control, and several monocopters have been built that are capable of carrying sensor packages and processors enabling autonomous flight. However these electronics are not commercially available in the weight class required for use on nano-class vehicles and therefore a new control methodology must be developed.

Designing a vehicle at the MAV scale does have the advantage of excluding the human pilot/cockpit/cabin etc. Without an on board pilot keeping the orientation of the vehicle fixed becomes unnecessary and all-rotating rotorcraft enter the design space while simultaneously solving technical challenge **iv**. The problem of unequal blade loading **v** and vibration damping **vi** can be solved by reducing the number of blades to one, and allowing for the rotor to be free from a non-rotating hub. By configuring the vehicle to resemble inertially and aerodynamically a samara or winged seed, the vehicle will be recoverable after an engine failure from any altitude **vii**.

The concept of a single-wing rotating aircraft is not a new one, and the first vehicle of this type was flown in 1952 in the woods surrounding Lake Placid, New York by Charles W. McCutchen [26]. McCutchen experimented with a number of different designs including some that incorporated underslung payloads. Though few publications exist that detail the design and performance of monocopters, some of the

design considerations are detailed in the July 1954 issue of Aeromodeller Magazine. Most of the monocopter flights made in the past 60 years have used a model rocket motor for propulsion and lacked any means of directional control.

The theory of the design of a monocopter was presented by Francis Graham in 1999, [26] with concepts taken from the original machine built by McCutchen and subsequent ones built by Graham himself. The monocopters described by Graham are rocket powered and do not perform stable forward flight. The contributions of the wing and motor force balance are treated and some configuration constraints are defined. Most notable is the requirement that the motor be angled so as to produce thrust in the vertical direction opposing the upward motion of the aircraft in flight.

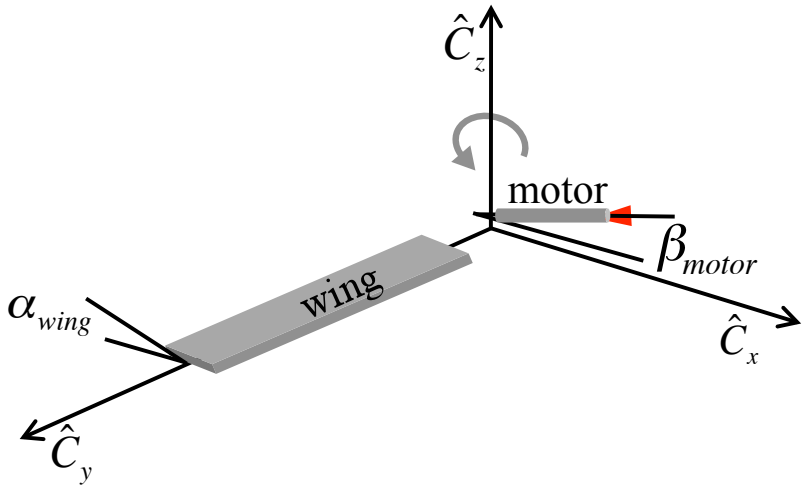

Figure 1.9: Conventional monocopter diagram of wing and motor orientation, Ref[[26]].

A more recent vehicle was developed and flown by a team led by Lockheed Martin Advanced Technology Laboratories [22]. The prototype called MAVPro incorporated an outrunner motor with an 20.3 cm diameter propeller, weighed 0.514 Kg, rotated at a stable 4 Hz, and could climb to 15 m with radio controlled actuation of a trailing edge flap. The MAVPro incorporated the AG38 airfoil, and exhibited a rectangular planform geometry.

The various single winged rotating aircraft developed over the years have made

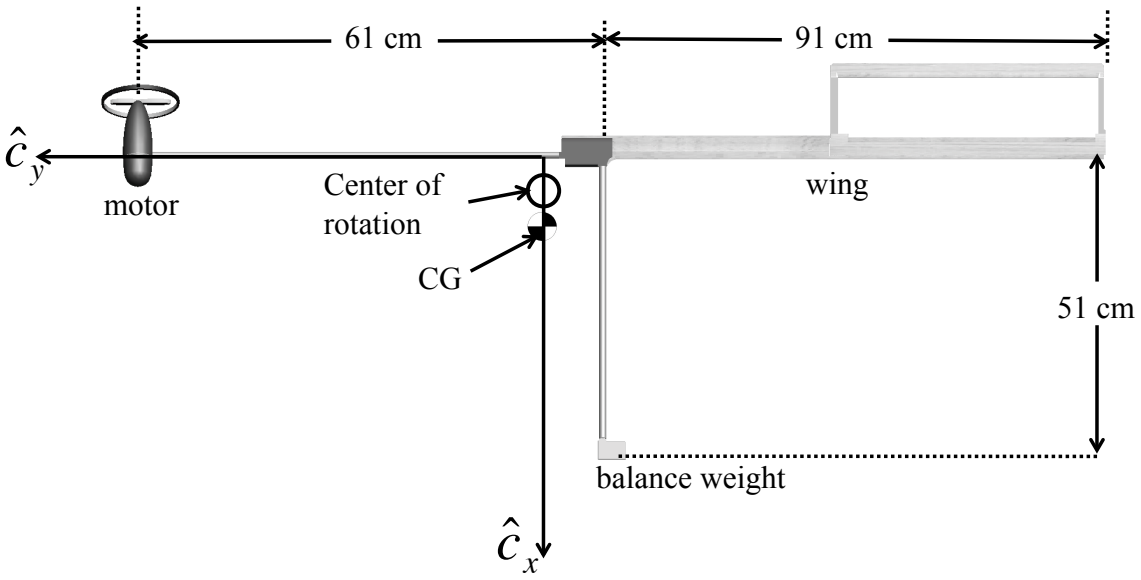

Figure 1.10: Conventional monocopter schematic, Ref[[26]].

no attempt to utilize the most basic mode of transit of natural samara, autorotation. Additionally, airfoil cross sections and planform designs have had no similarity to that found in natural samaras [26, 22].

Conventional monocopter designs apply torque to the vehicle with a thrust device slightly off-set from the $\hat{c}_y$-axis (see 1.10), and in the case of MAVPro the propeller spins in the $\hat{c}_y$-$\hat{c}_z$ plane and influences the stability about the $\hat{c}_y$-axis. This configuration results in the propeller fighting the pitch input from the flap and reduces controllability of the vehicle. Additionally, for stability in vertical flight, the layout of the aircraft requires the thrust vector be in opposition to the lift vector slowing its accent and reducing its payload capacity.

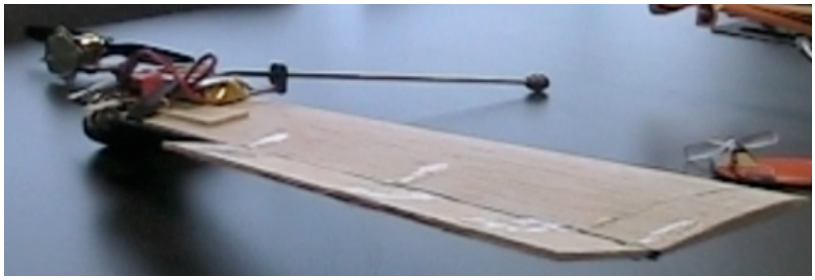

Figure 1.11: Lockheed Martin MAVPro.

1.4 Objectives

Attempts to scale down the existing monocopter configuration have hit a clear barrier. An alternative approach to the design and control of mono-wing aircraft is detailed in this dissertation and consists of six main objectives that are discussed below.

The most common method of experimentation to date has been to suspend the samara in the flow of a vertical wind tunnel while recording the flight with cameras placed around the perimeter. The test section size and proximity of the cameras prevented data from being collected beyond the perimeter of the wind tunnel. This restriction on lateral transit precludes observation of the present dynamic phenomenon of interest; horizontal motion that moves the samara away from the parent tree. Therefore the first objective of the current research is to develop and implement a drop test stand and experimental procedure that can be used to characterize the flight path and observe precisely and repeatably any feathering/conning oscillations that may have gone unnoticed in previous work.

The second objective is the experimental identification and characterization of an airfoil for the implementation of an efficient MAV rotor. Structural and manufacturing constraints need to be considered in order to apply the findings on a working prototype. Rotor design, and the effect of blade and airfoil parameters on autorotational performance are also explored in order to determine basic small-scale rotor design guidelines.

The third objective is to design and fabricate a prototype mono-wing rotorcraft with a different configuration from the classical design including servo control of the samara-like wing geometry. The goal of the design is to achieve stable flight for an at-scale robotic samara. The vehicle will retain the inertial properties of natural samara allowing for autorotation in the event of motor failure. The majority of the components will be plastic fabricated by a rapid prototyping machine which will allow

for a fast iterative design process.

The fourth objective is to improve the prototype durability by replacing plastic parts with a durable light-weight material so as to create a robust vehicle that will be unharmed upon contact with the wall or ground. This is necessary as the small lab space and fragile initial designs resulted in many vehicles being destroyed making repeatable experiments quantifying the dynamics impossible.

The fifth objective is to design an experiment to study and quantify the heave dynamics of the robotic samara. The near hover dynamics of robotic samara controlled by wing pitch variation have not been characterized previously and so a method developed to characterize the dynamics of miniature rotorcraft is adapted and implemented. System identification of the heave dynamics aids in the validation of the derived linear model. The model will be validated by realtime implementation of PID feedback regulation of altitude.

The sixth objective is to develop, implement and quantify a method of lateral control that can be used by a remote pilot using minimal onboard sensing and actuation. System identification techniques will be used to quantify stability derivatives from flight test data captured from a visual tracking system. This will allow for the construction of a mathematical model for use in future controller design.

1.4.1 Contributions

The key contributions of this research include:

1) The design, construction, testing, and characterization of new mechanical samara prototype geometries that through experimentation identify a geometry for a minimal descent rate. The location of the wing area centroid was found to determine descent rate, a trend not captured by wing loading or disk loading.

2) Constant coning and feathering angle is well established in the literature, however all mechanical samara models tested exhibited large oscillatory motion which has been quantified and reduced to a Fourier series representation of the roll and pitch.

3) Observation and characterization of two modes of flight that differ in flight path radius, wing pitch amplitude, and descent rate.

4) Design and fabrication of a new configuration of hover capable robotic samara controllable in the vertical direction by variation of the throttle.

5) Design and fabrication of a new configuration of hover capable robotic samara controllable in the vertical and horizontal direction by variation of the servo controlled wing pitch angle.

6) Performed iterative design improvements resulting in a vehicle capable of sustaining wall and ground contact without damage allowing for repeatable testing to be done.

7.) Designed an experiment to measure the heave and lateral dynamics of an open-loop human piloted robotic samara with the use of vision based positioning system allowing for simultaneous tracking of both input to the vehicle and the response that follows.

8) Derived nonlinear Euler equation based heave and lateral dynamics of a model for the robotic samara in hover and coordinated helical turn.

9) Used two different system identification packages to determine the stability derivatives of a heave dynamic model as well as a lateral dynamic model.

10) Invented a new method to control a mono-wing rotorcraft by slow variation in wing pitch angle which modifies the circular flight path enabling full controllability with a single input. Control can be implemented with a human remote pilot without onboard sensors for determining orientation.

11) Designed, fabricated and flew the first at-scale robotic maple seed or samara.

12) Discovery of forward speed instability, or non-minimum phase zero in the robotic samara lateral dynamics model.

1.4.2 Organization of Dissertation

This dissertation is comprised of six chapters that follow the logical progression of the project. Chapter 1 begins with an introduction to the field of flight and the state of the art of interest to this work. A detailed literature review of the relevant topics is presented. Chapter 2 begins with the design of the mechanical samara's used to characterize the impact of span-wise chord variation on the descent velocity and attitude dynamics. The experimental setup is then described followed by the method used to reduce data captured from the vision based tracking system to meaningful flight dynamics. The oscillatory motion or the roll and pitch is then reduced to a convenient Fourier series representation and is followed by a discussion of the different flight modes observed. Chapter 3 covers the design challenges associated with creating a mono-wing rotorcraft and discusses four iterations that covered the most significant advances. The specific design constraints of the layout of the vehicle are discussed with suggestions for wing design, motor angle, servo connection to the flap/lead/lag hinge,

and landing/take off gear location and orientation to prevent ground impingement. Next, the structural characteristics unique to the layout of the aircraft fuselage and wing are discussed. The chapter ends with scaling issues and performance metrics for three different size vehicles. Chapter 4 covers the vertical dynamics as forced by variation of the wing collective pitch angle. The experimental setup and conversion to conventional aircraft dynamics is covered with discussion of data synchronization and error. The next section covers the system identification process and techniques used to identify the governing heave dynamics and associated estimation errors. What follows in the implementation of PID controller on two vehicles using altitude feedback from position data gathered by the visual positioning system. Chapter 6 introduces a new method of control that exploits a single degree of freedom input command for full controllability. A new flight dynamics model based on a helicopter coordinated helical turn is used as a basis for identification of a lateral flight dynamics model. Next the experimental setup and open loop control technique is discussed for a data set consisting of a coordinated u-turn. Next error estimates on stability derivatives and the discovery of a non-minimum phase zero is covered. Finally a discussion of the major contributions of the work is given along with recommendations for future study and applications unique to this new type of aircraft.

Chapter 2

Free Flight Autorotation Samara Dynamics

2.1 Introduction

Samaras, or winged seeds, are the sole method by which several species of plants disperse their seed. Geometric configurations for maximal seed dispersal has evolved into two main classes of seeds [15], both of which execute autorotational flight as they fall from the tree, and one of which additionally rotates about its longitudinal axis. This discussion is limited to samaras which execute only autorotational flight.

Advances in technologies associated with the sensing and control of unmanned vehicles has allowed conventional micro-scaled vehicles to be equipped with real-time systems. The capabilities of these small systems are limited by the battery life and power consumption of all on-board electronics and actuators. The majority of the power in an aerial system is consumed by sustaining a desired flight mode for which the primary focus is to counteract the effects of gravity [2]. Perhaps a new paradigm is needed, one with a focus on a vehicle design with a passively stable primary mode of operation that requires little or no additional power to attain/maintain this mode

of transit. The natural flight of a samara is one of balance, trading gravitational potential energy for rotational kinetic energy, perpetuating an aerodynamically stable helical descent.

In nature the phenomenon of autorotation is utilized by various species of trees. The efficiency of a samara's autorotation heavily influences the population dynamics. The evolution of the samara provides a near infinite set of feasible autorotation configurations, each with distinct dynamics.

The goal of this chapter is to characterize the impact of span-wise chord variation on the descent velocity and attitude dynamics. This characterization will provide a baseline for mechanical samara planform design and provide insight into lift production of samaras.

2.2 Mechanical Samara Design

The models are designated by the planform geometry A41, B41, C41 and D41. The geometry of the models tested are not simple scaled-up versions of natural samaras. The design involved a trial and error method aimed at producing a mechanical samara capable of being tested in the limited space of the laboratory with the main constraint being the height of the ceiling. Design of the mechanical samara involves precise placement of the center of mass, since a poor choice results in a less stable and efficient autorotation. The low Reynolds number flight regime of the mechanical samara, Fig. 2.1, requires a non-standard airfoil cross-section based on geometric properties observed in natural samara. Azuma *et al* showed that a thick leading edge resulted in a 33% decrease in descent velocity; increased surface roughness also decreased the descent velocity [16]. The mechanical samaras designed for these experiments exhibit a smooth surface finish. Each model is designed with similar cross-sectional properties that only differ in chord length. The general layout of the airfoil includes

a thick leading edge followed by a thin region that extends to the trailing edge. Stable autorotation is sensitive to the distribution of mass along the chord line and precludes the use of many standard airfoil cross-sections including flat plate geometry. Stiffeners span the length of the samara wing and are required for structural rigidity of the model, (Fig. 2.2).

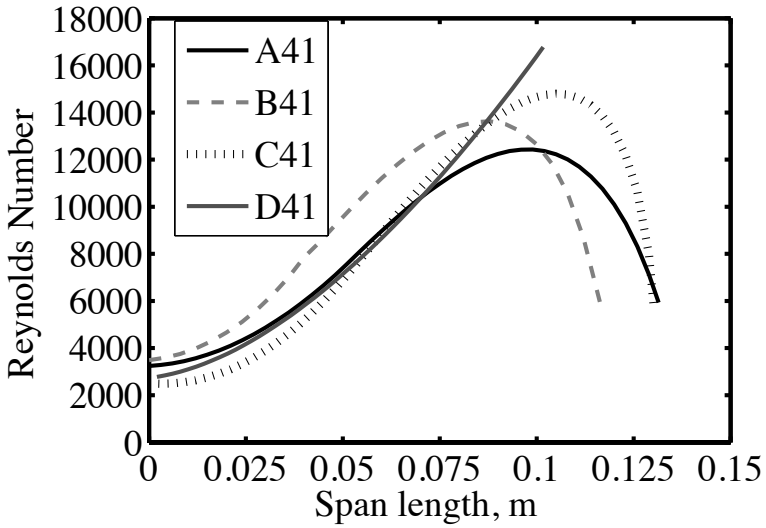

Figure 2.1: Mechanical samara Reynolds number variation with span length.

The models were designed using computer aided design (CAD) software capable of precisely calculating the model surface area, the location of the center of mass, as well as overall model mass. These parameters are held constant over the four different subjects shown in Fig. 2.3. The CAD model can then be exported as a stereo-lithography file (STL), which is a representation of the samara's geometry as approximated by triangles of varying dimension. This file is then used by the Eden350 rapid prototyping machine to create the physical prototype. The tolerances of the machine are 42 μm in the X-Y plane and 16 μm in the Z-plane [27]. Subjects are built in the same orientation on the machine to ensure similarity between models. The resin type used to construct all tested mechanical samara is VeroBlack [28]. The resin was chosen for its high color contrast with the reflective markers and its material properties which are listed in Table 2.1.

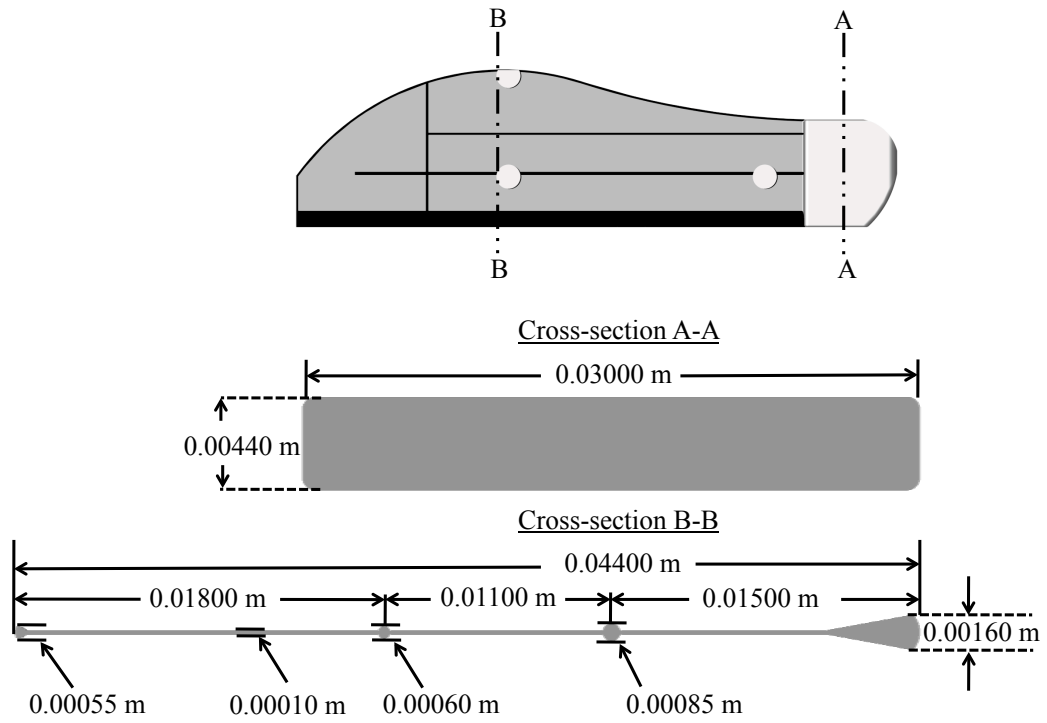

Figure 2.2: Samara model airfoil cross-section.

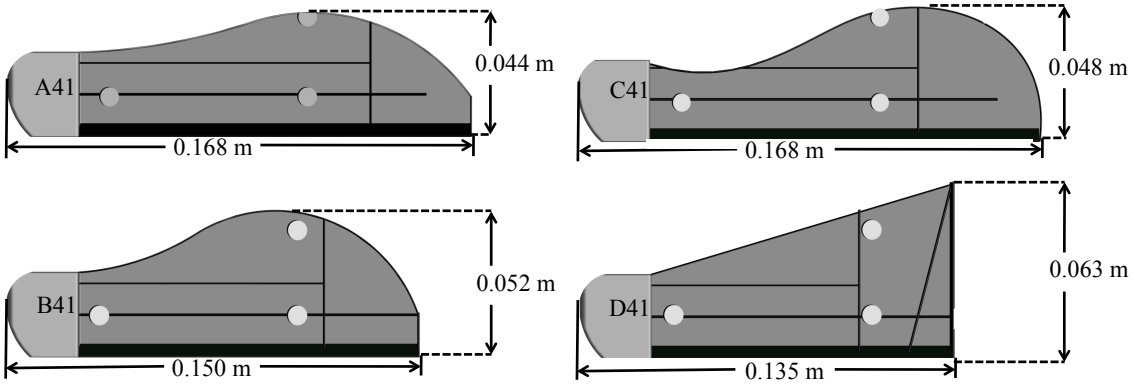

Figure 2.3: Samara model geometry.

Table 2.1: Mechanical samara material properties, VeroBlack [28]

Property	ASTM	Unit	Value
Tensile Strength	D-638-03	Mpa	5.070×10^1
Modulus of Elasticity	D-638-04	Mpa	2.192×10^3
Flexural Strength	D-790-03	Mpa	7.960×10^1
Flexural Modulus	D-790-04	Mpa	2.276×10^3
Density		Kg/m^3	1118

Table 2.2: Physical properties of the mechanical samaras

Item	Symbol	Units	A41	B41	C41	D41	Multiplier
Length of Wing	L_w	m	0.168	0.150	0.168	0.135	
Span of Wing (CG to tip)	R	m	0.131	0.116	0.130	0.102	
Mass	m_w	Kg	5.26	5.26	5.26	5.26	$\times 10^{-3}$
Total Weight	W	N	0.052	0.052	0.052	0.052	
Surface Area	S	m^2	1.24	1.24	1.24	1.24	$\times 10^{-2}$
Max Chord	c_m	m	0.044	0.052	0.048	0.063	
Aspect Ratio	R^2/S	$-$	2.29	1.81	2.27	1.48	
Wing Loading	W/S	Nm^{-2}	4.16	4.16	4.16	4.16	
Disk Loading	$W/\pi R^2$	Nm^{-2}	0.96	1.23	0.98	1.59	
Principal	I_1	Kgm^2	4.99	5.80	5.16	6.59	$\times 10^{-7}$
Moments of	I_2	Kgm^2	9.64	7.62	10.0	7.6	$\times 10^{-6}$
Inertia	I_3	Kgm^2	10.1	8.18	10.5	8.29	$\times 10^{-6}$
Rotation Angle:							
$[\tilde{e}_x]$ to I_1	-	$Degree$	0	0	0	0	
$[\tilde{e}_y]$ to I_2	-	$Degree$	0	0	0	0	
$[\tilde{e}_z]$ to I_3	-	$Degree$	88.348	89.964	89.354	93.439	
Radius of	R1	mm	9.74	10.50	9.90	11.12	
Gyration	R2	mm	42.81	38.04	43.58	37.82	
-	R3	mm	43.87	39.42	44.66	39.38	

The mechanical samara tested have the physical properties listed in Table 3.4. All of the mechanical samaras are planar symmetric, and hence, have zero twist. The inertias reported here include the final addition of the marker mass. The geometry of the planform area for A41, B41, and C41 can be represented through Fourier series approximation of the chord variation with the radius, as seen in Fig. 2.4. The coefficients of the resultant series approximation of the geometry along with the mean square fit error are listed in Table 2.3 for the series:

$$\hat{c}(s) = a_0 + \sum_{n=1}^{6} a_n \cos n\pi s \tag{2.1}$$

The geometry of the D41 model is calculated from the schematic provided in Fig. 2.3.

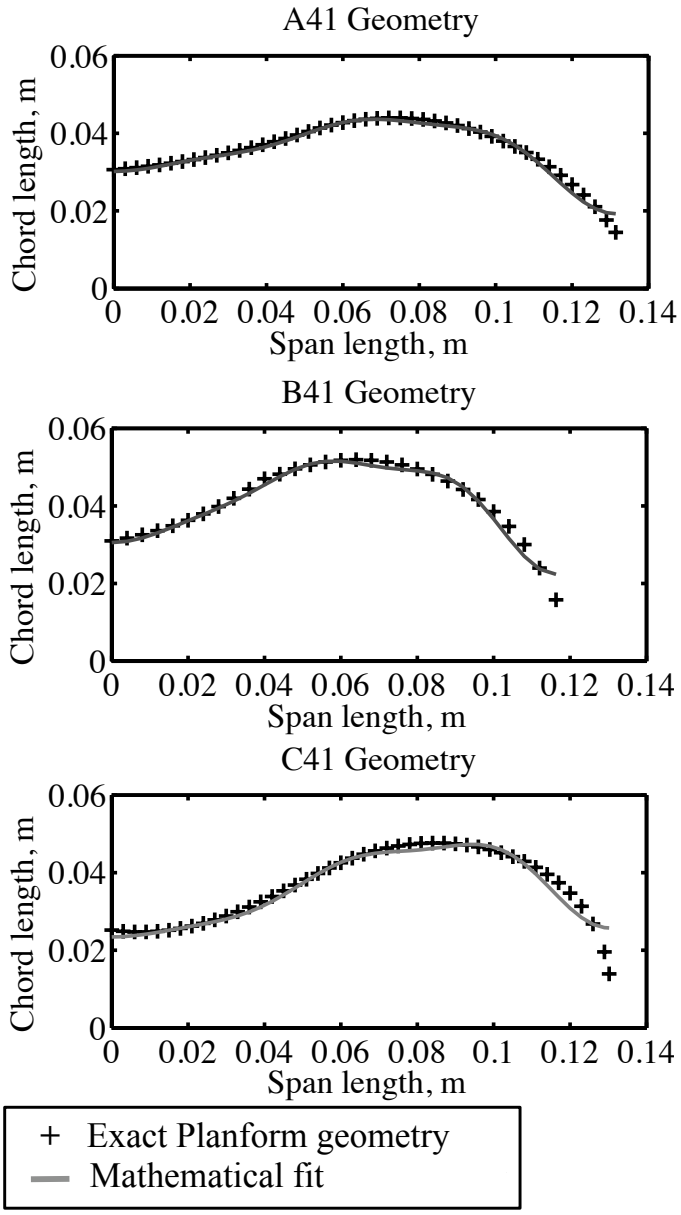

Figure 2.4: Samara planform geometry and Fourier series approximation of samara planform geometry.

2.3 Experimental setup

The flight dynamics of the samara are most accurately measured through vision-based motion capture. This method eliminates the need for costly micro-scaled sensor packages and is employed with use of a Vicon vision system [29]. The system collects data by capturing 2D images of the subject which is fitted with retro-reflective

Table 2.3: Coefficients of the Fourier series representation of mechanical samara planform geometry.

Fourier Coefficients	A41	B41	C41
a_0	$+0.0358$	$+0.0414$	$+0.0362$
a_1	$+0.0010$	-0.0006	-0.0071
a_2	-0.0084	-0.0113	-0.0085
a_3	$+0.0032$	$+0.0029$	$+0.0040$
a_4	-0.0017	-0.0024	-0.0017
a_5	$+0.0012$	$+0.0019$	$+0.0019$
a_6	-0.0011	-0.0012	-0.0013
MSE	1.20×10^{-4}	0.80×10^{-4}	3.70×10^{-4}

markers. The Vicon system strobes light at the frame rate of the camera. The light incident on the surface of the marker returns to its source, reducing errors commonly caused by interference. The light returned to the lens allows for a quick computation of the centroid of the marker. Three-dimensional position is obtained from a least-squares fit of the two-dimensional camera observations. The setup of the workspace tracked by the Vicon system is shown in Fig. 2.6 and is limited to the area labeled as the data capture region. This setup allowed the samara to fall a distance of 8 m before flight data were recorded.

A stable autorotation was achieved in every flight test observed. However, the chaotic flight prior to autorotation often resulted in the samara traveling outside the capture volume. Two dominant flight patterns emerged differing both in descent velocity and radius of precession. The flight path characterized by a larger radius of precession is discussed in Ref. [50]. The flight path characterized by a smaller radius of precession is discussed in this manuscript. The cameras are labeled one through seven and are placed around the test area as shown in Fig. 2.6. The camera system used to capture data in these experiments was the Vicon MX-F40 [29].

A simple mechanical release mechanism is used to hold the mechanical samara at a predetermined angle. The grip is grooved to ensure exact placement of the samara for each drop test. The release mechanism is mounted 12 m above the ground. The

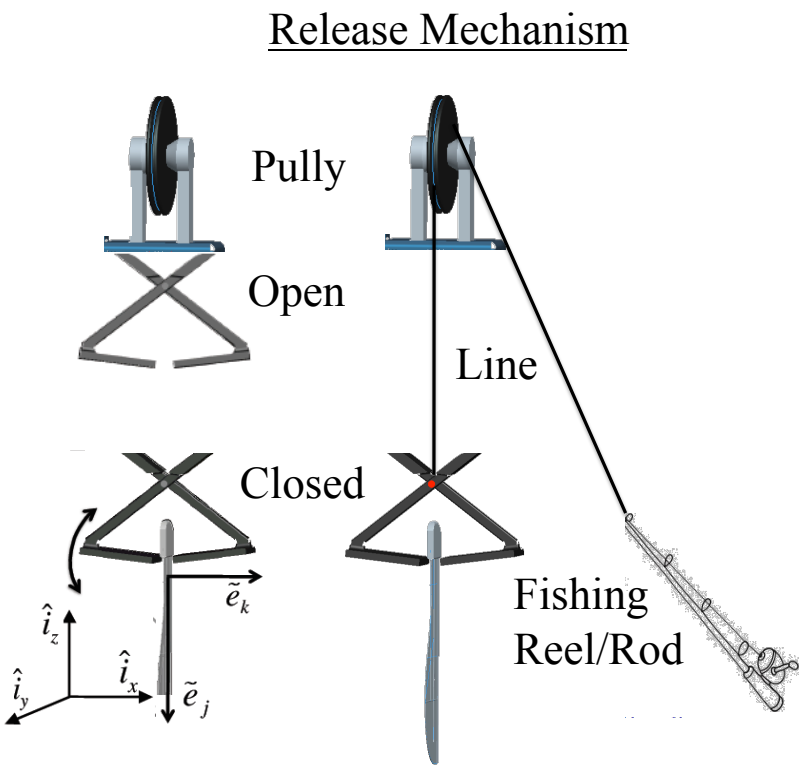

Figure 2.5: Mechanical samara release mechanism: The test subject is loaded into the claw and closed, the claw and samara are hoisted to the pulley by progressing the reel on the fishing rod, once the claw has reached the pulley a final abrupt pull opens the claw and releases the samara into free flight.

mechanical samara is released after transient motion has subsided. The samara is placed into the gripper and hoisted to the ceiling by an attached thread of monofilament. The monofilament drapes over a pulley, back down to the ground, and is attached to a fishing rod.

In order to minimize wind disturbances which may affect the flight dynamics, these experiments were conducted in a room with no ventilation. The test facility encompassed two platforms which provided the mounting area for cameras. The viewing angle of the cameras is critical in capture as well as calibration of the system. A minimum of three cameras is needed to calibrate the ground plane. This step in the calibration dictates the skew, if any, of the vertical axis with respect to the ground plane. To avoid potential errors from a poorly calibrated ground-plane, markers are

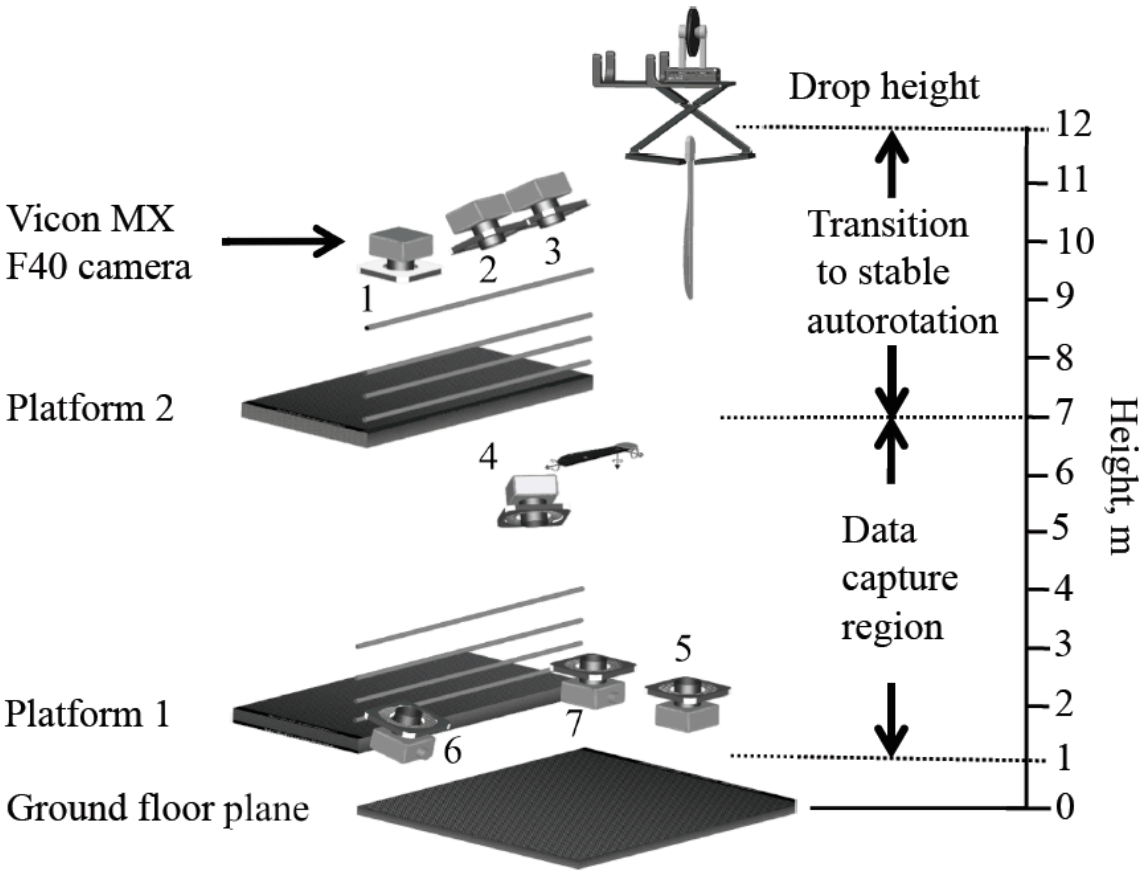

Figure 2.6: Depiction of experimental workspace

distributed in the area of interest, and the Vicon system takes an average of the location of the markers which improves the accuracy of the previously calibrated ground-plane. This calibration gives the user a least-squares estimate of the error associated with the tracking of each marker. Tracking errors for the trials included here were measured by recording data while the mechanical samara was motionless. The resultant measurement characteristics are displayed in Table 2.4.

Table 2.4: Measurement Characteristics

Measurement	Symbol	Variance	Unit
Time	t	-	s
Position	x, y, z	0.6128×10^{-3}	m
Orientation	ϕ,θ,ψ	7.8000×10^{-3}	rad
Translational Velocity	u, v, w	0.2510×10^{-3}	m/s
Rotational Velocity	p, q, r	1.2000×10^{-3}	rad/s

The location of the markers placed on the mechanical samaras is recorded by the Vicon system prior to flight testing. This calibration aids in the proper labeling of reconstructed marker location by excluding erroneous data that falls outside of the possible range of marker location for a given samara. This step also ensures the vision system is able to track the motion of the samara. The samaras are designed with grooves which trace the outline of the intended marker location. Any error in marker location is reduced in the calibration of the samara to the the values reported in Table 2.4. Typical motion capture work employs spherical marker geometry. In this work, a flat circular marker that is 0.007 m in diameter and 0.0001 m thick is used.

The non-standard marker geometry is chosen to interfere minimally with the aerodynamics of the samaras tested. A marker is placed in the same location on both sides of a samara and represent a single marker location to the visual tracking system. The conformal markers are intentionally placed on the samara in locations that are raised from the surface. This provides the marker with some three-dimensionality which aids in the ability of the vision system to track a samara. The marker discs were made using a hole punch on 3M 7610 high-gain reflective sheeting. Three markers are placed on the samara permitting attitude determination. Marker placement for the rigid body model is shown in Fig. 2.7 in Vicon inertial coordinates. A representative schematic showing the virtual flight path of the samara as observed by the vision system is shown in Fig. 2.8. The unprocessed flight data for each of the models, as recorded by Vicon, is shown in Fig. 2.20.

When working with the Vicon software, a rigid body model that defines the degrees-of-freedom of each of the segments of the samara is required. This helps to ensure only physically possible solutions are converged upon in the post processing of a trial. A rigid body is defined with a fixed body coordinate system, hence the Euler angles for a clockwise descent are different then those of a counterclockwise descent. An additional rotation of π about the fixed body X-axis is necessary to avoid

the singularity this introduces in the calculation of the orientation.

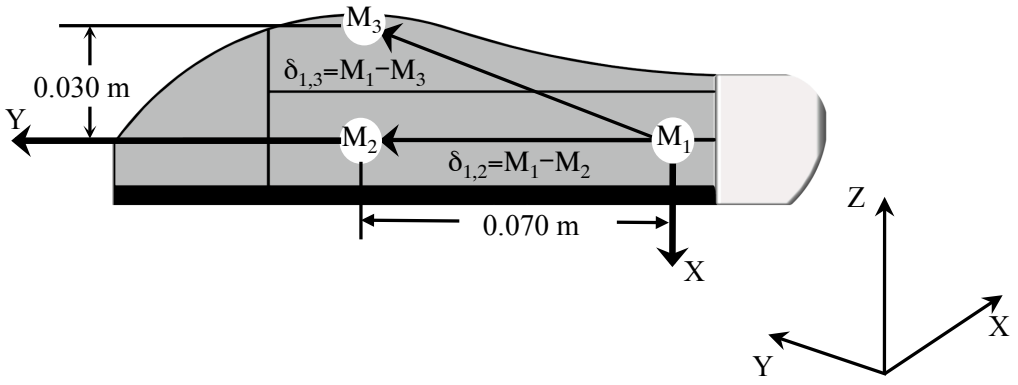

Figure 2.7: Retro-reflective marker placement (Vicon body fixed coordinate frame)

2.4 Data Reduction and Analysis

2.4.1 Attitude Determination

The 3D marker position data provides a means of resolving the orientation of the mechanical samara in space. The three markers are sufficient to describe an orthonormal basis from which the rotation matrix representing the samara's orientation can be formed. The first vector forms the $\tilde{e}_j$-axis in body frame coordinates and is the line from the samara center of mass to the marker located 0.070 m in the positive Vicon Y-direction. The remaining bases require an intermediate vector from which to compute a cross product defining the $\tilde{e}_k$-axis as follows:

$$\tilde{\delta}_{1,2} = M_1 - M_2 \tag{2.2}$$

$$\tilde{\delta}_{1,3} = M_1 - M_3 \tag{2.3}$$

$$\tilde{v} = \frac{\tilde{\delta}_{1,3}}{||\tilde{\delta}_{1,3}||}. \tag{2.4}$$

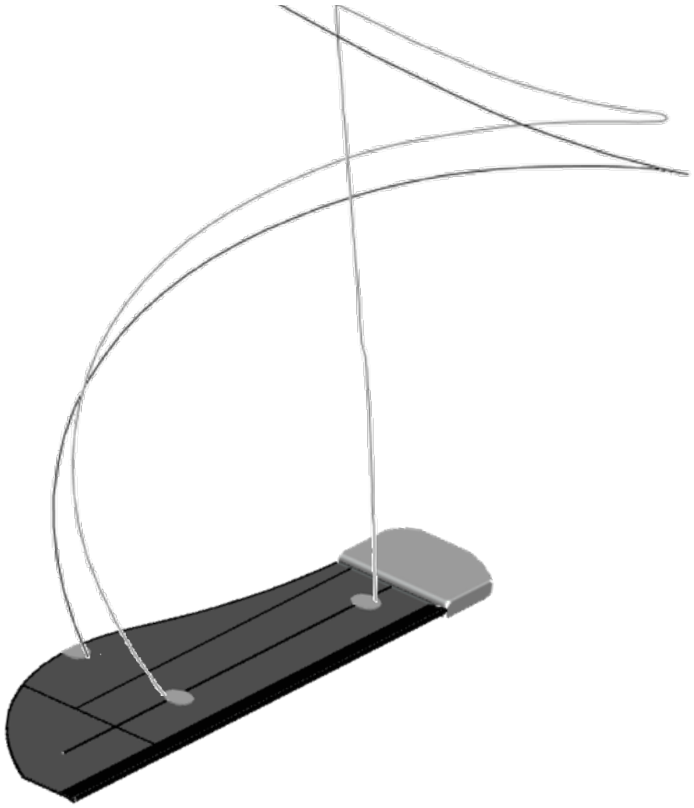

Figure 2.8: Virtual flight path as seen by Vicon.

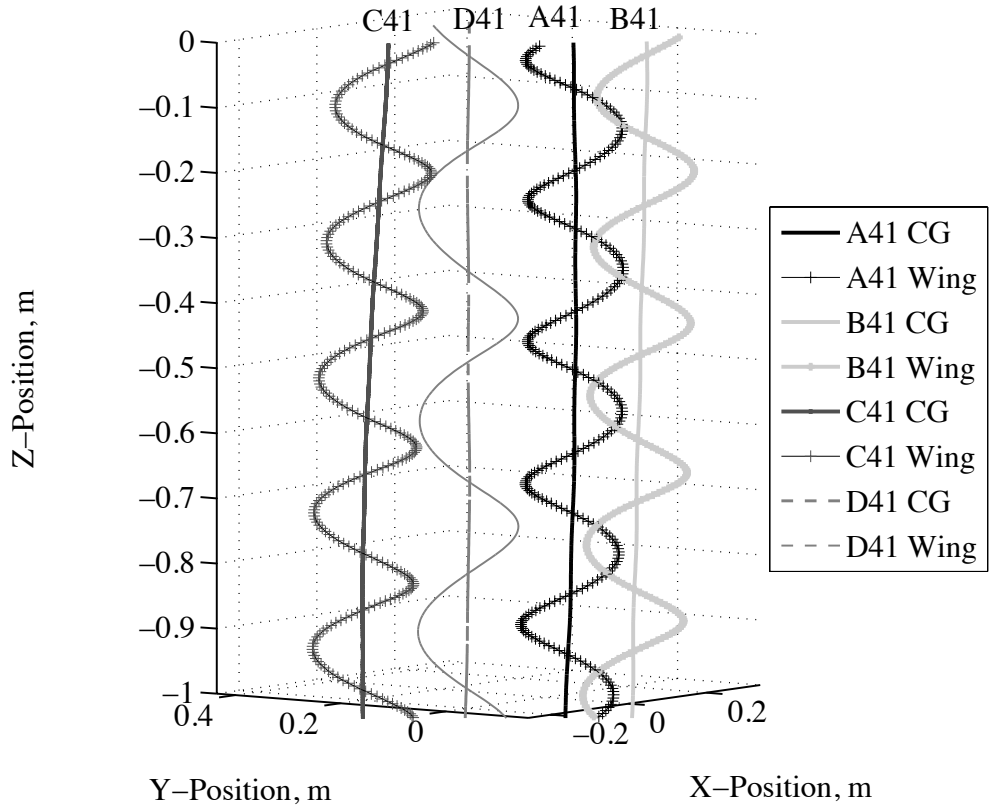

Figure 2.9: Mechanical samara flight path data recorded by Vicon.

A schematic detailing the construction of the vectors is shown in Fig. 2.7. The intermediate vector $\tilde{\delta}_{1,2}$ can be normalized forming the $\tilde{e}_i$ body frame axis. The vector $\tilde{v}$ is formed by normalizing $\tilde{\delta}_{1,3}$; this vector is then used to compute the body frame $\tilde{e}_k$ axis. The final body axis is formed in the cross product of $\tilde{e}_k$ and $\tilde{e}_i$. This set forms the orthonormal basis defining the orientation of the body with respect to the inertial frame.

$$\tilde{e}_i = \frac{\tilde{\delta}_{1,2}}{||\tilde{\delta}_{1,2}||} = \alpha_{11} + \alpha_{21} + \alpha_{31} \tag{2.5}$$

$$\tilde{e}_j = \tilde{e}_k \times \tilde{e}_i = \alpha_{12} + \alpha_{22} + \alpha_{32} \tag{2.6}$$

$$\tilde{e}_k = \tilde{v} \times \tilde{e}_i = \alpha_{13} + \alpha_{23} + \alpha_{33} \tag{2.7}$$

Once the three-dimensional marker position is obtained and the basis set of the samara body axes is computed, the Euler angles can be deduced from the basis $[\tilde{e}_i, \tilde{e}_j, \tilde{e}_k]$. The Euler angles provide a non-unique set of rotations that describe the samaras orientation, however a singularity arises at $\pi/2$. Away from the singularity, the angles are as follows:

$$\theta = \arcsin -\alpha_{13} \tag{2.8}$$

$$\psi = \arctan \frac{\alpha_{11}}{\alpha_{12}} \tag{2.9}$$

$$\phi = \arctan \frac{\alpha_{23}}{\alpha_{33}} \tag{2.10}$$

To maintain continuity of signs between successive time steps near the singularity, it is necessary to set $\psi = 0$ and compute the final angle ϕ as:

$$\phi = \arctan \frac{\alpha_{21}}{\alpha_{31}} \tag{2.11}$$

The computed Euler angles of the various models tested are shown in Fig. 2.12.

2.4.2 Attitude Representation

Subsequent testing of the various samaras provided insight into the governing dynamics as they varied with samara geometry. Attitude representation requires separate bases for the fixed inertial axes (F) and the body axes which are fixed to the samara (B).

$$F = [\hat{f}_x, \hat{f}_y, \hat{f}_z] \tag{2.12}$$

$$B = [\tilde{e}_i, \tilde{e}_j, \tilde{e}_k] \tag{2.13}$$

$$[\vec{r}]_B = R_1(\phi) \cdot R_2(\theta) \cdot R_3(\psi) \cdot [\vec{r}]_F \tag{2.14}$$

A schematic detailing the axis of these rotations is shown in Fig. 2.10. The transformation from the inertial frame to the body frame is described by three Euler angles.

The order of rotation is as follows: a yaw rotation ψ about the $\hat{f}_z$ axis, followed by a pitch rotation θ about the new $\hat{f}_y$ axis, and lastly a coning rotation ϕ about the new $\hat{f}_x$ axis. This rotation sequence is standard for aircraft [19].

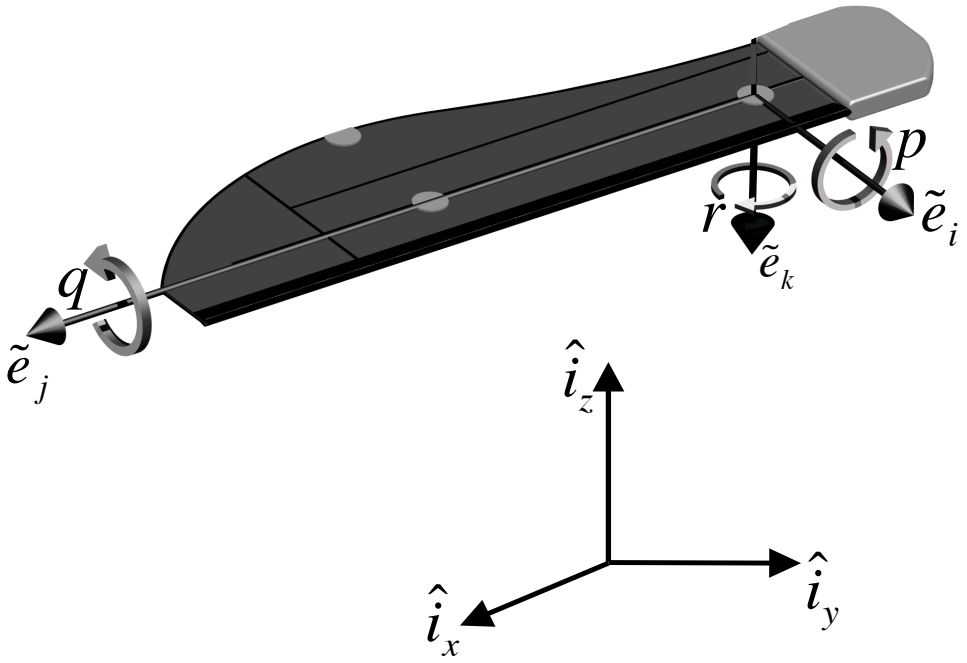

Figure 2.10: Roll (p), Pitch (q) and Yaw (r) definitions for body fixed coordinate system.

Rotations in the fixed body frame (B) are orthogonally projected onto the inertial frame (F), which requires the body angular rates to be defined separately. The sum of the inner products of each of the inertial angular rates with the body axis of interest yields the body angular rates:

$$p = -\dot{\psi}\sin\theta + \dot{\phi} \quad Roll \tag{2.15}$$

$$q = \dot{\psi}\cos\theta\sin\phi + \dot{\theta}\cos\phi \quad Pitch \tag{2.16}$$

$$r = \dot{\psi}\cos\theta\cos\phi - \dot{\theta}\sin\phi \quad Yaw \tag{2.17}$$

The roll, pitch and yaw time histories for each of the samaras tested are displayed in

Fig. 2.142.15.

Table 2.5: Flight performance metrics

Metric	r_{CG}, m	$\sigma_{r_{CG}}, m$	$\dot{z}_{CG}, m/s$	$\sigma_{\dot{z}_{CG}}, m/s$	Y_C, m
$A41$	0.07	0.01	-1.60	0.01	64.60×10^{-3}
$B41$	0.16	0.01	-1.70	0.02	59.00×10^{-3}
$C41$	0.27	0.01	-1.50	0.06	69.80×10^{-3}
$D41$	0.40	0.02	-1.80	0.05	56.20×10^{-3}

2.4.3 Flight Performance

The Euler angles display periodic behavior with varying degrees of phase shift between ϕ and θ for each case. This cyclic behavior can be seen in Fig. 2.12. The scope of flight in this study is characterized by a nearly constant radius of precession, or more precisely a standard deviation, $\sigma_{r_{CG}}$, of no more than 6.25% of the mean. The mean radius of precession r_{CG}, Fig. 2.11, is averaged over N periods (Table 2.6).

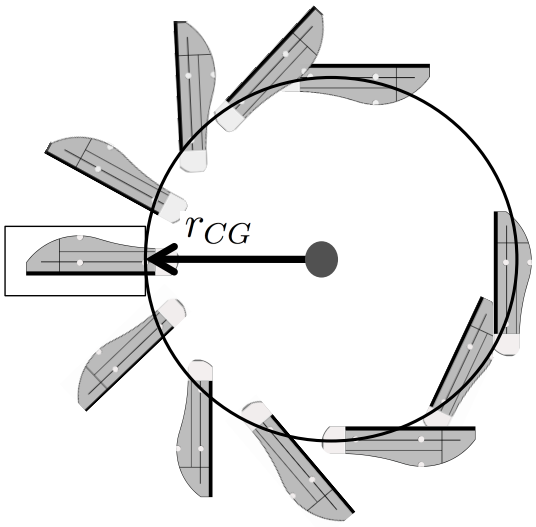

Figure 2.11: Definition of the radius of precession of the center of mass (r_{CG}), [30].

The radius of precession is computed in cylindrical coordinates where $r_{CG} = \sqrt{x_{CG}^2 + y_{CG}^2}$, and (x_{CG}, y_{CG}) denotes the location of the center of mass of the samara,

or M1 from Fig. 2.7. r_{CG} represents the amount of transverse motion in the helical descent trajectory.

The tabulated data shown in Table 2.8 identify key performance parameters, namely the resulting geometry for minimal descent velocity. The samara models rotate about the center of mass or CG, resulting in the majority of the wing area being located on one side of the CG, as shown in the box in Fig. 2.21. The distance of the area centroid of this portion of the samara with respect to the CG is shown in Table 2.8 for the samara models.

The terminal velocity of a natural samara is a function of two parameters: the mass of the samara and the mass of air accelerated by the samara. The control volume of the mass of air accelerated has been defined (by Norberg [17] as a flat disk equal in radius to the wing tip. This definition differs from Green's definition [14] which is limited to the surface area of the samara.

The samara models compared in this study have identical surface area and weight, for which Green's model predicts no variation in descent velocity. Norberg's model accounts for the wing tip radius varying between models resulting in a variation of disk loading. Models A41 and C41 have identical wing tip radii, therefore Norberg's model predicts no variation in descent velocity. Samara models of identical wing loading and disk loading can be quantitatively compared through observation of the location of the wing area centroid relative to the center of mass, or CG of the samara. In Table 2.8 and Fig. 2.16, the centroid location farthest from the CG corresponds to the samara with the lowest descent velocity. To reconcile the erroneous trends predicted by the previously mentioned models, a modified disk loading can be used to predict trends in the terminal velocity of samara. This modified disk loading uses the length (Y_C) between the area centroid and the rotational axis as the radius of the flat disk which defines the control volume of air accelerated by the descending samara. These relationships are shown in Fig. 2.16.

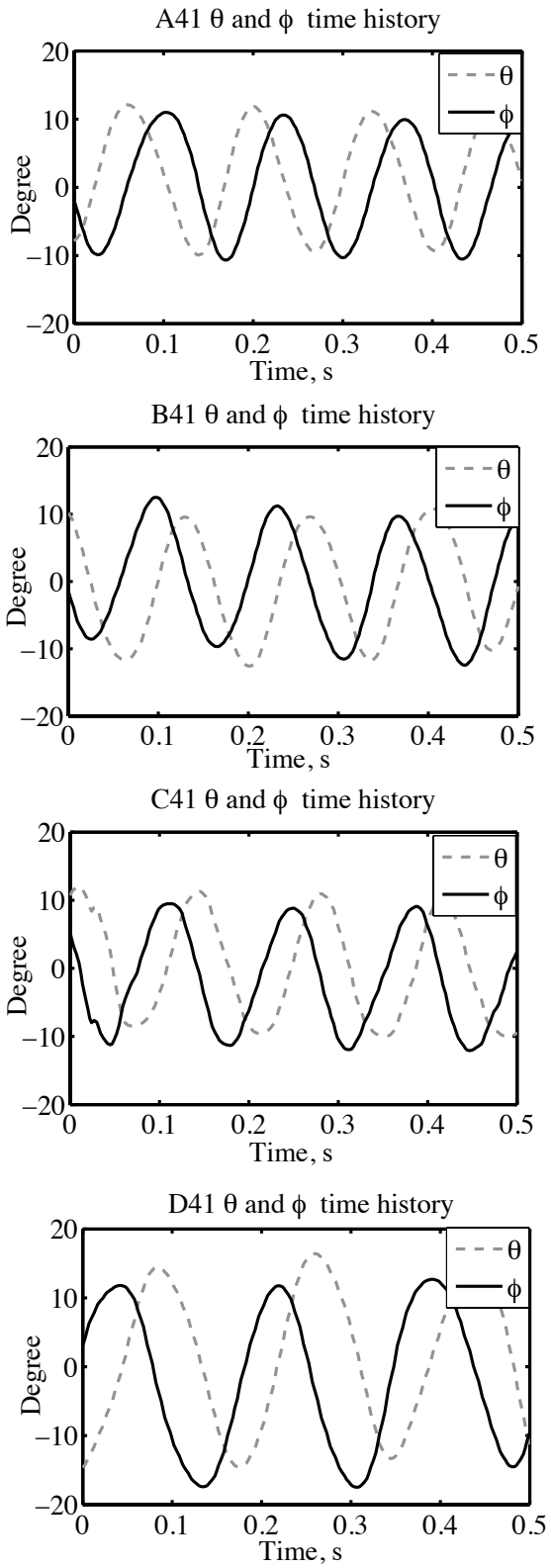

Figure 2.12: Euler angles computed from flight test data.

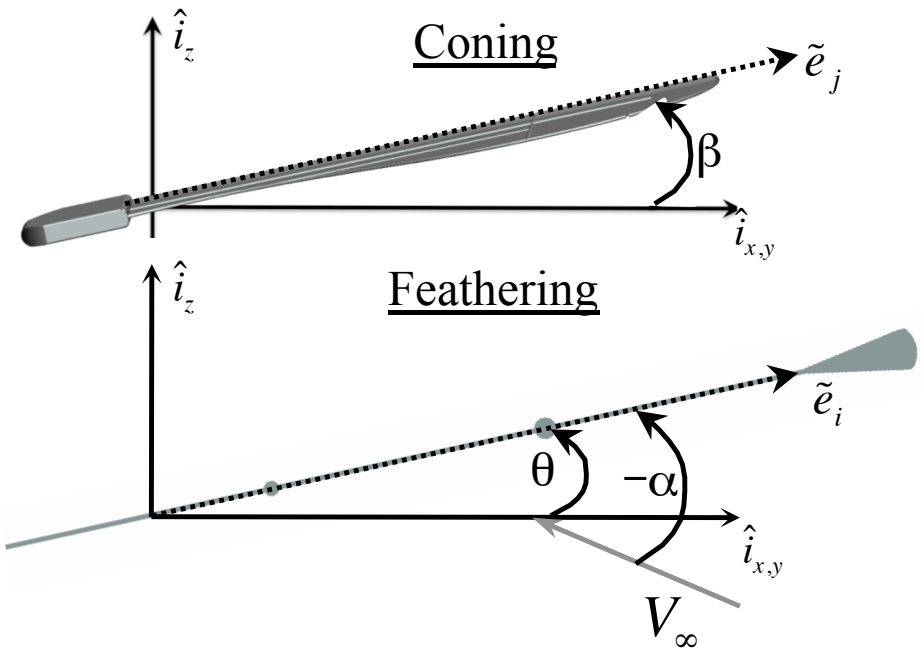

Figure 2.13: Definitions for coning β and feathering θ angles.

2.4.4 Flight Dynamics Analysis

In applications involving periodic signals it is desirable to enhance signal-to-noise ratios in order to extract representative waveforms. Time synchronous averaging (TSA) techniques previously implemented in applications such as structural health monitoring are employed here as a means of reducing a periodic signal into one discernable waveform [59,60]. For a deterministic signal $\chi(t)$ of period T, a measurement model can be written as:

$$\kappa(t) = \chi(t) + \nu(t) \tag{2.18}$$

where ν is additive sensor noise. For $\chi(t)$ measured over N periods, the ensemble average and ensemble variance can be approximated as:

$$\eta_\kappa(t) = \frac{1}{N}\sum_{n=0}^{N-1} \kappa(t + nT) \tag{2.19}$$

$$\sigma_\kappa^2(t) = \frac{1}{N}\sum_{n=0}^{N-1} [\kappa(t + nT) - \eta_\kappa(t)]^2 \tag{2.20}$$

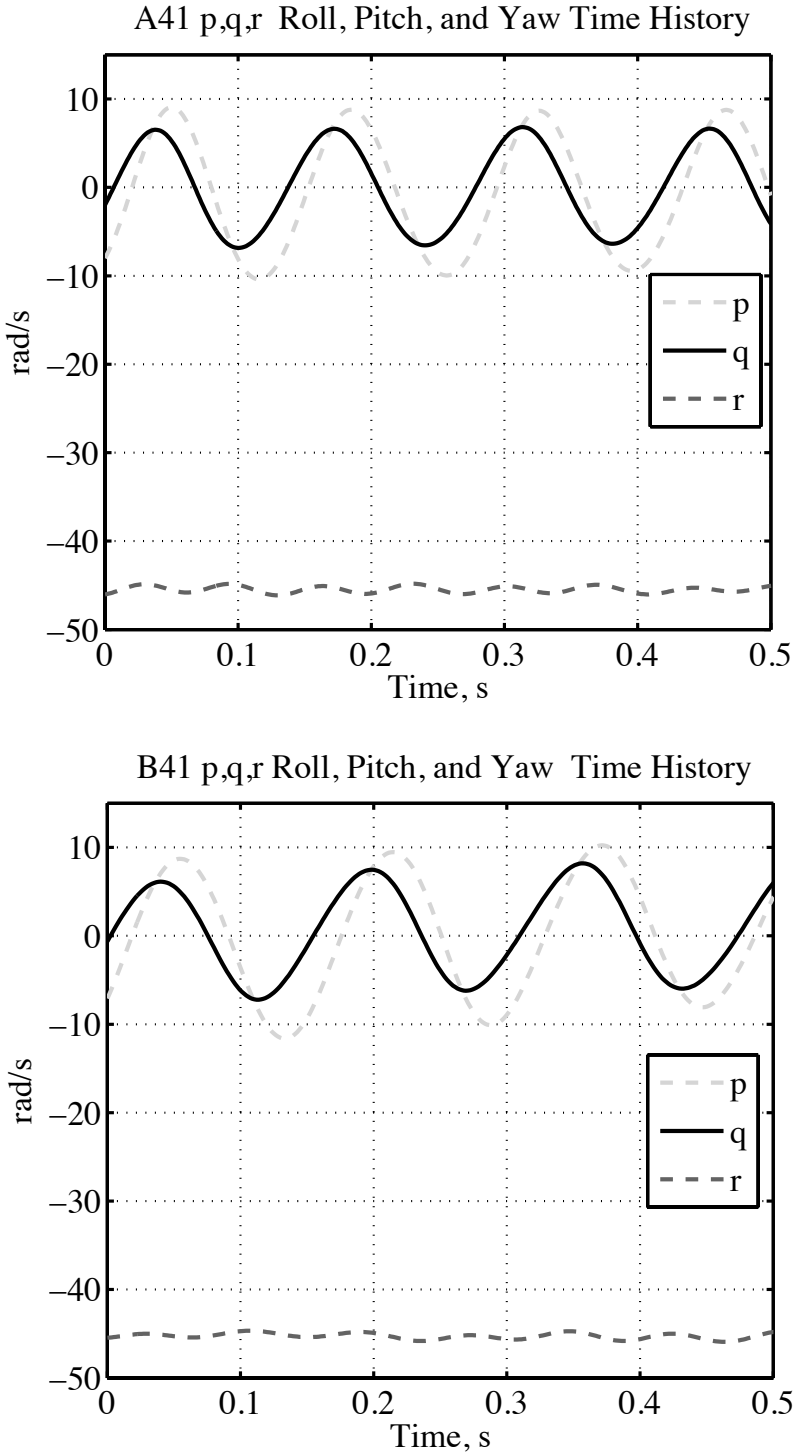

Figure 2.14: Roll (p), Pitch (q) and Yaw (r) rates for the mechanical samara A and B.

Confidence intervals for estimated parameters can be formulated from estimation theory [58]. The 95% confidence interval of these measurements with regard to the

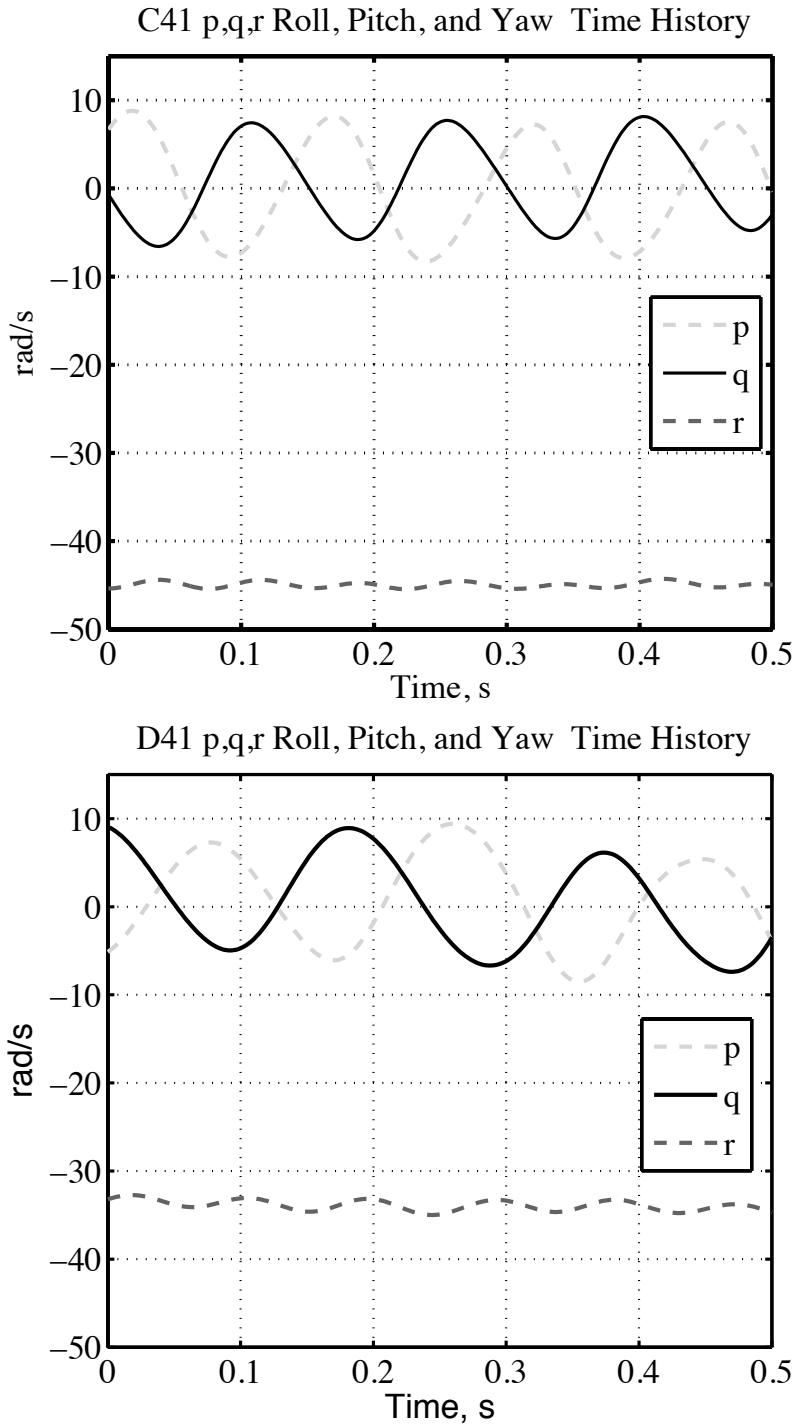

Figure 2.15: Roll (p), Pitch (q) and Yaw (r) rates for the mechanical samara C and D.

signal averages is approximated as:

$$\kappa_{0.95}(t) = \eta_{\chi}(t) \pm 1.96\sigma_{\kappa}(t) \tag{2.21}$$

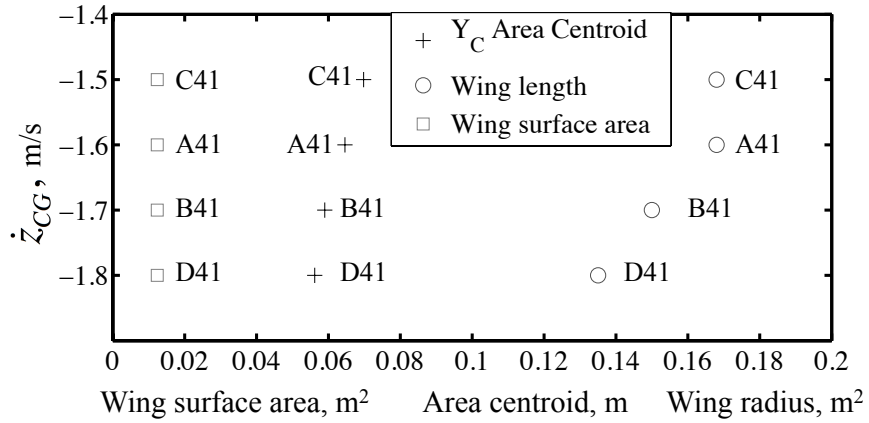

Figure 2.16: Influence of wing radius, wing surface area, and wing area centroid distance from center of mass Y_C, on descent velocity.

This average is then described for each samara by Fourier sine or cosine series of varying order. The specific parameters used for the ensemble averaging are listed in Table 2.6. The roll, pitch, and yaw time histories for each of the subjects are

Table 2.6: Time synchronous average parameters for each samara tested

Model	Term	f, Hz	T, s	points	N
A41	p	7.25	0.138	500	8
A41	q	7.25	0.138	500	8
B41	p	7.41	0.135	384	6
B41	q	7.41	0.135	384	6
C41	p	7.32	0.137	411	7
C41	q	7.32	0.137	411	7
D41	p	5.71	0.175	455	6
D41	q	5.71	0.175	455	6

displayed in Fig. 2.142.15. The concatenated signals are shown in Fig. 2.17 where the gray points are the overlaid signals. The black line is the signal average with the 95% confidence interval on the upper and lower bounds. The confidence interval bounds tend to increase from samara A to D, as shown in Fig. 2.17. Possible causes for this include but are not limited to: structural vibrations, susceptibility to small wind disturbance, and decreased aerodynamic damping resulting from a change in the center of pressure. The number of ensembles averaged is highly dependent on

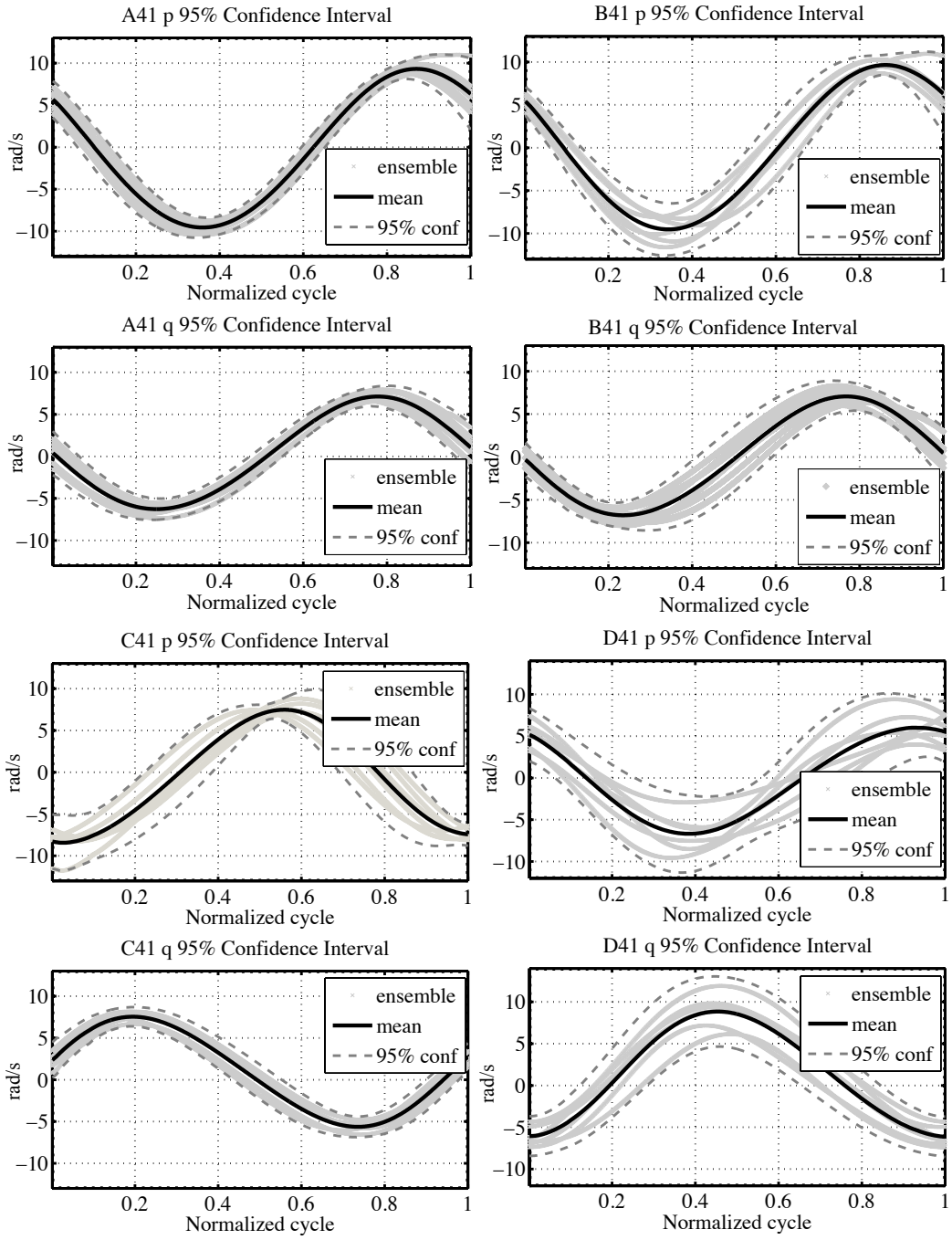

Figure 2.17: TSA flight data with 95% confidence interval.

the settling time of the individual samara and the limited drop height. This number could be increased at the cost of uncertain initial conditions by giving the samara a pre-spin upon launch.

The concatenated roll and pitch flight data can be represented with a Fourier

series allowing a functional representation of the flight dynamics. The curve fits of the four models including the 90% confidence interval are shown in Fig. 2.18,2.19.

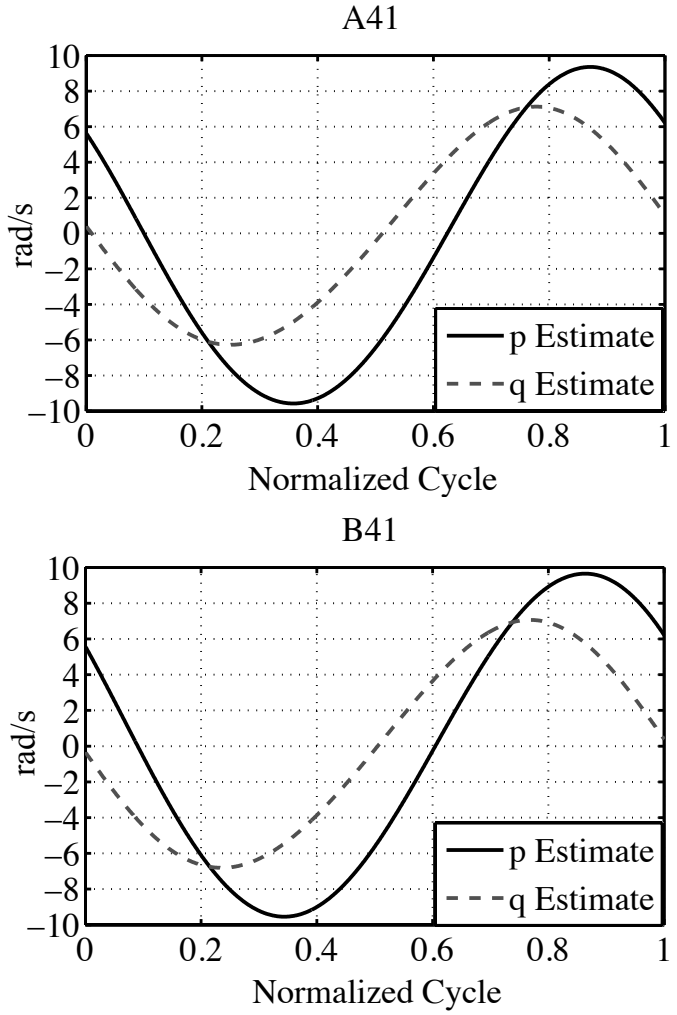

Figure 2.18: Fourier series estimation of TSA roll and pitch flight data

The most notable observation that steady vertical descent, roll and pitch are neither constant nor small as previously suggested by Seter *et al.* (Refs. [20,21]). This has substantial implications as a dynamic model was derived based on a trim state that enforced zero roll and pitch, upon which a number of vehicle design simulations are based Refs. [22, 23]. The waveform indicates a cyclic variation in the roll rate of roughly ± 9.5 rad/s for both A41 and B41 whereas C41 varies by ± 7.5 rad/s and D41 varies from -8 rad/s to 7.5 rad/s. The pitch rate observed in A41 is -6 rad/s to 7

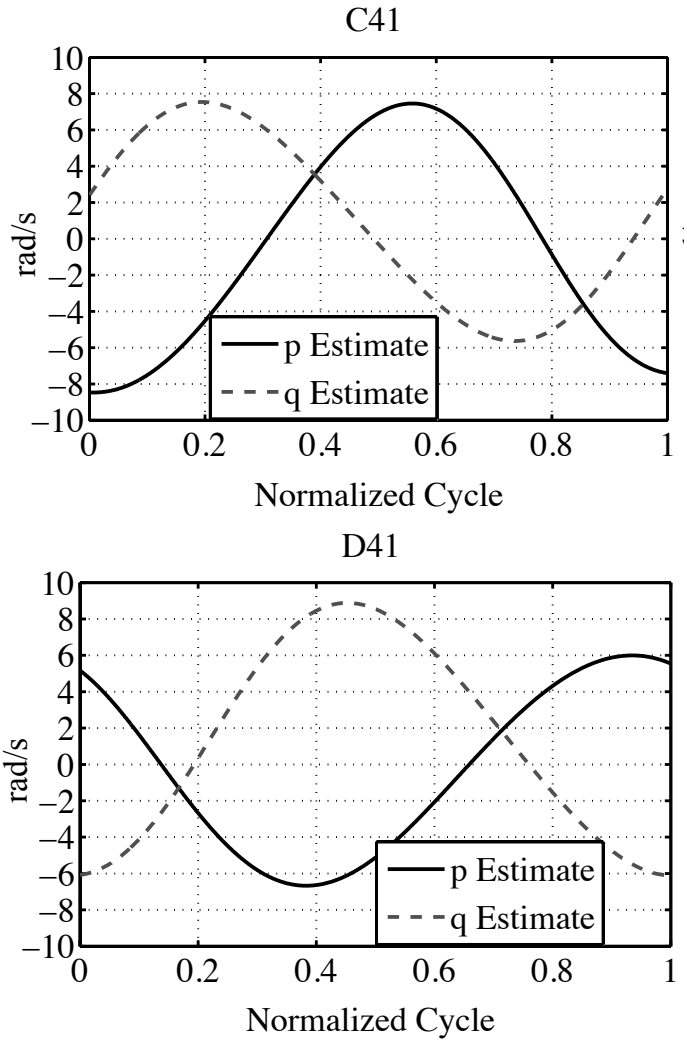

Figure 2.19: Fourier series estimation of TSA roll and pitch flight data

rad/s and is similar in amplitude to B41 which varies by ±7 rad/s. The pitch rates of both C41 and D41 appear to have an offset and are not symmetric about the zero point as observed for A41 and B41. The pitch rate for C41 can be observed to vary from −5.5 rad/s to 7.5 rad/s and for D41 the pitch rate varies from −7.5 rad/s to 10.5 rad/s and exhibits a similar offset as the one observed in C41. The roll and pitch rates are represented by Eq. 2.22− 2.23.

$$\hat{p}_i(t) = a_0 + \sum_{n=1}^{3}[a_n \cos(\omega t) + b_n \sin(\omega t)] \tag{2.22}$$

$$\hat{q}_i(t) = a_0 + \sum_{n=1}^{3}[a_n \cos(\omega t) + b_n \sin(\omega t)] \tag{2.23}$$

where $i = [A, B, C, D]$. The yaw rate and curve fit are neglected here as the variation in amplitude is 2 rad/s or 5% of the mean, and can be approximated with small error as a line. The resultant coefficients of the Fourier series estimate are tabulated and shown in Table 2.7. The observed phase shift in the rotational dynamics, when measured from maximum p to maximum q, varies between the models with A41 and B41 exhibiting similar shifts of 33.0° and 35.6°, respectively. Models C41 and D41 displayed substantially larger phase shifts of 131.7° and 188.7°, respectively. One observed trend is that an increase in phase shift between p and q corresponds to an increase in the radius of precession of the center of mass, r_{CG}.

Table 2.7: Coefficients of the Fourier series estimate of TSA roll and pitch

State	$\omega, rad/s$	a_0	a_1	b_1	a_2	b_2	a_3	b_3	MSE
$\hat{p}_A(t)$	6.206	−0.323	+5.905	−7.398	+0.049	−0.229	−	−	0.789
$\hat{q}_A(t)$	6.194	+0.257	+0.297	−6.677	−0.147	−0.240	−	−	0.024
$\hat{p}_B(t)$	2.773	−1.872	+4.004	+3.147	+3.450	−12.100	−	−	0.696
$\hat{q}_B(t)$	6.185	+0.018	−0.224	−6.912	−0.128	−0.260	−	−	0.225
$\hat{p}_C(t)$	4.059	−2.573	−4.163	+5.055	−1.399	−3.363	−0.331	+0.431	0.386
$\hat{q}_C(t)$	6.334	+0.948	+1.273	+6.392	+0.179	+0.447	−	−	0.091
$\hat{p}_D(t)$	2.947	−2.462	+0.172	+4.173	+7.113	−4.525	+0.341	−1.170	0.118
$\hat{q}_D(t)$	6.180	+1.349	−7.254	+1.627	−0.175	−0.460	−	−	0.598

2.4.5 Observations from Free Flight Test

The two flight modalities identified, shown in Fig. 2.20^i, have been observed on all scale models tested. The major differences found include mean feathering/coning angles, radius of precession, and descent velocity. The coning and feathering angles from mode (I) averaged $\bar{\beta} = 10.1^o$ with $\sigma_\beta = 1.6^o$, and $\bar{\theta} = 2.4^o$ with $\sigma_\theta = 1.8^o$, Fig. 2.20^a. Flight mode (II) exhibited larger oscillations in coning and feathering with $\bar{\beta} = 8.6^o$ with $\sigma_\beta = 6.1^o$, and $\bar{\theta} = 1.3^o$ with $\sigma_\theta = 7.4^o$, Fig. 2.20^b. The body angular velocities were found to be substantial and varying by as much as 20 Rad/s

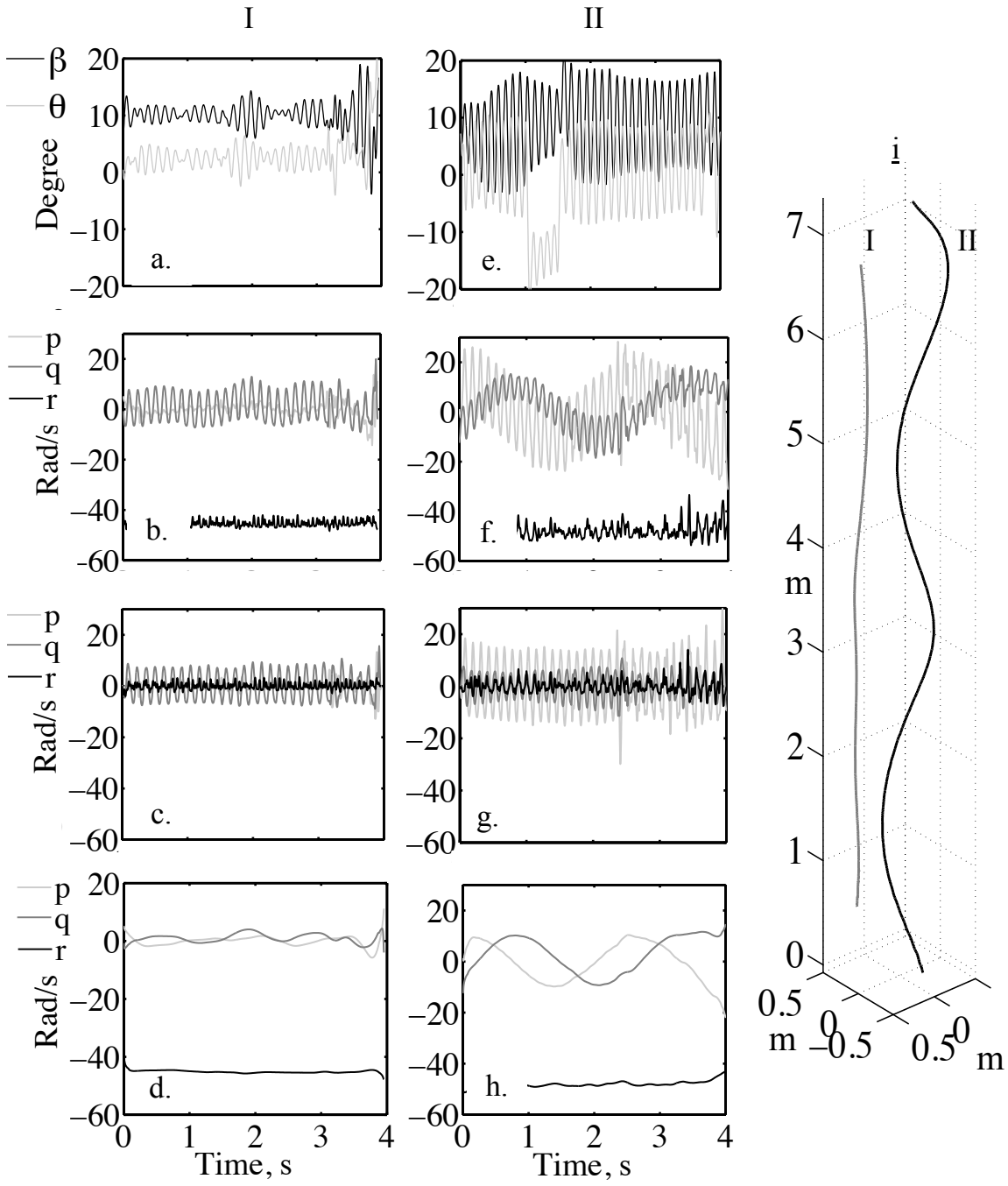

Figure 2.20: Mechanical samara flight path data recorded by Vicon.

in the roll (p) and pitch (q) axis, which have been previously reported or assumed to be constant and negligible by all previous work, Fig. 2.20^{b,f}. Roll, pitch, and yaw for both flight modes display cyclic (once per revolution) and low frequency (< 1 Hz) oscillations. Shown in Fig. 2.20^{c,g} is the oscillatory excitation of (p, q, r) that

occurs near the rotational frequency r, and shown in Fig. 2.20[d,h] is the low frequency excitation that occurs at 0.7 Hz for the first mode (I) and 0.4 Hz for the second mode (II).

The tabulated data shown in Table 2.8 identifies key performance parameters, namely the resulting geometry for minimal descent velocity. The samara models rotate about the center of mass or CG, resulting in the majority of the wing area being located on one side of the CG, as shown in the box in Fig. 2.21. The distance of the area centroid of this portion of the samaras are calculated with respect to the CG, and is called Y_c and quantified in Table 2.8.

The second mode observed traced a 0.5 m diameter circle upon descent, whereas the first mode settled to trace a circle with diameter equal to 0.06 m. In both cases the variations in roll and pitch display cyclic behavior at a frequency different than that of the yaw rotation. The two differing flight paths begin with identical initial conditions for the same samara. The seemingly chaotic tumble into stable autorotation was not observed in detail.

Table 2.8: Flight performance metrics

Metric	r_{CG}, m	$\sigma_{r_{CG}}, m$	$\dot{z}_{CG}, m/s$	$\sigma_{\dot{z}_{CG}}, m/s$	Y_C, m
$A41$	0.07	0.01	-1.60	0.01	64.60×10^{-3}
$B41$	0.16	0.01	-1.70	0.02	59.00×10^{-3}
$C41$	0.03	0.01	-1.50	0.06	69.80×10^{-3}
$D41$	0.40	0.02	-1.80	0.05	56.20×10^{-3}

2.5 Summary

A new approach to the study of micro-scale flight that incorporates vision-based motion capture has elucidated the effects of wing geometry on mechanical samara autorotation and rotational dynamics. The flight data captured with this approach are the most precise to date and have resulted in the characterization of previously

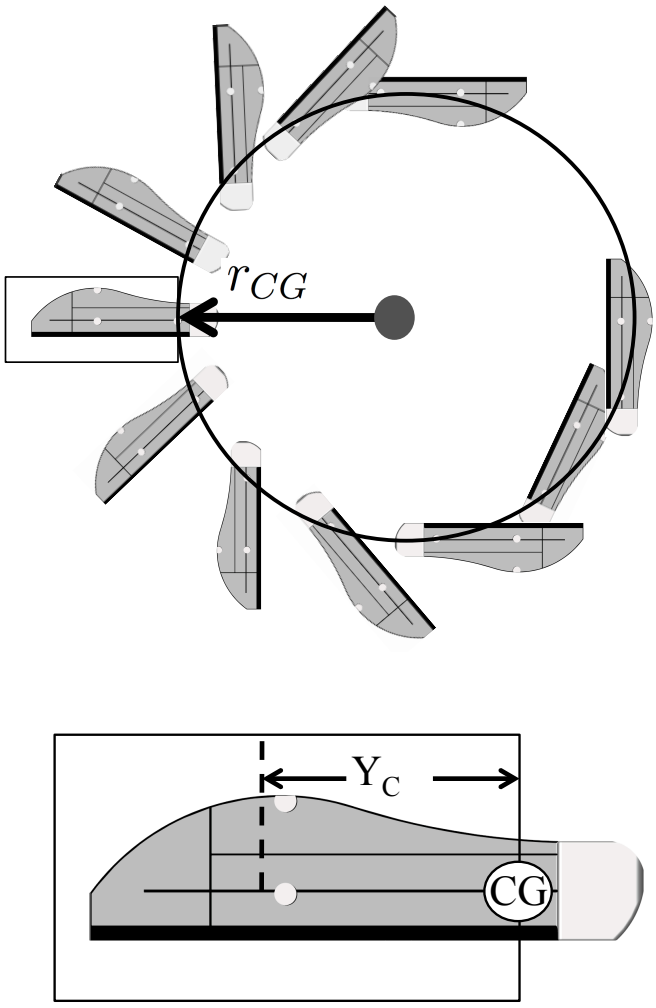

Figure 2.21: Area of wing used to compute Y_C. Also shown is the definition of the radius of precession of the center of mass (r_{CG}), [30].

unobserved roll and pitch dynamics. The different planform geometries of the samara tested resulted in a variation in descent velocity by as much as 16.7%. The C41 geometry has the minimal descent velocity. Four new mechanical samara designs were presented. A simulated electronics payload of 4.5 grams was molded into the model to demonstrate the vehicle's ability to safely deliver sensitive hardware by preventing ballistic descent with consistent autorotation. A new airfoil derived from natural samara chord geometry was presented and tested. The radius of precession of the center of mass r_{CG} was found to vary by $> 500\%$ among models. A linear

relationship was established between the location of the area centroid with respect to the center of mass, Y_C, and the vertical descent velocity, $\dot{z}_{CG}$, capturing the trends observed by varying planform geometry.

Chapter 3

System Design of a Robotic Samara Micro Air Vehicle

3.1 Introduction

Design of the monocopter is difficult as there is a lack of literature on design principals. Efforts to scale down the conventional configuration are numerous but have failed to create a stable and controllable vehicle that can be flown outdoors where its usefulness can be realized. The iterative design process outlined here resulted in a number of vehicles that are substantially smaller than those previously constructed and flown. The design space filled by this scale of rotorcraft is shown in Fig 3.1 and is one of the main contributions of this work.

Beginning with design constraints that maintain the inertial layout of a natural samara, a number of fully controllable vehicle were constructed. The initial prototypes are presented in chronological order. This is followed by the general configuration and discussion of the final design iteration. The motor orientation, wing planform design, and connection between the two is discussed and flight performance metrics are given for 3 different size vehicles. Finally the first at-scale robotic maple seed or samara is

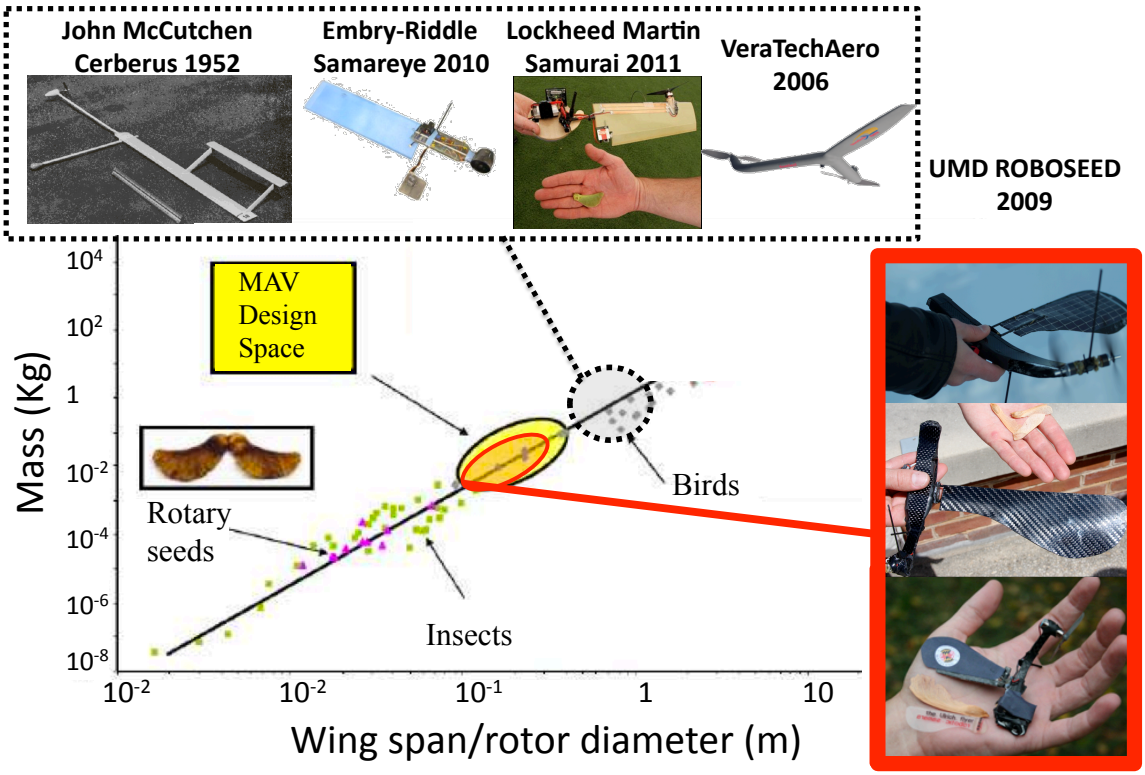

Figure 3.1: Mass vs Wing span. The prototypes constructed in this work are substantially smaller than other mono-wing rotorcraft and set the lower limit for aircraft of this kind.

described and discussed.

3.2 Vehicle Design

The unconventional wing and body structure are the result of an iterative design process which has produced on the order of one-hundred vehicle designs. The resultant vehicles are damage tolerant as they employ flexible structures which deflect upon impact, effectively increasing the time over which the impact load is applied to the vehicle. Advantages over traditional micro-scaled vertical take-off and landing (VTOL) configurations include passive stability, efficient autorotation, low body drag, mechanical simplicity, low cost, high payload capacity, and substantial damage tolerance. The first prototype capable of flight, Figure 3.2, was primarily made of rapid

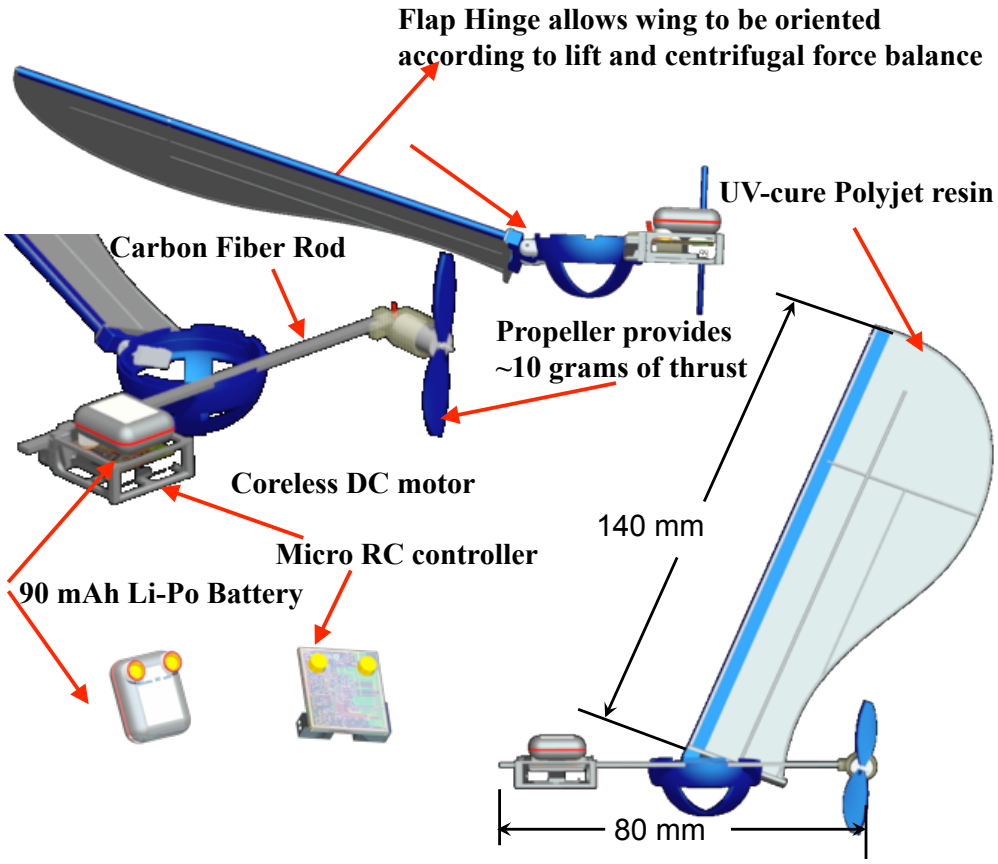

Figure 3.2: First robotic samara to take flight.

prototyped plastic, however the main structural spar is made of carbon fiber. The wing used is a modified C41 that has a hinge in place of the mass. The wing's connection to the main fuselage is through a passive flap hinge that allows the lead/lag and flap degree's of freedom. In flight the wing's coning angle is proportional to the mass and rotational velocity of the wing, balanced by the lift generated by the wing. This model was unable to adjust the wing pitch angle in flight and was only controllable in the vertical direction. Another limitation of the vehicle is its inability to autorotate as the there is no way to decreases the angle of attack of the wing to prevent stall when motor torque drops off. The motor used is an off the shelf pager motor with a maximum output of 3 Watts with a two-bladed propellor. One of the difficulties in initial launch of the vehicle is to maintain the wing and motor orientation as there

is an undamped and free hinge connecting the two. This was overcome by adding a type of landing gear that prevented the propellor from impacting the ground on takeoff and landing ensuring proper orientation of the vehicle.

The next scaled up prototype incorporated the same passive flap hinge with a larger rapid prototyped wing, as seen in Figure 3.3. To mitigate the previous designs issues with ground impingement and takeoff orientation the open motor with a kick stand was replaced with a larger and more powerful ducted fan. The structure was made of parallel carbon fiber beams that directly attached to the motor and battery across the central flap hinge/receiver section. Flight was very noisy as the duct acted like pipe. Vertical control was possible through an increase in the throttle and the vehicle could takeoff and land without issue. The vehicle was fragile and any impact with its surrounding shattered the wing.

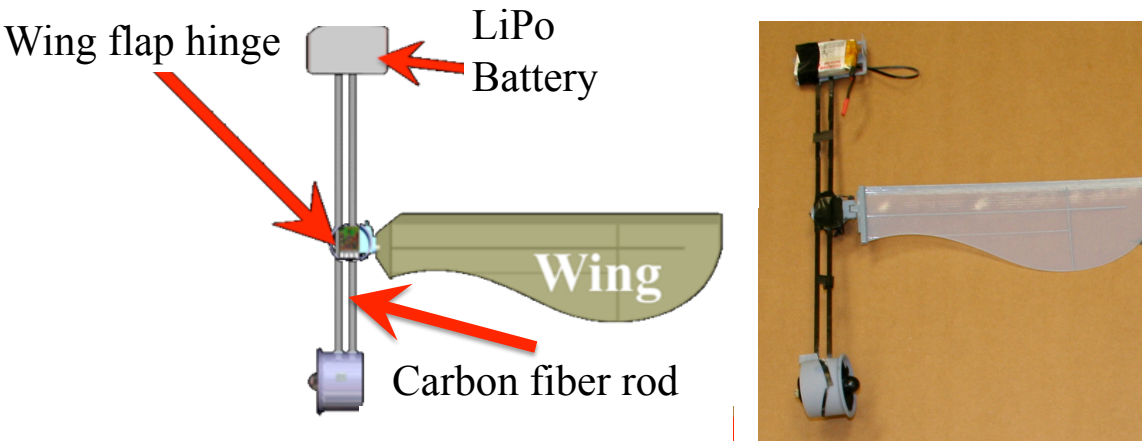

Figure 3.3: Ducted dan and flap hinge samara prototype.

The addition of a servo to control the wing pitch allows for vertical control without variation of the throttle, Figure 3.4. The flap hinge required some damping and in future iterations the hinge was replaced entirely and the wing has the flexibility needed to act as a flap hinge.

The smallest vehicle constructed with variable wing pitch can be seen in Figure 3.5. The wing pitch is varied by a shape memory alloy actuator that was low power and

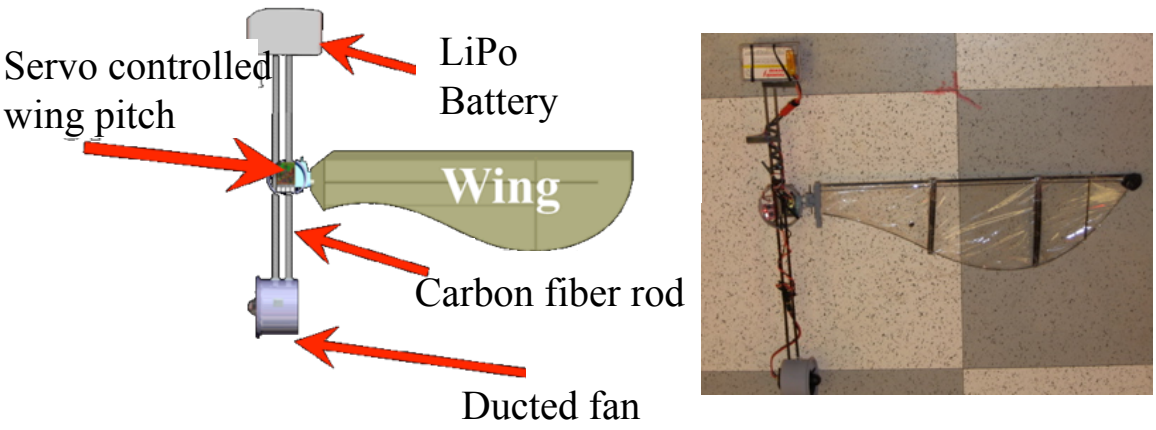

Figure 3.4: Ducted dan and servo control with flap hinge samara prototype.

low weight (0.9 g). The total weight of the vehicle is 9.5 g and its maximum dimension is 12.5 cm and is well within the minimum dimensions set by DARPA. The brushless pager motor has a maximum output of 3 Watts with a 90 mAh LiPo battery and uses a two bladed propellor.

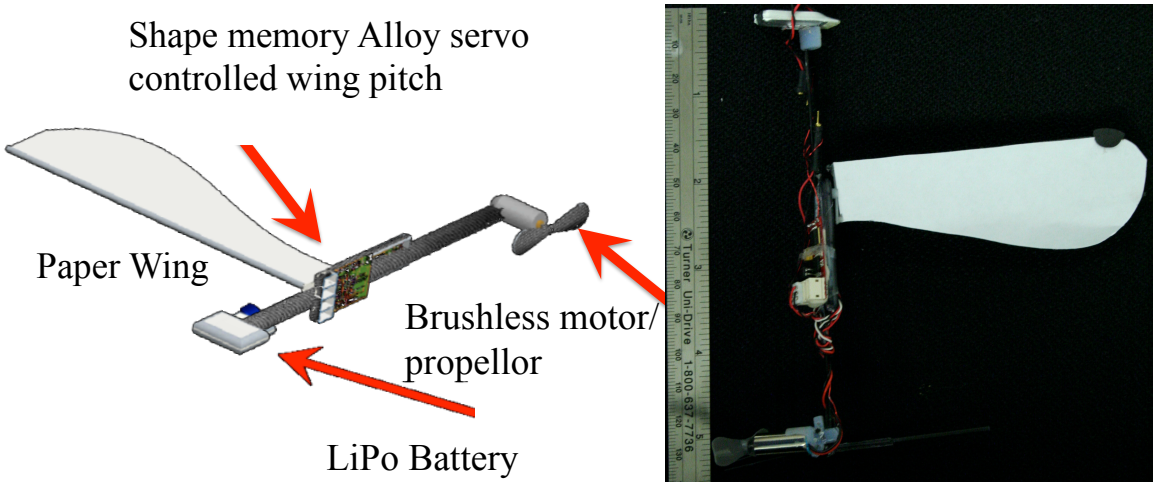

Figure 3.5: Robotic samara vehicle incorporating a shape memory allow servo for wing pitch control.

The vehicle shown in Fig 3.6 incorporates the lessons learned from the design iterations. This prototype is described in detail in the following paragraphs and is the vehicle used in the testing and characterization of the flight dynamics and control experiments covered in the chapters to come.

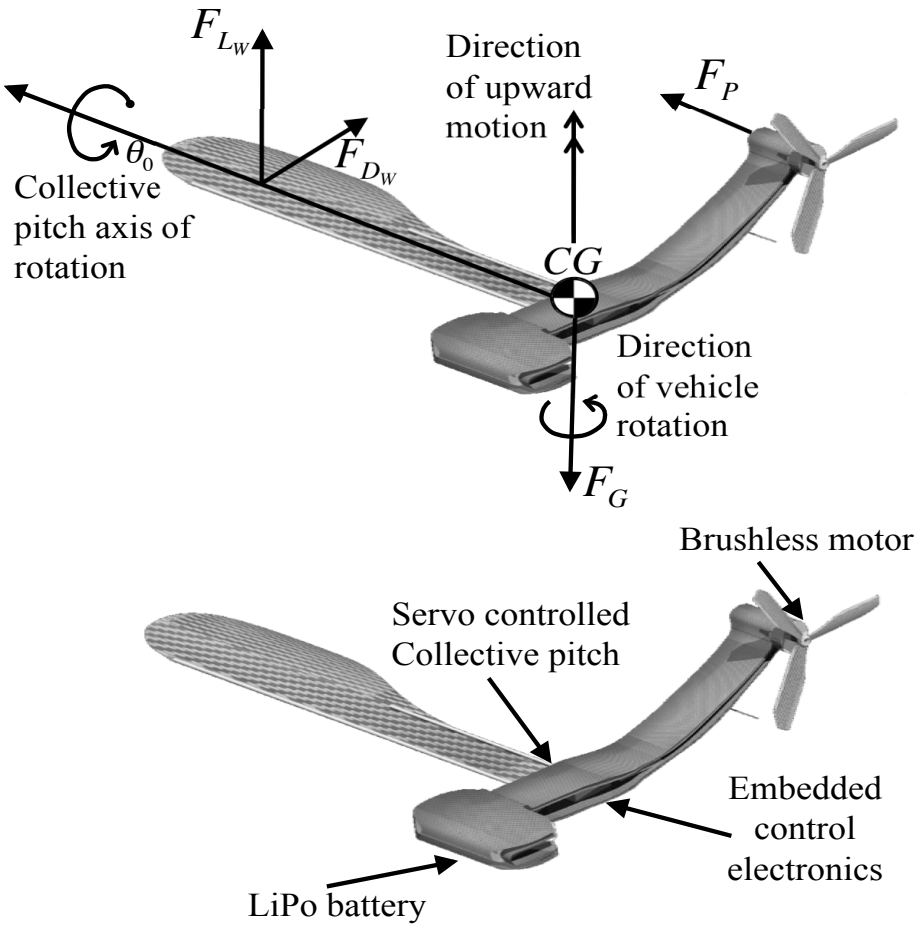

Figure 3.6: Robotic samara component and free body diagram. All structural components are made of carbon fiber. This configuration is used for all the subsequent testing and flight dynamic analysis.

3.2.1 Structures

The primary load-bearing structure of the vehicle is 0/90 ply .025 thick carbon-fiber composite laminate, with opposed parallel tension and compression members mounted to the motor and wing. In this configuration the structure provides a high degree of flexure in the $\hat{c}_z$-direction and a high degree of stiffness in the plane of rotation.

3.2.2 Landing gear and Motor orientation

The angle at which the motor is held provides protection from ground impingement on take-off and landing.

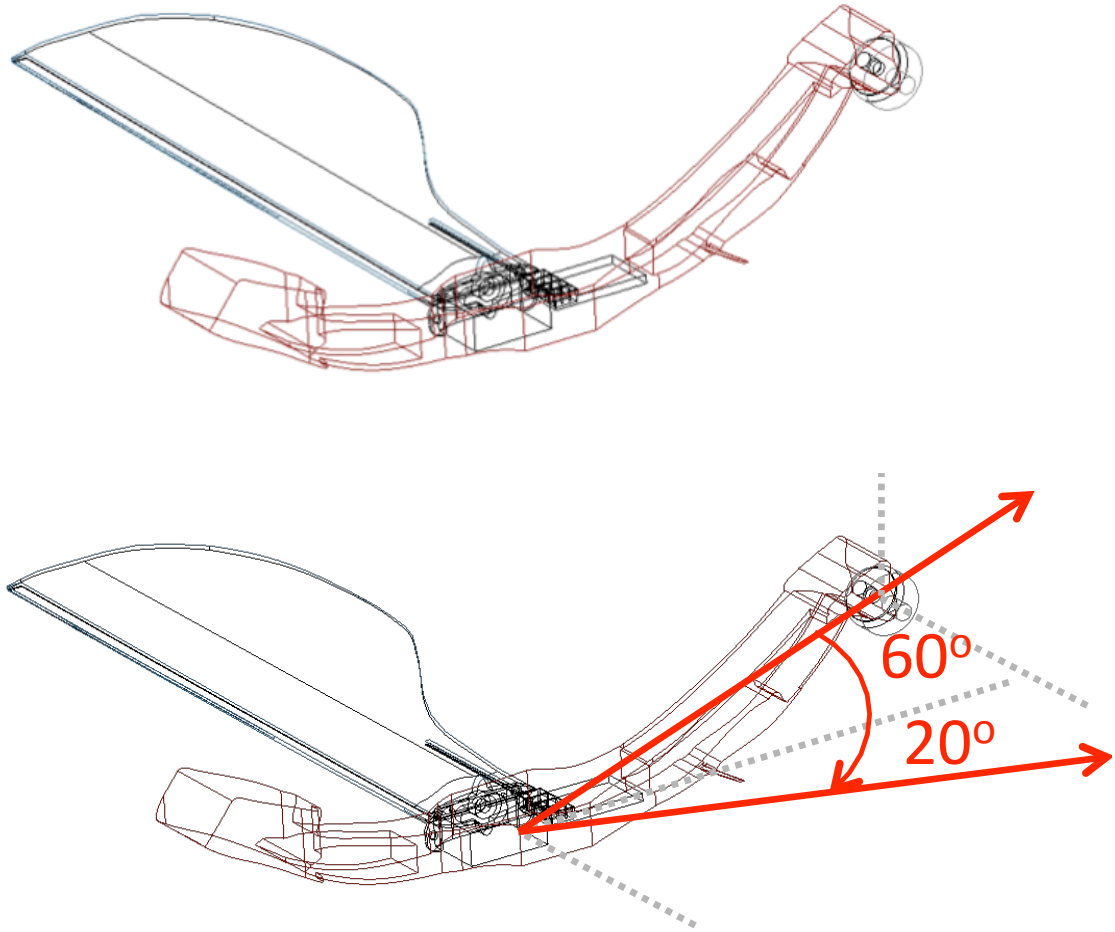

Figure 3.7: Fuselage range of acceptable angles.

The fuselage range of acceptable angles is shown in Fig. 3.7 the arm connecting the motor to the wing and the arm connecting the battery to the wing have the same range of acceptable angles for stable controlled flight. The fuselage is shown in red.

The Motor/propellor range of acceptable angles is shown in Fig. 3.8 the motor/propellor acceptable angles for stable controlled flight range from a positive 45^o (angling the thrust vertically) to -90^o.

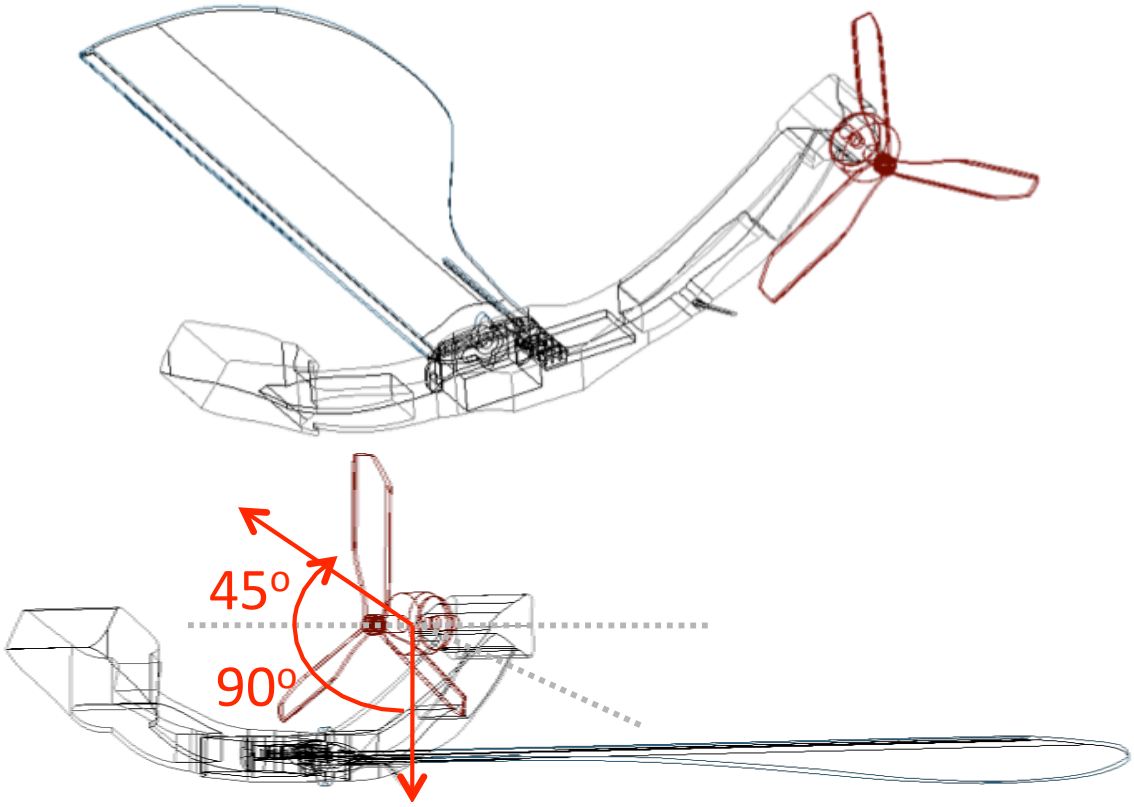

Figure 3.8: Fuselage range of acceptable angles.

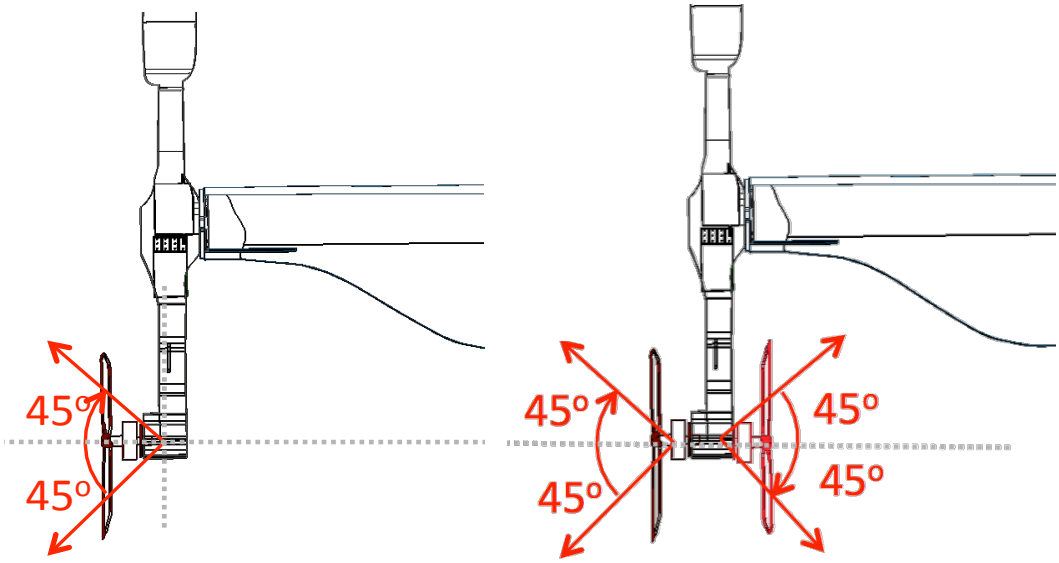

Figure 3.9: Motor/propellor range of acceptable angles.

The motor/propellor acceptable angles for stable controlled flight range from -45^o (angling the thrust toward the CG) which tends to increase stability) to +45^o (angling the thrust away from the CG) which tends to decrease hover stability by causing an increasingly larger circular path, Fig. 3.9. The double motor/propellor setup has more power and can lift more payload and has the added bonus of single motor out operability, Fig. 3.9. The props can spin in either the same or opposite directions as there is no need to cancel the torque from the propellor.

3.2.3 Power and Propulsion

Flight time of the samara-I is roughly 20 minutes with a 25 g, 480 mAh 7.4 V two-cell Lithium-Polymer (LiPo) battery, for a total vehicle mass (GW) of 75 g. The maximum gross take-off weight (GTOW) of the vehicle is 125 g, and the maximum dimension is 270 mm. The second and smaller samara tested, called samara-II is designed and constructed in a similar fashion to samara-I. However, the total mass is 38 g, and maximum dimension is 180 mm. The smallest of the robotic samaras has a maximum dimension of 75 mm, samara-III is powered by a 60 mAh 3.4 V single-cell LiPo battery and has a maximum flight time of 2 minutes. This vehicle has a passive flap hinge, which reduces control to the vertical axis. Table 3.3 details the mass breakdown of samara-I,II and III.

3.3 Aerodynamics

In the derivation of the aerodynamic environment for the samara it is convenient to borrow from helicopter aerodynamics the blade element/momentum theory of Glauert and Gessow. Applying the conservation laws of axial momentum, angular momentum and energy, an expression for the vertical force dT is obtained as applied to the annular element by the fluid passing through it. This method is commonly known as the Blade

Element Momentum Theory or BEMT and allows for the inclusion of blade geometry, section orientation, airfoil characteristics and sectional twist for the calculation of the inflow distribution along the blade.

The remaining performance parameters require a solution to the inflow equation to properly estimate. Flight data collected on the robotic samara's provides a means of approximating the rotation rate, while the blade geometry, mass, and disk area are calculable from the CAD models and prototypes. A MATLAB script was written that allowed for the approximations to be iterated upon and improved resulting in the performance parameters found in table 3.1. The theory used for these calculations is derived below.

3.3.1 Derivation of BEMT equations

The circle carved out by the rotating blade is used as the disk area and is discretized into concentric annuli of area $dA = 2\pi y dy$ as shown in Figure 3.10. A rotor

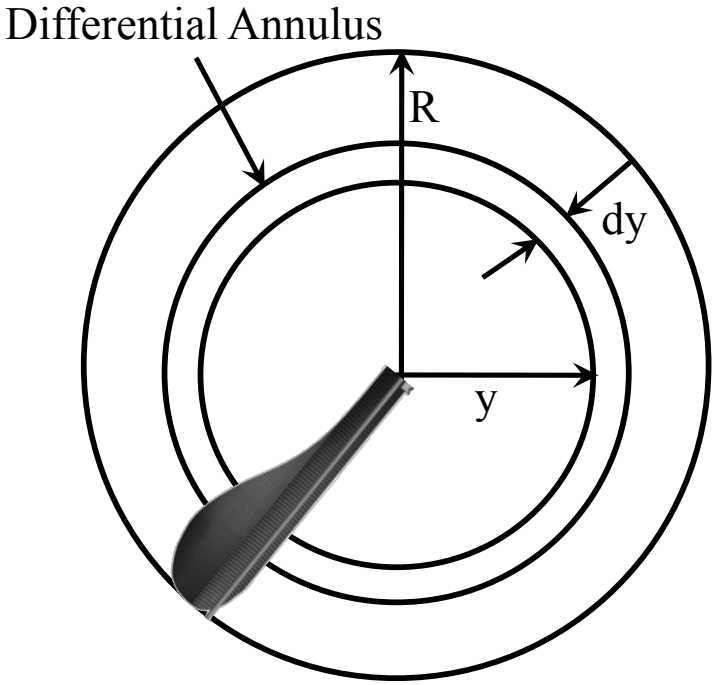

Figure 3.10: Annular element.

in vertical axial flight creates a downward force that is proportional to the rotor disk area and the climb (V_c) and inflow (v_i) velocities. This can be calculated using a simple one dimensional momentum theory approach, as such the thrust produced by each annulus is:

$$\partial T = 2\rho(V_c + v_i)v_i dA = 4\pi\rho(V_c + v_i)y\partial y \tag{3.1}$$

Normalizing the differential thrust equation yields the thrust coefficient

$$\partial C_T = \frac{2\rho(V_c + v_i)v_i dA}{\rho\pi R^2(\Omega R)^2} = 4\frac{V_c + v_i}{\Omega R}(\frac{v_i}{\Omega R})(\frac{y}{R})\partial(\frac{y}{R}). \tag{3.2}$$

The total inflow ratio λ and the induced inflow ratio λ_i can be substituted into the above equation to simplify the expression which then becomes

$$\partial C_T = 4\lambda\lambda_i\partial r = 4\lambda(\lambda - \lambda_c)r\partial r. \tag{3.3}$$

Where λ_c is the component of the total inflow ratio that is produced from the climb speed of the rotor. Applying blade element theory (BET) to the rotor annuli the incremental thrust coefficient is:

$$\partial C_T = \frac{1}{2}\sigma C_l r^2 \partial r = \frac{\sigma C_{l_\alpha}}{2}(\theta r^2 - \lambda r)\partial r. \tag{3.4}$$

Next the previous two expressions from blade element and momentum theory are combined to obtain a quadratic equation which can be simplified and put in canonical form as:

$$\lambda^2 + (\frac{\sigma C_{l_\alpha}}{8} - \lambda_c)\lambda - \frac{\sigma C_{l_\alpha}}{8}\theta r = 0. \tag{3.5}$$

For a hovering rotor $\lambda_c = 0$ and the above quadratic simplifies to the following:

$$\lambda(r) = \frac{\sigma C_{l_\alpha}}{16}[\sqrt{1 + \frac{32}{\sigma C_{l_\alpha}}\theta r} - 1]. \tag{3.6}$$

These equations are typically solved numerically by discretizing the blades into a series of elements. The rotor inflow ration at each blade element n, $\lambda(r_n)$ for a hovering rotor is then solved for and is represented by:

$$\lambda(r_n) = \frac{\sigma C_{l_\alpha}}{16}[\sqrt{1 + \frac{32}{\sigma C_{l_\alpha}}\theta(r_n)r_n} - 1]. \tag{3.7}$$

where r_n and $\theta(r_n)$ are the radius and pitch angle at each of the n elements. This representation allows for the solution of the inflow as a function of the radius for any blade geometry and airfoil section. Once the inflow is determined numerically the incremental thrust of each blade element is:

$$\Delta C_T = \frac{\sigma C_{l_\alpha}}{2}(\theta(r_n){r_n}^2 - \lambda(r_n)r_n)\Delta r \tag{3.8}$$

The total thrust is calculated by numerically integrating over the entire blade. The induced C_{P_i} and profile C_{P_0} power coefficients are as well found by numerically integrating over the blade and can be represented as:

$$C_{P_i} = \int_{r=0}^{r=1} \lambda dC_T \tag{3.9}$$

$$C_{P_o} = \int_{r=0}^{r=1} C_d(r)r^3 dr \tag{3.10}$$

The induced power factor is calculated after the induced power coefficient and thrust coefficient have been found and is calculated as:

$$\kappa = \frac{C_{P_i}}{C_T^{\frac{3}{2}}/\sqrt{2}} \tag{3.11}$$

The inclusion of the viscous losses in the preceding section is done through the airfoils drag coefficient. Below the stall angle of attach the drag coefficient in this analysis is

approximated by a second order polynomial in α as:

$$C_d(\alpha) = C_{d_0} + d_1\alpha + d_2\alpha^2. \tag{3.12}$$

Where d_1 and d_2 are empirically determined coefficients. Values typically used in full scale helicopters airfoils are $C_{d_0} = 0.01$, $d_1 = 0.025$, and $d_2 = 0.65$. Also included are the induced losses resulting from a non-uniform inflow distribution, however the induced effects of the finite number of blades have yet to be incorporated into the present model. The pressure differences between the upper and lower surfaces produce losses near the tip and root of the blade. In these regions there is an increased inflow that effectively reduces the induced angles of attack. Including the tip losses results in an inflow distribution with zero lift production at the inner and outer most sections of the blade. Prandtl derived a factor to adjust the inflow as a function of the number of blades N_b and radial position r. This tip loss function is incorporated into the model of the blade. The correction factor called F is given by:

$$F = (\frac{2}{\pi})cos^{-1}e^f. \tag{3.13}$$

where f is:

$$f = \frac{N_b}{2}(\frac{1-r}{r\phi}). \tag{3.14}$$

In the above equation the inflow angle ϕ is a function of the inflow and the radial position:

$$\phi = \frac{\lambda(r)}{r}. \tag{3.15}$$

Including the tip loss factor results in a modification of the momentum equation of the differential thrust coefficient. In the present case for a hovering rotor ($\lambda_c = 0$) Eq. 3.3 becomes:

$$\partial C_T = 4F\lambda^2 r. \tag{3.16}$$

The differential thrust coefficient from BET can be equated with Eq. 3.16 to form a quadratic equation in λ. Following the same procedure as before an expression for the inflow as a function of the radial position is obtained:

$$\lambda(r) = \frac{\sigma C_{l_\alpha}}{16F}[\sqrt{1 + \frac{32F}{\sigma C_{l_\alpha}}\theta r} - 1]. \tag{3.17}$$

The solution to Eq. must be done iteratively as F is a function of λ. An initial value of $F = 1$ is used and the resultant λ is used in Eq. 3.13 to recalculate F. The airfoil cross section used in the samara tested vary only in chord length and for the purpose of calculating the helicopter performance parameters are assumed to have the same lift and drag coefficients.

Table 3.1: Aerodynamic Performance Parameters.

Samara	I	II	III
Hover Power Watt	1.80	0.77	0.19
Watts/Kg	24.03	20.25	20.29
Induced Power Factor κ	1.4	1.4	1.4
Figure of Merit	0.53	0.81	0.69
Cp	0.0006	0.0024	0.0735
Cp_i	0.0004	0.0020	0.0730
Cp_0	0.0002	0.0004	0.0005
Disk Loading N/m^2	3.21	3.66	5.27
Power Loading $N/Watt$	2.45	2.06	2.07
Cd_0	0.04	0.04	0.04
Rotor Solidity σ	0.043	0.083	0.102
C_T	0.0056	0.0160	0.1758

3.4 Hover power and Efficiency

The efficiency of hovering flight can be evaluated using power loading, PL, as a metric. Hover power loading is an absolute measure of efficiency as it represents the ratio of the thrust produced by the lifting aerodynamic surfaces per unit power

expended to produce the thrust:

$$PL = \frac{T}{P} = \frac{W}{P} \tag{3.18}$$

Here it is assumed that the total thrust is equal to the weight. The disk loading is defined as:

$$DL = \frac{T}{A} \tag{3.19}$$

where A is the effective disk area and is computed from the rotor disk area, $A = \pi R^2$, where R is the radius of the rotor.

Classic momentum theory embodies the principals of conservation of mass, momentum, and energy and can be applied to a control volume surrounding a conventional rotor, [31] [32], or flapping wing system, [15]. This assumes an ideal quasi-steady, one-dimensional, incompressible and inviscid flow and predicts the minimum induced power required for hovering flight. With the assumption that non-ideal induced and profile losses can be accounted for with the inclusion of the term figure of merit, FM, then the resultant power loading can be written in terms of FM and disk loading DL:

$$PL = \frac{\sqrt{2\rho}FM}{\sqrt{DL}} \tag{3.20}$$

From Eq.3.20 and figure 3.11 it can be seen that hovering performance or maximum power loading, is obtained when the effective disk loading is minimized and the FM is maximized at any defined disk loading. Under the stated assumptions the best theoretical power loading is given by $FM = 1$, however in practice this is unachievable as non-ideal effects and profile power losses are inherent to hovering flight. It can be observed in figure 3.11 that the robotic samara have the highest power loading for a given disk loading when compared to conventional rotors, cyclorotors, experimental flapping wings, and even some biological flyers including the hummingbird.

The induced or ideal power required to hover is given by $P = Tv_h$ and therefore

the power loading PL is inversely proportional to the induced velocity at the disk:

$$v_h = v_i = \sqrt{\frac{T}{2\rho A}} = \sqrt{\frac{DL}{2\rho}} = \frac{P}{T} = PL^{-1} \tag{3.21}$$

The ideal power required to hover is:

$$P_{ideal} = \frac{T^{3/2}}{\sqrt{2\rho A}} \tag{3.22}$$

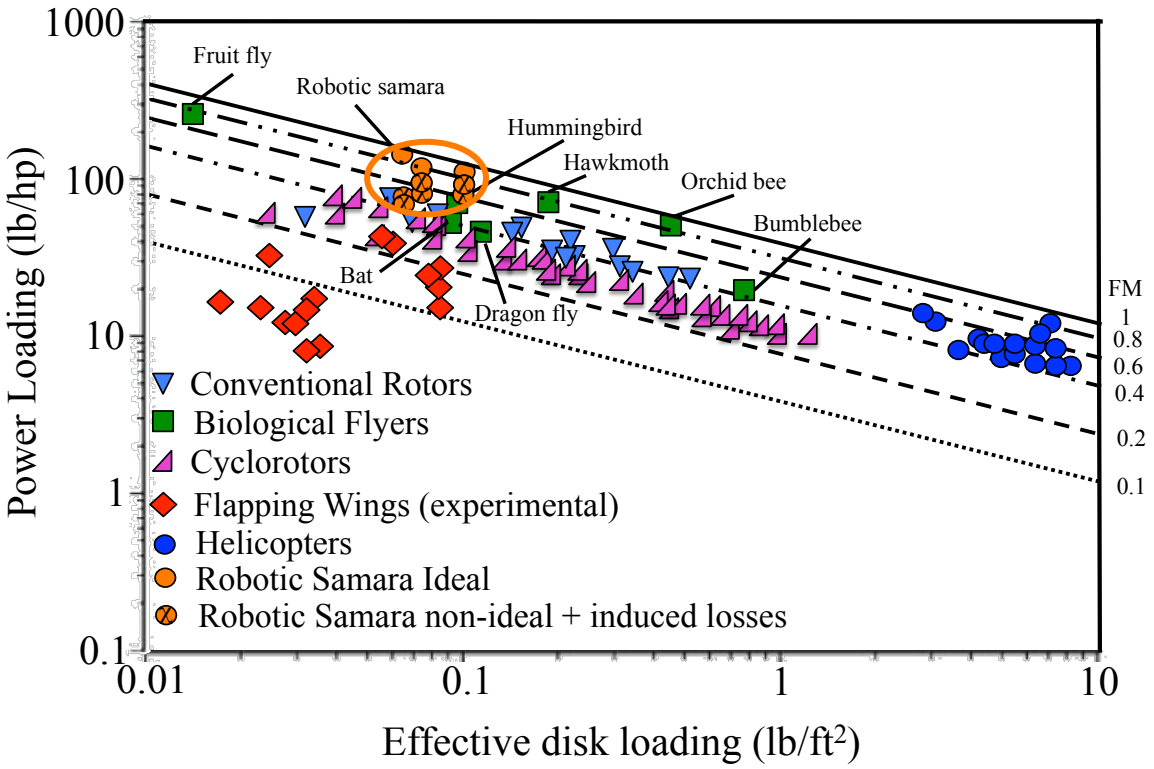

Figure 3.11: Hover efficiency of biomimetic and hover capable MAVs [33] [34] [35] [36] [37] [38].

3.4.1 Payload, mass fractions, and mass distribution

Pines, et al [2], found the propulsion system of small-scale fliers typically exceed 60% of the total vehicle mass, compared to a jetliner which boasts a propulsion system with a 40% mass fraction. The 20% savings at full scale is used entirely for payload as

the Boeing 767 payload mass fraction is 29%, compared to 9% for small-scale flight vehicles. The mass fraction of the propulsion system of samara I and II without payload is 47% and 42% respectively. If we consider the vehicles maximum gross takeoff weight for this calculation the mass fraction of the propulsion system drops to 28% and 35% respectively, with payload fractions of 40% and 21%, Table 3.3.

Table 3.2: Representative MAV Weight data (In terms of percent of GW).

Robotic samara [39]	I	II	III	Black Widow [40]	MICOR UMD [42] [43]	Boeing 767	Giant UT [44]	Hummingbird Aerovironment [45]
Gross Weight	GW	GW	GW	GW	GW	GW	GW	GW
Structure	20	25	26	18	12	35	28.9	14-21
Propulsion	28	33	52	64	70	39	55.2	49-86
Avionics	12	21	12	9	9	9	15.9	10-15
Payload	40	21	10	9	9	17	0	0

Table 3.3: Weight data (In terms of percent of GW).

Samara	I	II	III
Mass g	75	38	9.5
Max GTOW g	125	48	10.5
Max Dimension mm	270	180	75
%Gross Weight	GW	GW	GW
Propeller	2.6	5.3	4.2
Tailboom	3.3	2.6	3.0
Motor	10.7	10.5	30.5
Wing	27.6	26.3	24.4
Landing Gear	2.7	2.6	2.0
Control System	16.0	18.4	6.0
Avionics	7.9	4.0	6.6
Battery	33.3	26.3	23.2
Payload	0	0	0
Flight Time	20 min	10 min	2 min

3.4.2 Stability Properties

A substantial advantage of the samara-I and II vehicles is their a passive stability system. The type of motion exhibited by the robotic samara allows for stable unpow-

ered flight if the distribution of mass mimics a natural samara. The exact inertial properties and their relation to stability are detailed in this section. A simple qualitative stability analysis of the samara-I in a steady hover or autorotation illustrates this point. In steady hover the thrust from the propeller (F_P) is balanced by the drag from the body and wing (F_{D_W}), resulting in a near constant rotational rate about its principal inertial axis, I_z. The vertical force generated by the wing (F_{L_W}) apposes the force of gravity (F_G) resulting in a net zero vertical velocity. Alternatively, in autorotation, the resistive torque of the wing drag is equal to the driving torque of the lift, resulting in a net zero torque and vertical acceleration. Consider the assumed motion $r = r_0$ and $p, q << r_0$ in steady hover, or autorotation. To investigate whether the motion is stable, neglecting aerodynamic contributions, a small moment is applied to the body such that after the moment is applied the resultant angular velocities are as follows:

$$p = \epsilon_p \tag{3.23}$$

$$q = \epsilon_q \tag{3.24}$$

$$r = r_0 + \epsilon_r \tag{3.25}$$

Where ϵ_i $(i = 1, 2, 3)$ are infinitesimal quantities. To determine the evolution of these perturbed angular velocities in time it is convenient to use the Euler equations as follows:

$$I_z(\dot{r}_0 + \dot{\epsilon}_r) + (I_x - I_y)\epsilon_p\epsilon_q = 0 \tag{3.26}$$

$$I_x\dot{\epsilon}_p - (I_y - I_z)(r_0 + \epsilon_r)\epsilon_q = 0 \tag{3.27}$$

$$I_y\dot{\epsilon}_q - (I_z - I_x)(r_0 + \epsilon_r)\epsilon_p = 0 \tag{3.28}$$

The change in angular velocities is small, and as such allows linearization of the above equations by eliminating quadratic and higher order terms in ϵ_i yielding:

$$I_z\dot{\epsilon}_r = 0 \tag{3.29}$$

$$I_x\dot{\epsilon}_p - (I_y - I_z)r_0\epsilon_q = 0 \tag{3.30}$$

$$I_y\dot{\epsilon}_q - (I_z - I_x)r_0\epsilon_p = 0 \tag{3.31}$$

This implies ϵ_r is constant. The behavior of the remaining angular velocities can be understood with eigenvalue analysis. Assuming a solution of the form:

$$\epsilon_p(t) = E_p e^{\lambda t} \tag{3.32}$$

$$\epsilon_q(t) = E_q e^{\lambda t} \tag{3.33}$$

Next, we can introduce the expansions into the linearized equations:

$$\begin{bmatrix} I_x\lambda & (I_z - I_y)r_0 \\ (I_x - I_z)r_0 & I_y\lambda \end{bmatrix} \begin{bmatrix} E_p \\ E_q \end{bmatrix} e^{\lambda t} = \begin{bmatrix} 0 \\ 0 \end{bmatrix} \tag{3.34}$$

The solution requires that the determinant of the coefficient matrix be zero, yielding the characteristic equation:

$$I_x I_y \lambda^2 - (I_x - I_z)(I_z - I_y)r_0^2 = 0 \tag{3.35}$$

The solution is:

$$\lambda = \pm i\sqrt{\frac{(I_x - I_z)(I_z - I_y)r_0^2}{I_x I_y}} \tag{3.36}$$

Two types of solutions are possible and depend on the principal moments of inertia. If $I_x > I_z$ and $I_y > I_z$, or if $I_x < I_z$ and $I_y < I_z$ (characteristic of samara-I and

samara-II) both roots of the characteristic equation are imaginary. In the absence of nonconservative forces, the system is marginally stable [55]. The inertial parameters of the samara vehicles as well as the resultant eigenvalues are listed in Table 3.4.

Table 3.4: Inertia properties, rotation rate, and resultant eigenvalues for robotic samara-I and II.

	I_x	I_y	I_z	r_0	λ	
	$Kgmm^2$	$Kgmm^2$	$Kgmm^2$	rad/sec		
Samara-I	248	562	797	80.5	$\pm 0 + 77i$	rad/sec
Samara-II	35	98	122	76	$\pm 0 + 59i$	rad/sec

3.4.3 Wing Design

The aerodynamics of the robotic samara is subject to the scaling of Reynolds number *Re*, which is the ratio of inertial to viscous forces, and is a measure of the flow conditions over a body immersed in a fluid. The importance of this relationship as it applies to biological/bio-inspired systems can be understood through Nachtigall's [56] postulate of the subcategories into which biological creatures flow properties can be grouped.

Relevant to this work, the second regime is inhabited by insects and small birds that use vortices to stay aloft and move through a fluid. This regime is presently poorly understood, as compared to the third regime that is dominated by inertial effects, and is the environment in which MAV's reside. To achieve peak performance it is desirable to have the lifting surface of a wing operate at its maximum lift-to-drag ratio (L/D) as this is a measure of the wing's aerodynamic efficiency. The factors which determine L/D include wing geometry and surface roughness which influences the flow conditions over a given airfoil.

McMasters and Henderson [57] found the maximum L/D performance of various airfoils as a function of Reynolds numbers dramatically changed above Re=70,000 for smooth airfoils, whereas rough airfoils exhibited a steady increase with Reynolds

number and out-performed smooth airfoils below Re=10^5, Fig. 3.13^b. The variation of Reynolds number with span length for a robotic samara crosses this performance boundary at the out-board section of the wing, Fig. 3.13^b. It is therefore advantageous to distribute the the wing area such that the largest chord sections are collocated with the largest Reynolds number thereby increasing the maximum L/D for that wing section, Fig. 3.12^b. This approach is as well based on findings from the autorotation experiments which indicated that an increase in the distance of the area centroid Y_c from the center of rotation leads to an increase in the efficiency of the wing which is measured by the descent rate [30].

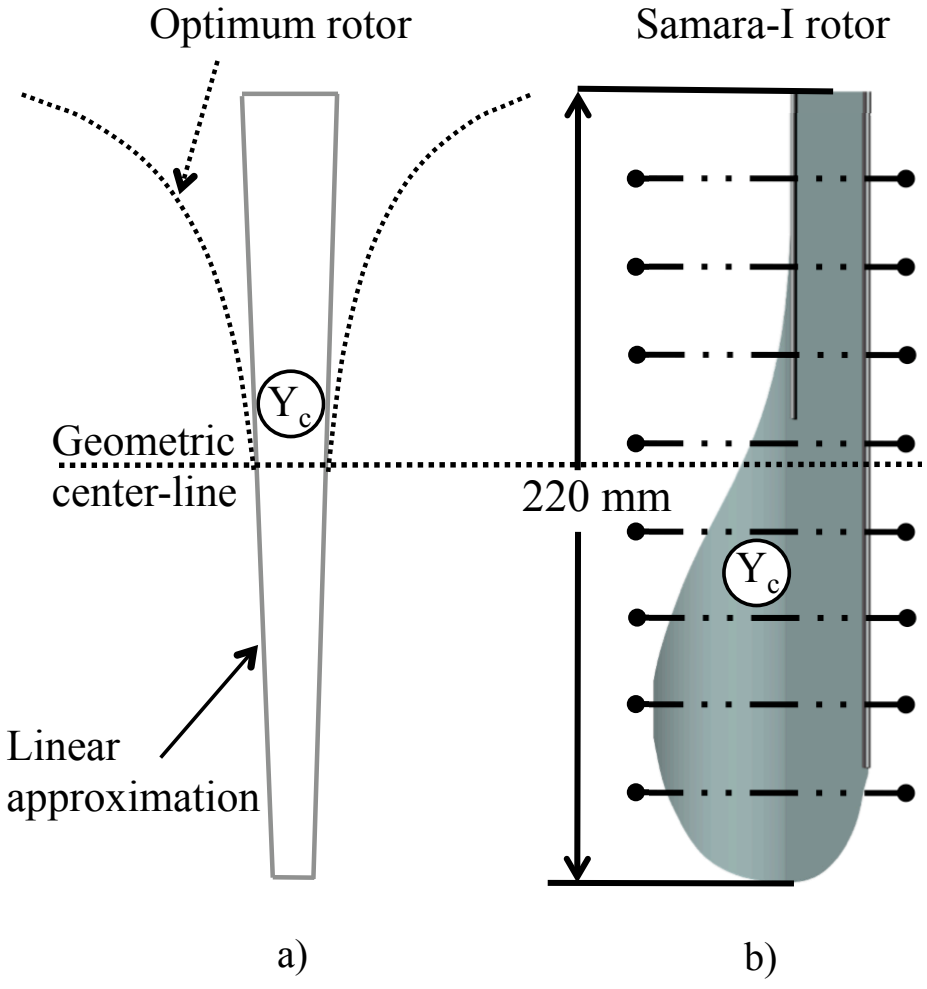

Figure 3.12: (a.) Optimum helicopter rotor design, [32]. (b.) Samara-I wing geometry. Y_c represents the span-wise location of the area centroid.

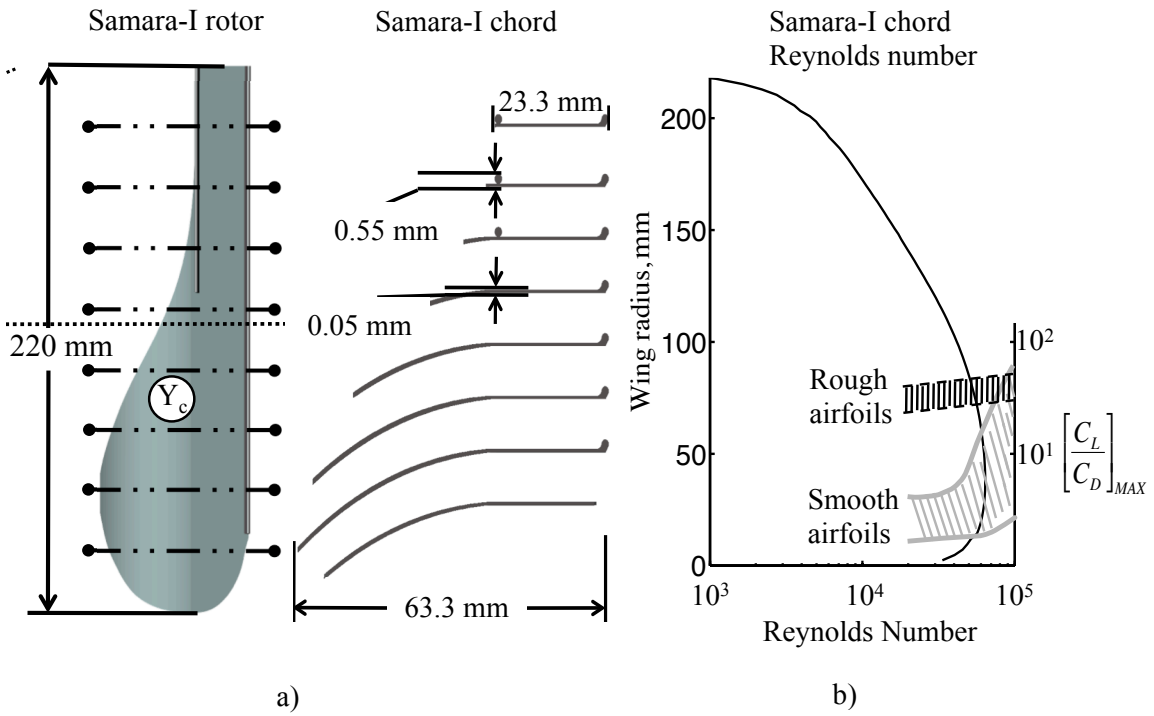

Figure 3.13: (a.) Samara-I wing chord distribution. (b.) Reynolds number variation with wing radius, [57]

This approach differs from full scale rotor design which seeks to minimize power loses by creating uniform inflow over the rotor disk [32]. This approach results in a rotor with large chord sections at a high angles of attack, close to the center of rotation, and small chord sections at lower angles of attack farther from the center of rotation, Fig. 3.12^a. The optimum rotor blade at full scale has a hyperbolic radial distribution of blade chord, however in practice a linear approximation is used and is beneficial to hovering rotor performance, Fig. 3.12^a.

3.4.4 Flight Test

Controlled flight of the robotic samara platform demonstrated the similarities between the unpowered/powered rigid body dynamics. The two modes of flight observed in unpowered flight are evident in powered flight, where the change in the radius of precession is used to dynamically steer the vehicle to a desired location. The two

test shown in Fig. 3.15 are for flight paths which carve out different size circles. The coning and feathering angle differ in magnitude and can be seen to result from the roll, pitch, and yaw body rates. The body angular rates for both turns are shown in Fig. 3.15^{b,e}, and the mean angular rates are shown in Fig. 3.15^{c,f}. Larger oscillations can be seen in β, θ for the path which carves out a larger circle, as was the case for the unpowered samara.

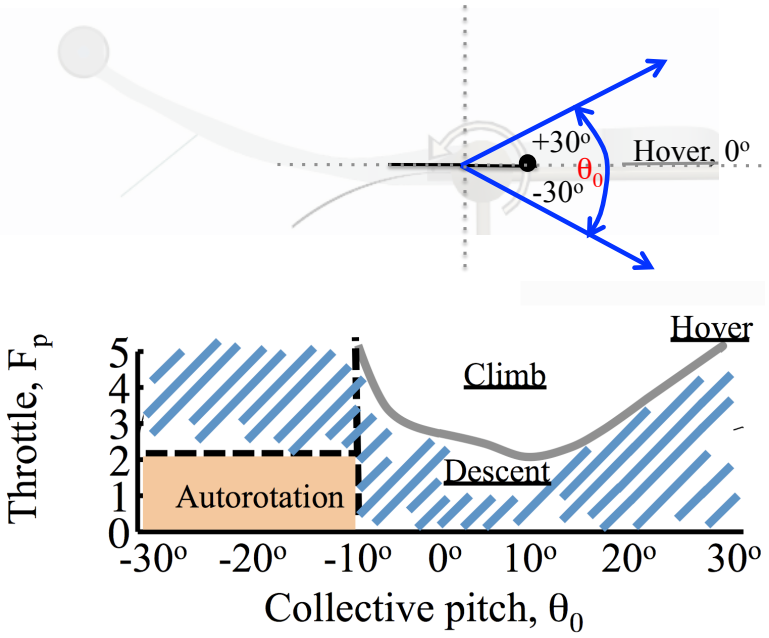

Figure 3.14: Flight envelope as is relates to throttle and wing pitch angle.

Control of the vehicle is done through open loop piloting, where the path of the signal from pilot to robotic samara is shown in Fig. 3.16^{a}. Lateral directional flight was recorded in the laboratory for a flight path consisting of an initial trim state and a perturbation about the trim, Fig. 3.16^{b}. In general, the turn radius is inversely proportional to the collective pitch of the wing. The samara travels in the opposite direction of the motion that would be induced by an impulsive collective input applied at that instant. A non-impulsive, sustained input changes the turn radius of the flight path such that an alternating series of large and small turn radii can steer the vehicle in a specific direction. The range of the samara-I vehicle is 4.8 Km which is computed

using its maximum translational velocity for 20 minutes of flight.

The velocity components, and rotation rate are shown in Fig. 3.16^b as they vary with the input θ_0. The first 0.5s of flight correspond to a near constant u and near zero w. At the time of the u-turn, 1-1.5s, there is an increase in the vertical velocity. The increase is correlated because a collective pitch increase used to change the heave velocity, is also used to change the flight path direction.

3.4.5 Scaling Effects

The flight dynamics observed in the passive and robotic samara have been found to exist in both larger and smaller prototypes ranging from 0.5 m to 0.075 m. The smallest and lightest robotic samara constructed to date is shown in Fig. 3.17, where the wing of the vehicle is similar in size to a natural samara wing.

3.5 Summary

This Chapter dealt with the design and scaling of robotic samara's. The unconventional wing and body structure of the robotic samara are the result of an iterative design process which has produced on the order of one-hundred configurations. Beginning with design constraints that maintain the inertial layout of natural samara, a number of fully controllable vehicle were created. The initial prototypes are presented in chronological order. This is followed by the general configuration and discussion of the final design iteration. The motor orientation, wing planform design, and connection between the two bodies is discussed and flight performance metrics are given for 3 different size vehicles. Finally the first at-scale robotic maple seed or samara is shown and discussed. The vehicles are extremely damage tolerant as they employ flexible structures which deflect upon impact. Advantages over traditional micro-scaled vertical take-off and landing (VTOL) configurations include passive stability,

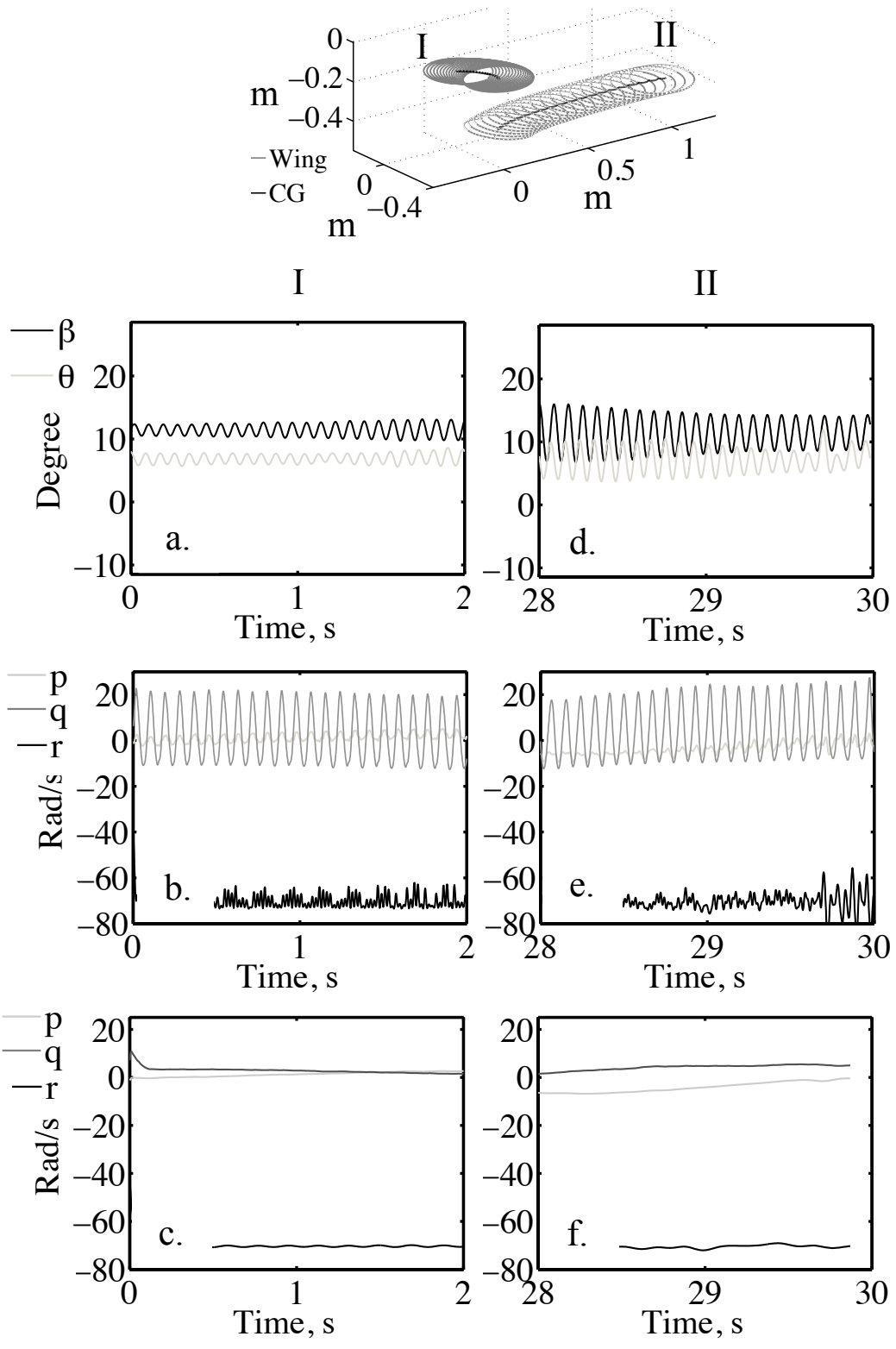

Figure 3.15: Flight test data for two different flight paths traversed by samara-I.

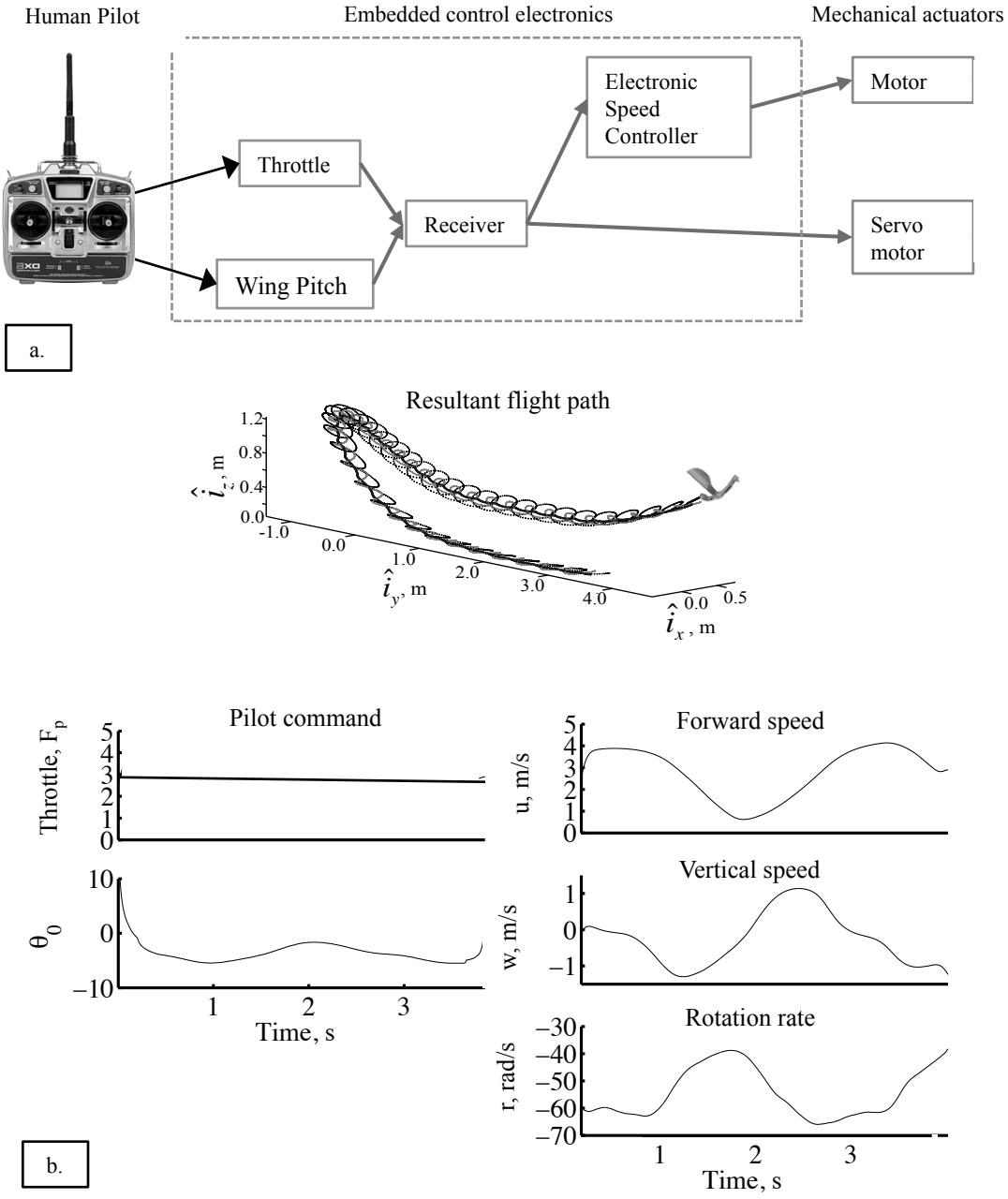

Figure 3.16: (a.) Samara-I control synthesis and signal diagram (b.) Samara-I coordinated U-turn maneuver with corresponding control input and resultant vehicle dynamics and flight path, [51].

efficient autorotation, low body drag, mechanical simplicity, low cost, high payload capacity, and substantial damage tolerance.

Figure 3.17: Smallest robotic samara constructed.

Chapter 4

System Identification, Stability and Control of Vertical Hovering Dynamics

4.1 Introduction

This chapter covers the experiments that led to the development of a mathematical model of the pitch and heave dynamics of two different size robotic samara prototypes. It begins with a description of a visual positioning system that was used to collect flight data while the vehicles were piloted in an indoor laboratory, and the way in which inputs to the vehicle are recorded by the system. The position data from the visual positioning system are converted to orientation and velocity. System identification techniques were used to create from flight data a linear model describing the pitch and heave dynamics. Next, eigenvalues of the heave dynamic model are estimated and the identified parameters are used in simulating the vehicles response to heave and collective input perturbations, as well as in the development of a PID controller. Finally, closed-loop implementation of the derived controller is

demonstrated using the visual tracking system for position and velocity feedback.

4.2 Experimental Setup

4.2.1 Visual Tracking System

Position and orientation of each vehicle was collected at a rate of 500 Hz using a Vicon visual tracking system. During a flight test, the tracking system utilizes eight cameras to track the three-dimensional position of three retro-reflective markers placed on the samara wing. Each marker is spherical with a diameter of 5 mm. The three dimensional shape of the marker allows for better tracking by the Vicon system. Figure 4.1 displays images of the virtual capture volume and the rigid body model of the samara wing created by the retro-reflective markers.

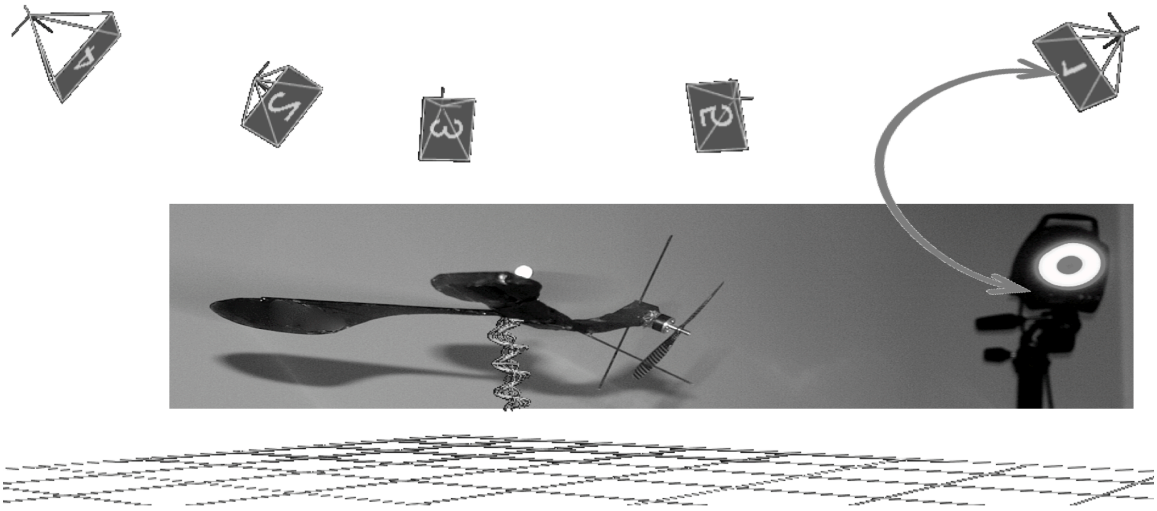

Figure 4.1: Representative Vicon workspace and flight path of samara-II.

4.2.2 Telemetry Synchronization

Pitch input is measured by two methods, both on and off the vehicle. The state of the actuator is measured off-board the samara on an identical system receiving

commands from the same transmitter. Two markers are placed on an arm attached to the off-board actuator to track the input to the vehicle. During a test flight the samara vehicle and the off-board actuator are simultaneously tracked allowing the angular displacement measured on the ground to be correlated to the motion of the samara vehicle; both of which are synchronized in time.

4.2.3 Vehicle Inputs

It is advantageous to track the wing pitch angle via the off-board system as it provides the ability to track the collective pitch inputs without the influence of the forces on the vehicle. The on-board method includes measuring both pitch angle, θ, and coning angle, β, via the markers placed on the wing. It is interesting to compare the on-board and off-board measurements as the on-board angles are influenced by the aerodynamic and centrifugal forces acting on the vehicle. The wing pitch angle, θ_0, of the vehicle in flight exhibits a once per revolution displacement. This variation results in a cyclical change in the coning angle, β, and heave velocity not captured by the off-board measurements. In the absence of aerodynamic forces the wing would assume an arbitrary orientation. However, in the presence of aerodynamic forces, a flapping moment is applied to the samara body causing the wing to precess to a new orientation, restoring equilibrium to the system. Nothing was assumed about the forces or deflection angles generated for a given change in the actuator, therefore all control inputs are normalized. The input command is given by θ_0 for collective input and is normalized such that $\theta_0 \in [-1, 1]$. The forces acting on the wing in flight as well as the definition of the coning angle are detailed in Fig. 4.2.

4.2.4 Attitude Determination

The 3D marker position data provide a means of resolving the orientation of the robotic samara in space. The three markers are sufficient to describe an orthonormal

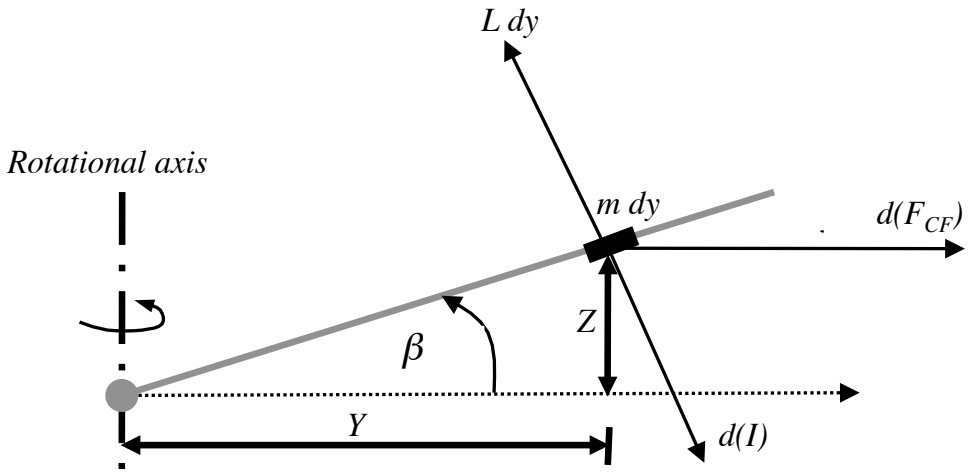

Figure 4.2: Forces acting on element of a flapping robotic samara wing.

basis from which the rotation matrix representing the samaras orientation can be formed. The first vector forms the $\hat{c}_j$-axis in body frame coordinates and is the line from the samara's center of mass (M_1) to the marker located in the positive $\hat{f}_y$-direction (M_2). The remaining basis require an intermediate vector from which to compute a cross product defining the $\hat{c}_k$-axis as follows:

$$\delta_{1,2} = M_1 - M_2 \tag{4.1}$$

$$\delta_{1,3} = M_1 - M_3 \tag{4.2}$$

$$v = \frac{\delta_{1,3}}{||\delta_{1,3}||}. \tag{4.3}$$

A schematic detailing the construction of the vectors is shown in Fig. 4.3. The intermediate vector $\delta_{1,2}$ can be normalized forming the $\hat{c}_i$ body frame axis. The vector v is formed by normalizing $\delta_{1,3}$. This vector is then used to compute the body frame $\hat{c}_k$ axis. The final body axis is formed in the cross product of $\hat{c}_k$ and $\hat{c}_i$. This set forms the orthonormal basis which defines the orientation of the body with respect to the inertial frame.

$$\hat{c}_i = \frac{\delta_{1,2}}{||\delta_{1,2}||} = \alpha_{11} + \alpha_{21} + \alpha_{31} \tag{4.4}$$

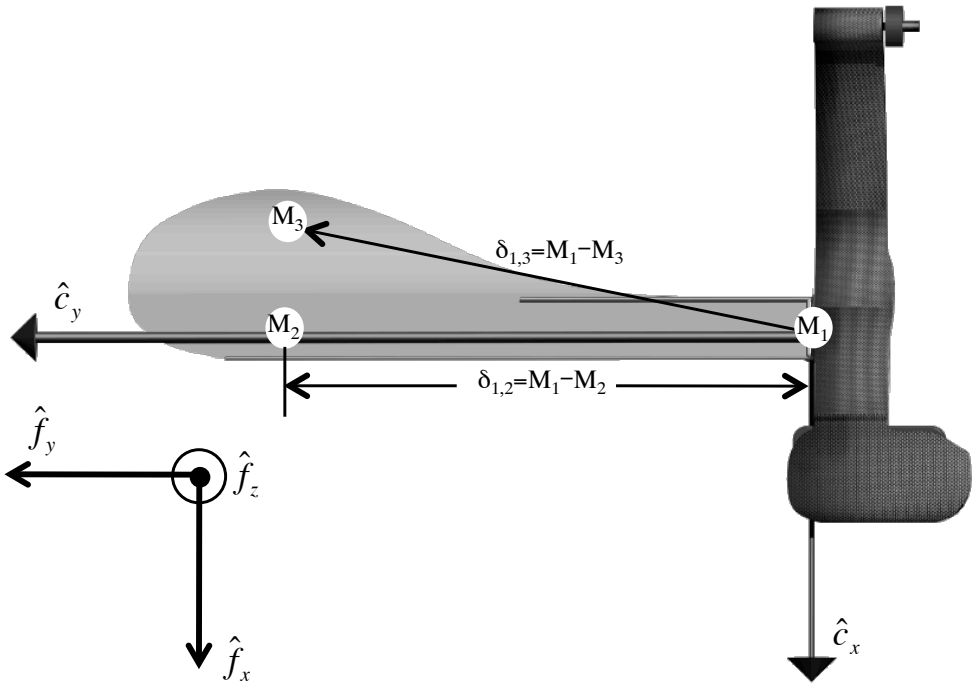

Figure 4.3: Retro-reflective marker placement.

$$\hat{c}_k = v \times \hat{c}_i = \alpha_{13} + \alpha_{23} + \alpha_{33} \tag{4.5}$$

$$\hat{c}_j = \hat{c}_k \times \hat{c}_i = \alpha_{12} + \alpha_{22} + \alpha_{32} \tag{4.6}$$

Once three-dimension marker position is obtained, and the basis set of the samara body axes are computed, the Euler angles can be deduced from the basis $[\hat{c}_i, \hat{c}_j, \hat{c}_k]$. The Euler angles provide a non-unique set of rotations which can describe the samaras orientation. The angles are computed as follows:

$$\theta = \arcsin -\alpha_{13} \tag{4.7}$$

$$\psi = \arctan \frac{\alpha_{11}}{\alpha_{12}} \tag{4.8}$$

$$\phi = \arctan \frac{\alpha_{23}}{\alpha_{33}}. \tag{4.9}$$

However, a singularity arises near $\pi/2$, and to maintain continuity of signs between successive time steps near the singularity it is necessary to set $\psi = 0$ and compute

the final angle ϕ as:

$$\phi = \arctan \frac{\alpha_{21}}{\alpha_{31}}. \tag{4.10}$$

A central difference scheme is used to calculate the Euler angular rates, $[\dot{\phi}, \dot{\theta}, \dot{\psi}]$.

4.2.5 Attitude Representation:

Attitude representation requires separate basis for the fixed inertial axes (**F**) and the body axes, which are fixed to the vehicle center of mass and are aligned with the principal inertial axis (**B**).

$$\mathbf{F} = [\hat{f}_x, \hat{f}_y, \hat{f}_z] \tag{4.11}$$

$$\mathbf{B} = [\hat{c}_i, \hat{c}_j, \hat{c}_k] \tag{4.12}$$

$$[\vec{r}]_B = R_1(\phi) \cdot R_2(\theta) \cdot R_3(\psi) \cdot [\vec{r}]_F. \tag{4.13}$$

The transformation from the inertial frame to that of the body frame is described by three Euler angles. The order of rotation is as follows: a yaw rotation ψ about the $\hat{f}_z$ axis, followed by a pitch rotation θ about the new $\hat{f}_y$ axis, and lastly a coning rotation ϕ, about the new $\hat{f}_x$ axis. The transformation matrix can then be written as:

$$R_{BF} = \begin{bmatrix} c\psi c\theta & s\psi c\theta & -s\theta \\ c\psi s\theta s\phi - s\psi c\phi & c\psi c\phi + s\psi s\theta s\phi & c\theta s\phi \\ s\psi s\phi + c\psi s\theta c\phi & s\psi s\theta c\phi - c\psi s\phi & c\theta c\phi \end{bmatrix}. \tag{4.14}$$

The notation is such that $s\theta = \sin\theta, c\theta = \cos\theta$. This rotation sequence is standard for aircraft [19]. The Euler angular rates are defined in the inertial coordinate system, Fig. 4.4. The angular rates in the inertial frame are finite rotations, which do not commute. It is thus necessary to define the body angular rates separately. The sum of the inner products of each of the inertial angular rates with the body axis of interest

yields the body angular rates:

$$p = -\dot{\psi}\sin\theta + \dot{\phi} \tag{4.15}$$

$$q = \dot{\psi}\cos\theta\sin\phi + \dot{\theta}\cos\phi \tag{4.16}$$

$$r = \dot{\psi}\cos\theta\cos\phi - \dot{\theta}\sin\phi. \tag{4.17}$$

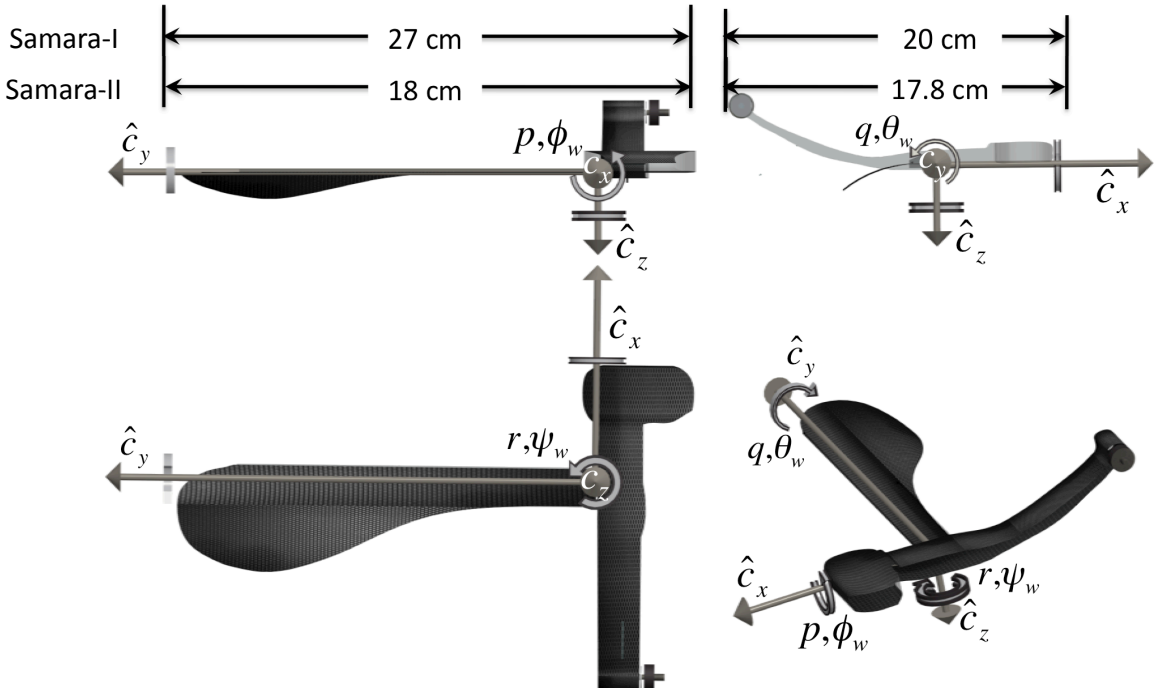

Figure 4.4: Robotic samara coordinate system, 3-view, and dimensions.

4.2.6 Kinematic Output

The Vicon data are exceptionally precise compared to data from commercial grade on-board attitude sensors. The position noise variance was estimated by recording data while not moving the vehicle, shown in Table 4.1. The low noise present in the position estimate allows the inertial position to be numerically differentiated to yield

inertial velocity estimates.

$$\{\dot{x}, \dot{y}, \dot{z}\}^T = \frac{\partial}{\partial t}\{x, y, z\}^T \tag{4.18}$$

The body fixed velocities can be directly computed using the direction cosine matrix representation of the orientation estimate, R_{BF}, and the inertial velocities as:

$$\{u, v, w\}^T = R_{BF}\{\dot{x}, \dot{y}, \dot{z}\}^T \tag{4.19}$$

Table 4.1: Measurement characteristics.

Measurement	Symbol	Source	Resolution	Variance	Unit
Time	t	VPS	$1.000 \times 10 - 3$	-	s
Control Input	θ_0	VPS	-	$7.8000 \times 10 - 3$	$norm$
Position	x, y, z	VPS	-	$0.613 \times 10 - 3$	m
Orientation	ϕ,θ,ψ	VPS	-	$7.800 \times 10 - 3$	rad
Translational Velocity	u, v, w	VPS	-	$0.251 \times 10 - 3$	m/s
Rotational Velocity	p, q, r	VPS	-	$1.200 \times 10 - 3$	rad/s

4.2.7 Open-Loop Flight Test Data

The first step in system identification is to pilot the vehicle in a flight envelope where the dynamics of interest are thoroughly excited. The vehicle was piloted within the capture volume of the vision system while simultaneously collecting the inputs and vehicle kinematics. The pilot excited the vehicle over a wide range of frequencies, which is required for determination of the relationship between input and output. For proper system identification, it is important to collect flight data open-loop, as a closed-loop feedback system would alter the natural dynamics of the vehicle. The open-loop setup is shown in Fig. 4.5.

Typical portions from recorded open-loop data sets are shown in Fig. 4.6. The

heave velocity, w, is found by applying the central difference approximation to the vehicle vertical position data collected by the Vicon system. Figure 4.6 also compares the inputs given to the vehicle during one flight test, as calculated both on and off the robotic samara. Both on-board and off-board methods demonstrate similar pitch inputs, but the on-board measurements display more oscillations.

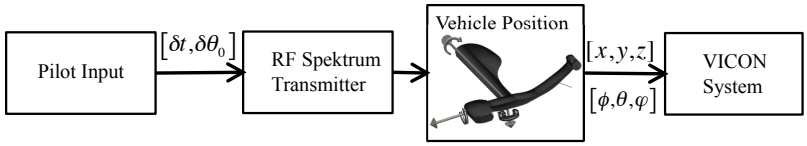

Figure 4.5: Open-loop control setup.

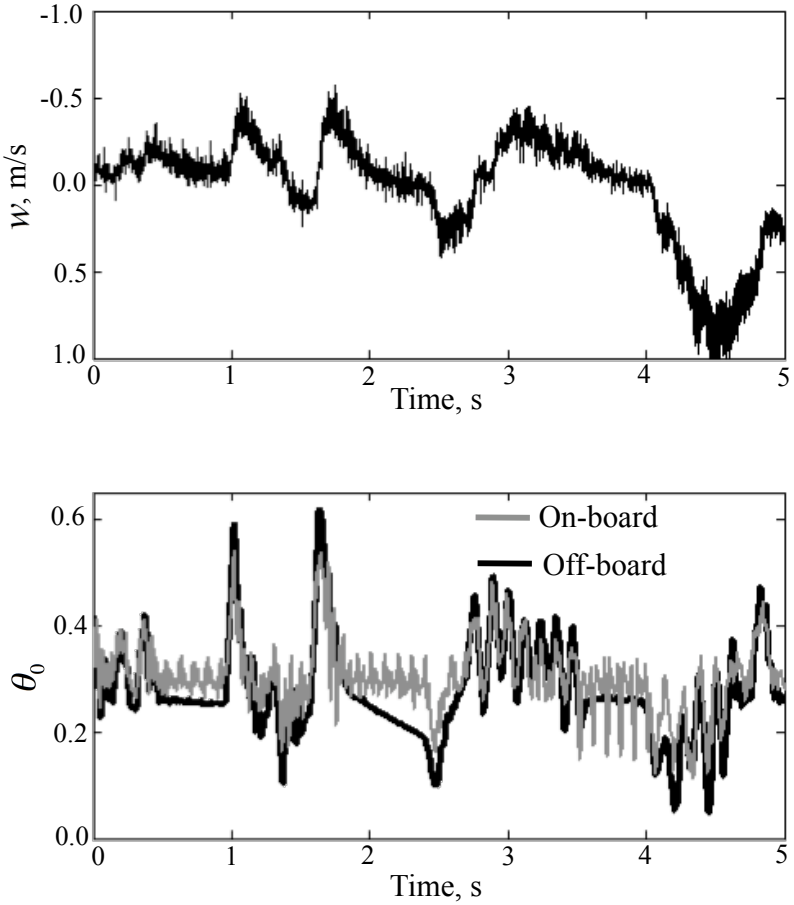

Figure 4.6: Flight data collected on samara-I.

4.2.8 Closed-Loop Flight Test Data

Implementation of closed-loop flight is enabled by an off-board feedback system. The ground control station setup is shown in Fig. 4.7. During closed-loop flight, the position and orientation of the robotic samara are tracked by the Vicon visual system, which sends the information to a LabVIEW controller program. The LabVIEW program takes into account the vehicles vertical position and heave velocity to create wing collective commands which are sent through a PIC-18F8722 microcontroller. The PIC microcontroller in turn sends the commands to the vehicle through a Spektrum Transmitter.

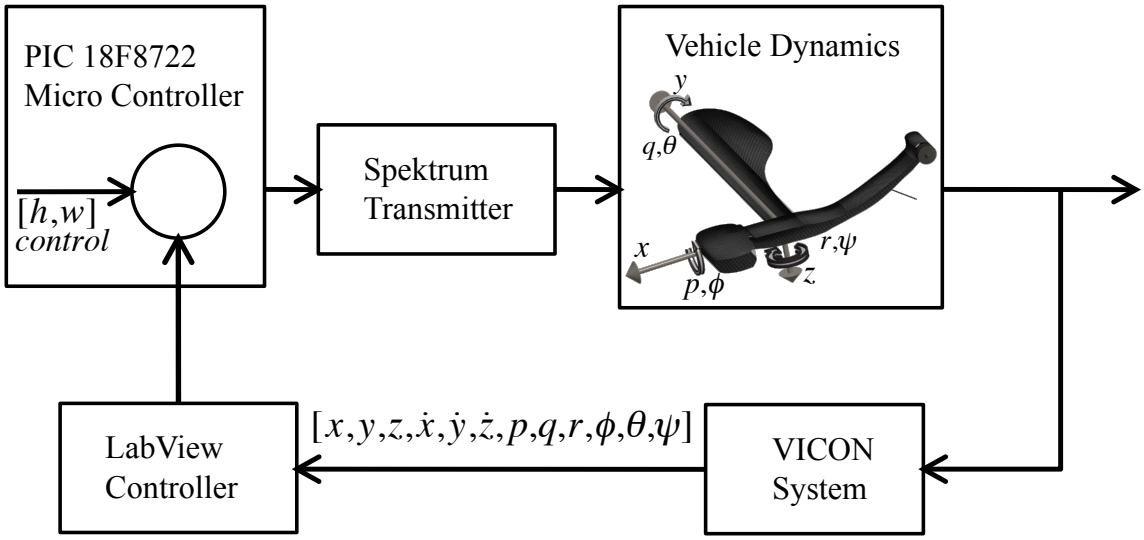

Figure 4.7: Ground control station (closed-loop).

4.3 Experimental Results

4.3.1 System Identification Method

A beneficial step in the identification process is computing the coherence function. This step provides a measure of the extent to which an output is linearly related to the input over some frequency range [53]. The magnitude squared coherence is given

by:

$$\gamma_{xy}^2(\omega) \equiv \frac{|R_{xy}(\omega)|^2}{|R_{xx}(\omega)||R_{yy}(\omega)|} \tag{4.20}$$

An input/output pair with low coherence implies either the input has no effect on the output or the effect is nonlinear. However, an input/output pair with high coherence implies the relationship can be modeled well by a linear model such as a transfer function or state space model. Tischler [53] suggests a coherence of 0.6 or above for some useful frequency range is necessary for accurate transfer function identification.

The magnitude squared coherence for the input/output relationship of samara-I using the on-board actuator system for input measurement is shown in Fig. 4.9. It can be seen that the useful frequency for this input/output pair lies in the range of 0.3 to 10 Hz. The coherence and useful frequency range predicted by the on-board measured θ_0 is equivalent to that of the off-board measurement, Fig. 4.9. The similarity of the two predictions validates the hypothesis that off-board measurements of θ_0 are capable of capturing the physics relevant for system identification. The on-board measurement of θ_0 for samara-II demonstrates some high frequency behavior above 55 rad/sec and may be a result of the aeroelasticity of the wing in flight, Fig. 4.9. Samara-I does exhibit lower correlation than samara-II below 5 Hz, most likely due to less excitation of samara-I in that frequency range as compared to samara-II. Despite the lower frequency content observed in the flight test of samara-I, all three coherence plots demonstrate similar ranges for strong relationships between input, θ_0 and output w.

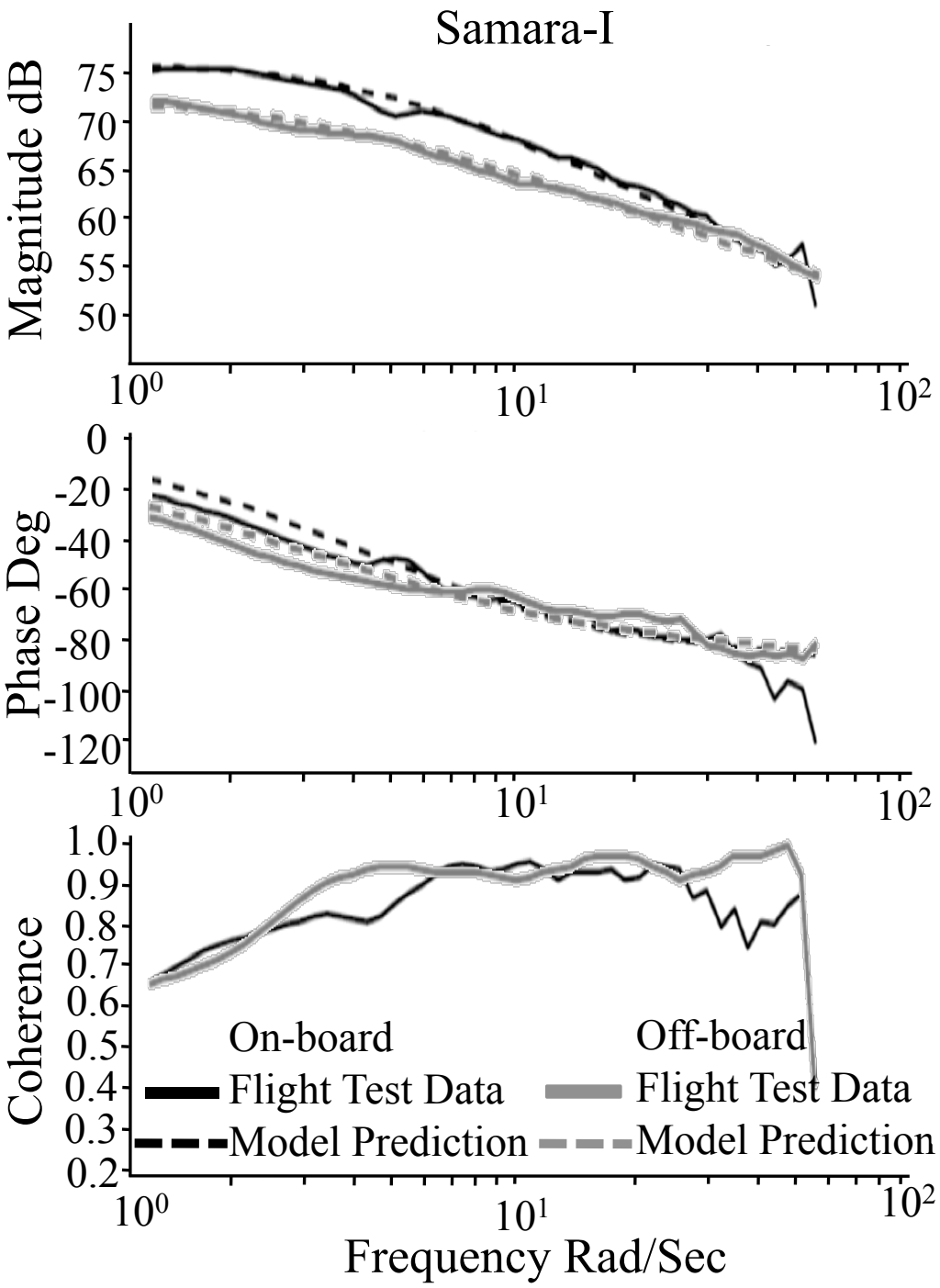

Figure 4.8: Robotic samara-I Identified model Bode diagram with corresponding data coherence, for on-board and off-board data collection and transfer function $G(s) = \frac{K}{s-T_{pl}}$.

4.3.2 Open-loop Control

The transfer function of the pitch input to heave dynamics was modeled as a first-order continuous-time process model:

$$G_p(s) = \frac{K}{s - T_{pl}} = \frac{W(s)}{\Theta(s)} \tag{4.21}$$

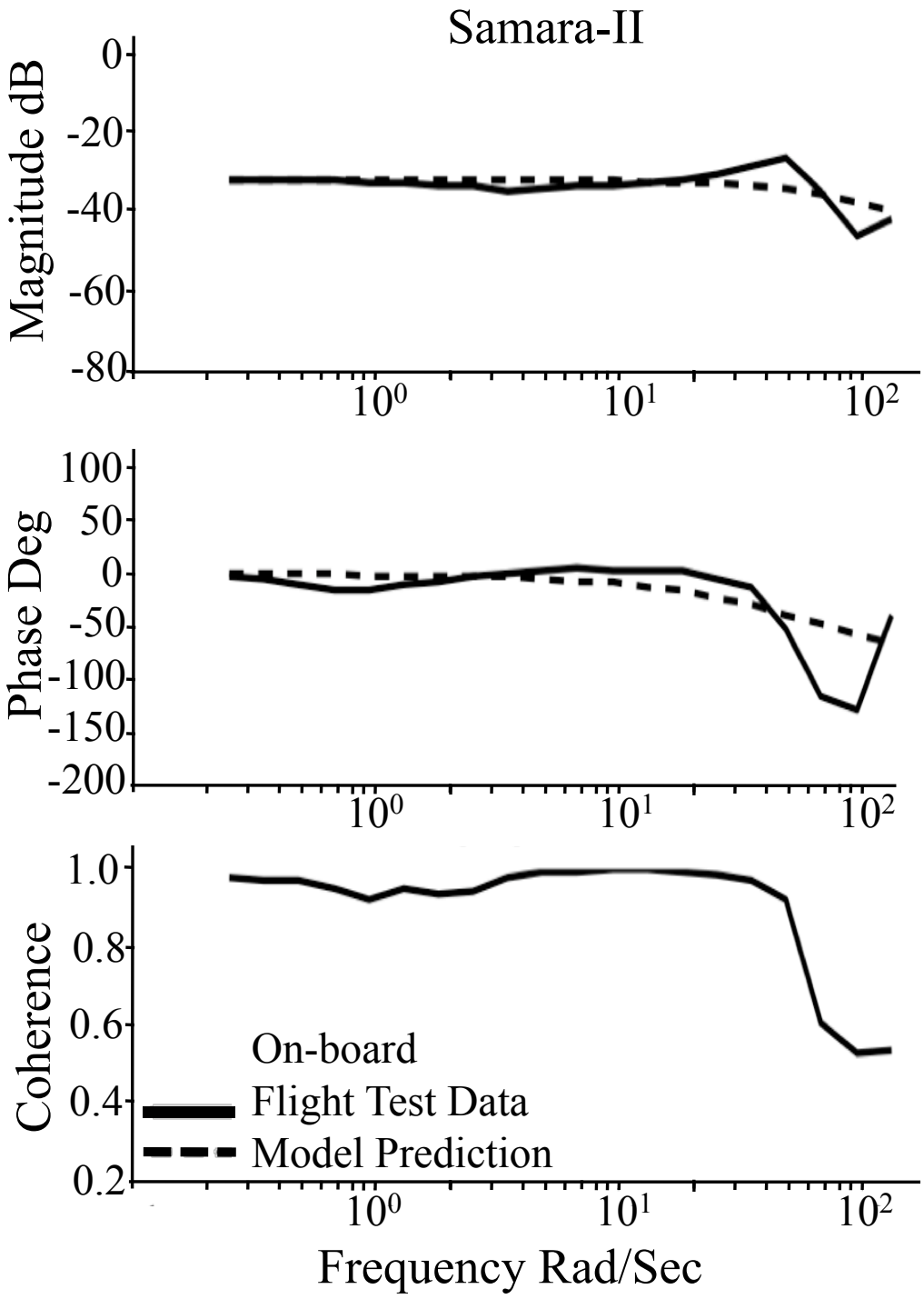

Figure 4.9: Robotic samara-II Identified model Bode diagram with corresponding data coherence, for on-board and off-board data collection and transfer function $G(s) = \frac{K}{s - T_{pl}}$.

Given a flight data set with sufficient coherence, as seen in Fig. 4.9, the MATLAB System Identification Toolbox can be used to compute frequency response-based system identification. The input and output data are imported to the system identification GUI where it is filtered to 100 rad/sec using a fifth-order Butterworth filter.

Table 4.2 shows the values identified for the robotic samara for the collective to heave velocity transfer function using data from both methods of measuring pitch input. In comparing the two methods of identification, it is important to note that both methods identify K and T_{pl} to be on the same order of magnitude, proving both methods have similar capabilities in capturing the input-output relationship. The transfer functions of the computed models are plotted in Fig. 4.9,4.11.

Table 4.2: Identified robotic samara parameters.

	samara-I	samara-I	samara-II
θ_0	Off-board	On-board	On-board
K	-13.643	-24.689	-21.44
T_{pl}	-4.864	-3.814	-1.690

4.3.3 Error analysis

A state space model was created allowing for error estimation using the Cramer-Rao bounds, and is represented as:

$$\dot{X} = AX + BU \tag{4.22}$$

$$Y = CX \tag{4.23}$$

The state space model for this identification reduces to

$$\dot{w} = Z_w w - Z_{\theta_0\theta_0}. \tag{4.24}$$

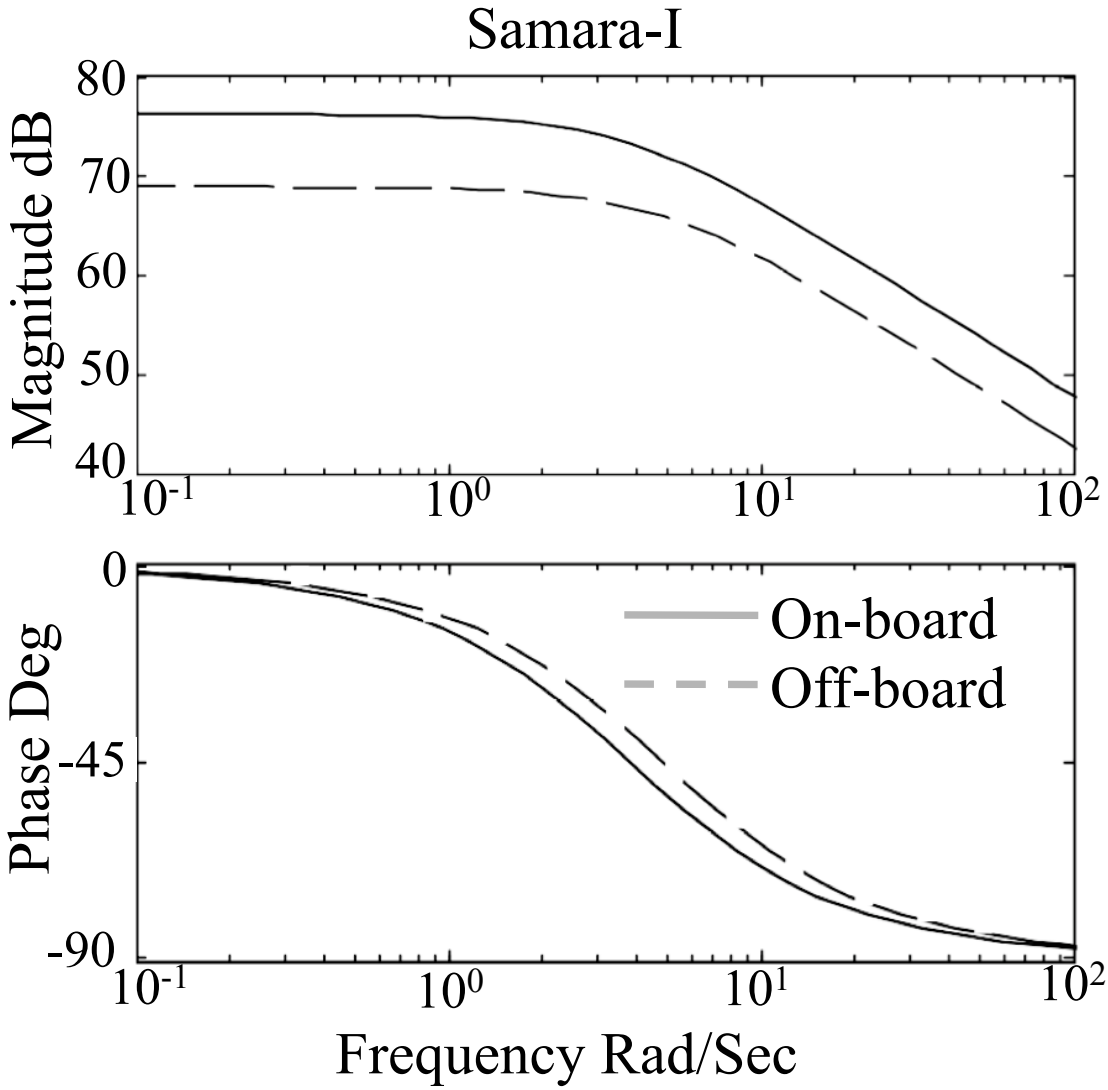

Figure 4.10: Robotic samara-I identified model Bode diagram, for on-board and off-board data collection and transfer function $\dot{w} = Z_w w - Z_{\theta_0\theta_0}$.

The Cramer-Rao bounds are theoretical minimum limits for the expected standard deviation in the parameter estimates, which would be obtained from several experiments [53]. Tischler suggests the following conditions represent the most valid parameter estimates: $CR\% \leq 20\%$, $\bar{I}\% \leq 10\%$. The CR and $\bar{I}$ percentages were found using the Comprehensive Identification of FRequency Responses software (CIFER). Table 4.3 shows the parameter estimates and associated error bounds of the identified state space model and demonstrates the validity of the identified parameter estimates,

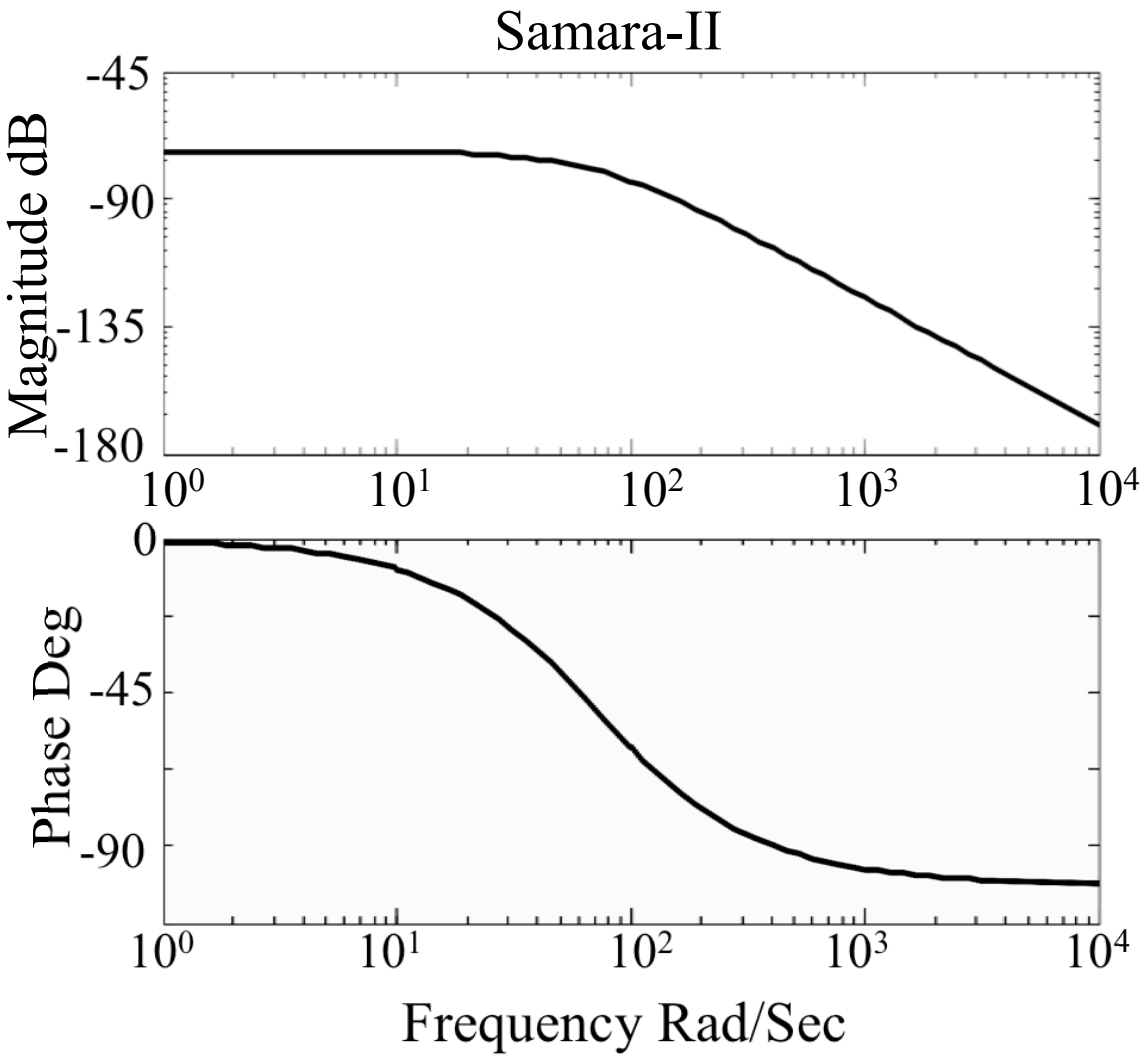

Figure 4.11: Robotic samara-II identified model Bode diagram, for on-board and off-board data collection and transfer function $\dot{w} = Z_w w - Z_{\theta_0\theta_0}$.

as all parameters meet the conditions specified.

The model computed from both on/off-board measurement of the collective angle input is capable of capturing most of the low frequency inputs, but can be seen to average higher frequency excitation. The model computed from the off-board measurement of collective angle input performs well at the lower frequencies but tends to average the higher frequency excitation. The model exhibits more overshoot than that of the model derived from on-board measurements. The small differences in the performance of the two methods of input measurement validate the ground-based

Table 4.3: Robotic samara identified parameter with Cramer-Rao error estimates.

	Term	Value	$CR\%$	$\bar{I}\%$
On-board samara-I	Z_w	-6.382	10.04	4.231
-	Z_{θ_0}	-15.880	4.733	1.994
Off-board samara-I	Z_w	-4.303	9.413	3.808
-	Z_{θ_0}	-28.130	5.022	2.032
On-board samara-II	Z_w	-20.640	13.670	2.064
-	Z_{θ_0}	-1.501	12.840	1.939

input observation method. A comparison of the poles identified by MATLAB and CIFER is displayed in Fig. 4.13. The control derivative is a negative number as an increase in collective pitch, θ_0, results in an increase in rotor thrust.

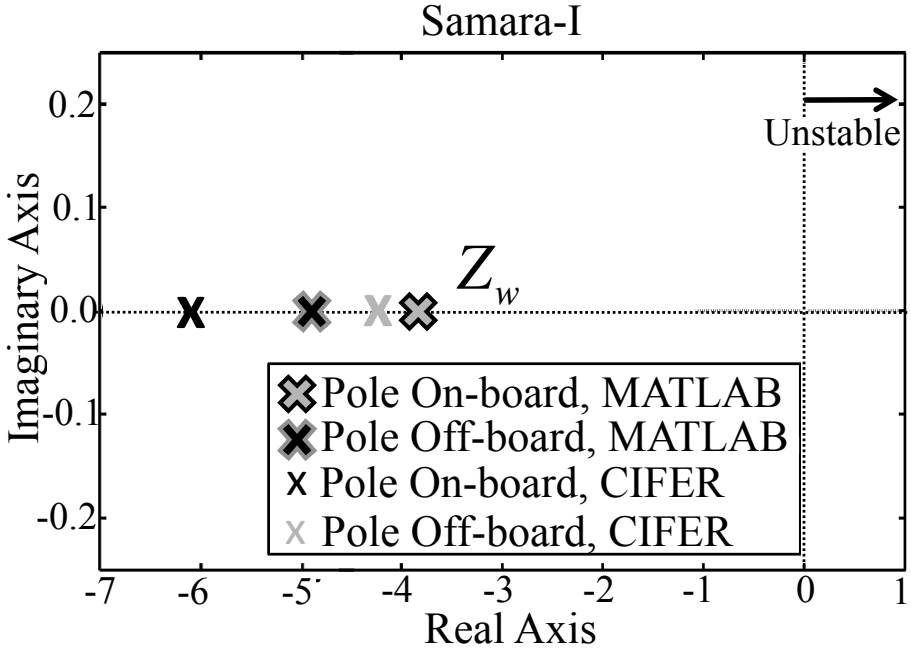

Figure 4.12: Real negative heave pole for Robotic samara-I.

4.3.4 Heave Dynamics

The heave dynamics of the robotic samara in hover are described by

$$\dot{w} - Z_w w = 0, \tag{4.25}$$

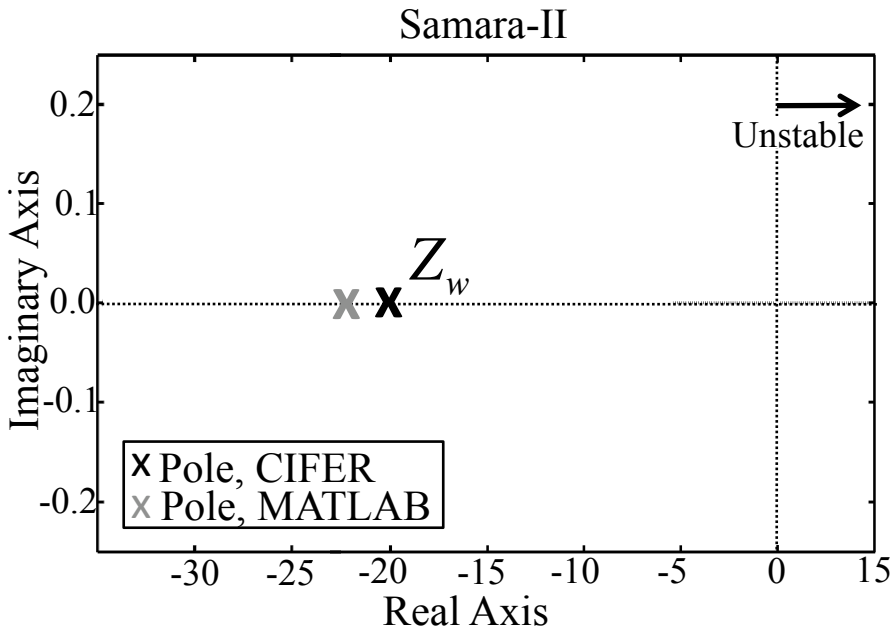

Figure 4.13: Real negative heave pole for Robotic samara-II.

where w is the heave velocity and $\dot{w}$ is the heave acceleration. This has the analytical solution of

$$w(t) = w_0 e^{Z_w t}. \tag{4.26}$$

Because the stability derivative Z_w is negative, the motion following a heave perturbation is a stable subsidence, shown in Fig. 4.14. For example, a positive heave perturbation will generate an upflow through the robotic samara rotor disk and increase thrust which acts in the negative direction of the $\hat{c}_z$-body axis. This also implies that in hover the robotic samara will have a real negative pole, as shown in Fig. 4.13. It is as well possible to obtain the expression for altitude loss due to a velocity perturbation w_0. For a robotic samara in hover $w = \dot{z}$ and

$$z(t) = \int_0^t w dt + z_0 = w_0 \int_0^t e^{Z_w t} dt + z_0 \tag{4.27}$$

where z_0 is the initial altitude. Integrating from $\{0, t\}$ yields

$$z(t) = z_0 - \frac{w_0}{Z_w}[1 - e^{Z_w t}]. \tag{4.28}$$

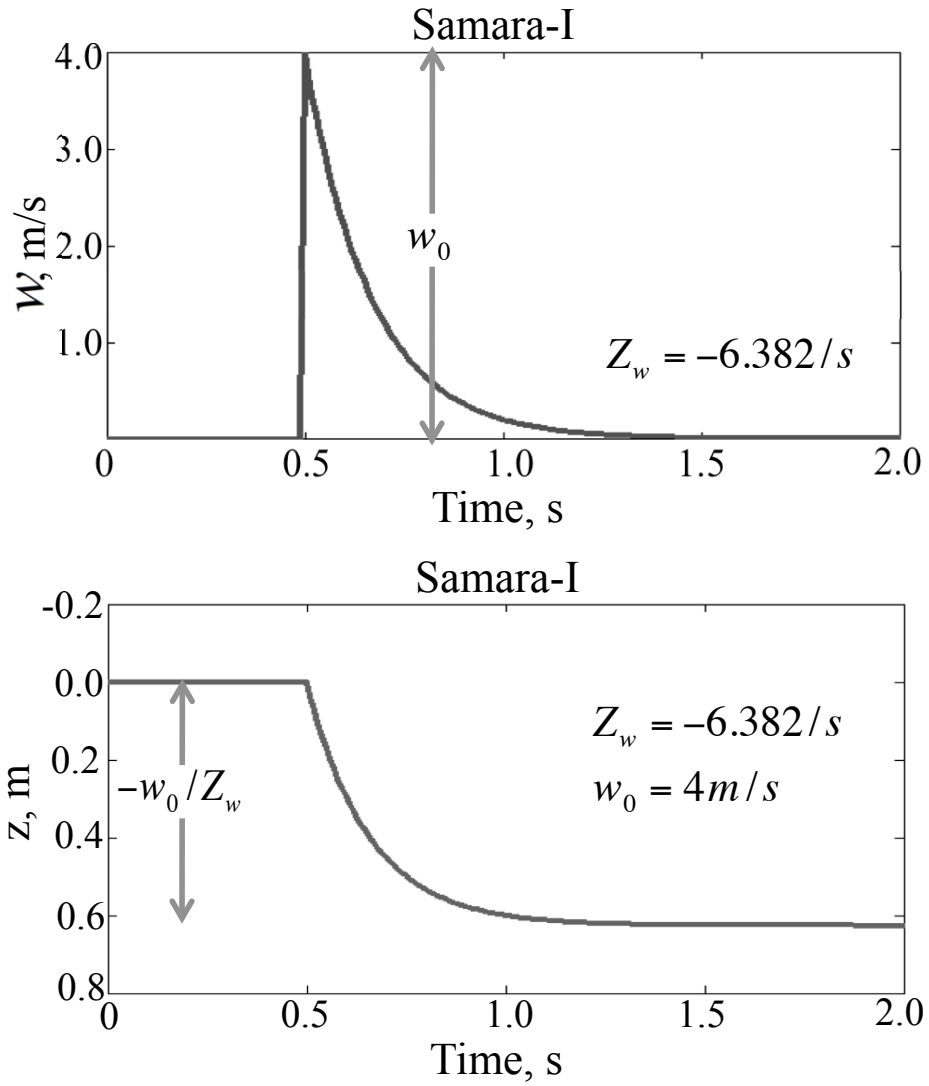

Figure 4.14: Motion following a perturbation w_0 of heave velocity.

Which the asymptotic value of altitude loss is

$$\lim_{t \to \infty} \Delta z = -\frac{w_0}{Z_w} \tag{4.29}$$

The robotic samara altitude change in response to a perturbation of heave velocity

is shown in Fig. 4.14.

4.3.5 Heave response to pilot input

Consider a step input of collective pitch $\theta_0 = 0.4$. After a change of variables the heave dynamic equation can be written as

$$\dot{w_1} - Z_w w_1 = 0 \tag{4.30}$$

where

$$w_1(t) = w(t) + \frac{Z_{\theta_0}}{Z_w}\theta_0, \dot{w_1} = \dot{w}. \tag{4.31}$$

The analytic solution of the first order differential equation is

$$w_1(t) = w_{1_0} e^{Z_w t}, \tag{4.32}$$

with $w_{1_0} = \{w + \frac{Z_{\theta_0}}{Z_w}\theta_0\}_{t=0^+}$. For the robotic samara in a steady hover $w = 0$, which reduces the solution of $w_1(t)$ to

$$w_1(t) = \frac{Z_{\theta_0}}{Z_w}\theta_0 e^{Z_w t}. \tag{4.33}$$

Thus the heave velocity response to a step input of collective pitch reduces to

$$w(t) = -\frac{Z_{\theta_0}}{Z_w}\theta_0(1 - e^{Z_w t}). \tag{4.34}$$

An example of the first order character of the vertical speed response to a step input of collective pitch is shown in Fig. 4.15. This is a basic characteristic of the behavior of a robotic samara and is clearly identifiable in results obtained from mathematical models and flight tests.

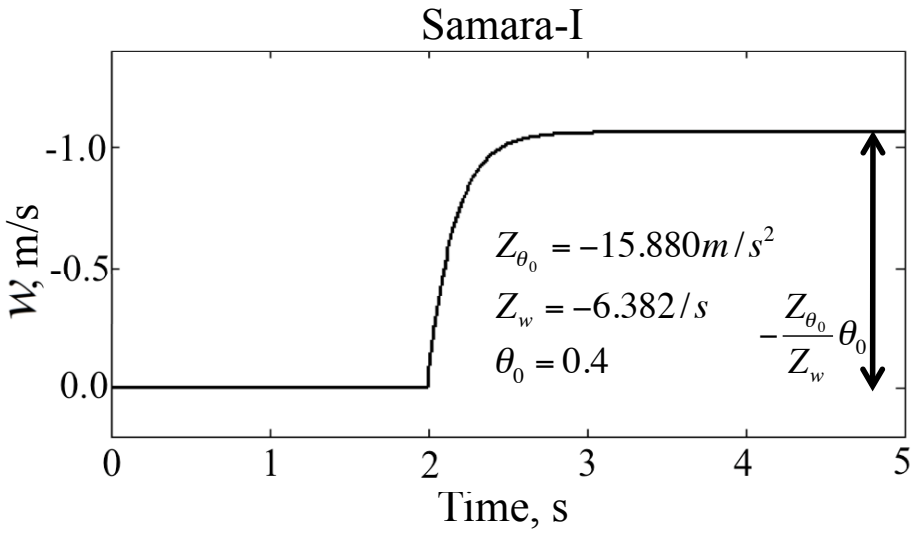

Figure 4.15: Robotic samara heave response to a step input of collective pitch.

4.3.6 Closed-loop Feedback Control

Feedback control is used to correct for perturbations in the system in order to keep the vehicle at a reference condition. The structure of the closed-loop system is depicted in Fig. 4.16. Precise attitude data are collected by the Vicon motion

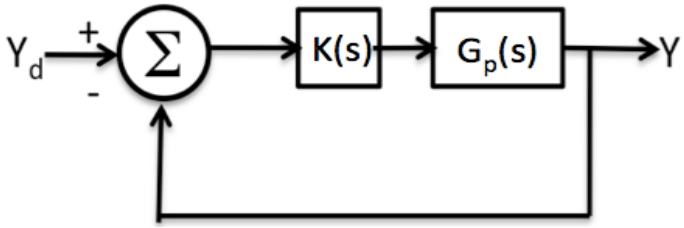

Figure 4.16: Prototypical feedback control loop.

capture system. The commanded altitude of the samara is maintained by feeding back the error in position to a control loop which contains the system and actuator dynamics. The closed-loop system attempts to compensate for errors between the actual and reference height of the samara by measuring the output response, feeding the measurement back, and comparing it to the reference value at the summing junction. If there is a difference between the output and the reference, the system drives the plant to correct for the error.

A proportional plus derivative plus integral (PID) controller was chosen for feedback control of the robotic samara. A PID controller is given by the equation:

$$K(s) = K_p + K_d s + \frac{K_i}{s} \tag{4.35}$$

A PID controller feeds the error plus the derivative of the error forward to the plant. The proportional gain provides the necessary stiffness to allow the vehicle to approach the reference height. The proportional gain improves steady state error but causes overshoot in the transient response, whereas the derivative gain improves transient response. The integral term is proportional to both the magnitude and duration of the error in position, with the effect of eliminating the steady-state error. Using the ground control station setup described in Fig. 4.7 for closed-loop feedback control, several gain combinations were tested in order to find the PID gains providing the best transient response to a change in reference height. Figure 4.18 depicts a representative data set of a flight test with the implementation of the PID controller using the gains in Table 4.4, demonstrating that the actual height closely matches the reference height.

Table 4.4: PID gains for feedback control.

Gain	samara-I	samara-II
K_p	0.211	0.344
K_d	0.889	0.133
K_i	0.028	0.020

The dashed line in Fig. 4.18 is the altitude specified by the ground station. The solid line is the vehicles vertical flight path. The change in altitude specified for ascent and descent are the same, and for a linear controller the initial change in collective input is as well the same. However, the resulting heave velocity in ascent is half the value observed in descent for both samara-I and samara-II.The characteristic over-damping in climb, and under-damping in descent, of samara-I and II is the effect of

gravity on the vehicle. In climb, the input wing force is greater than and opposite the force of gravity, and in descent the same input wing force is in the direction of the force of gravity resulting in a greater acceleration. The settling time Ts of samara-I for a climbing maneuver is 1.03 s with no overshoot. A descending maneuver settles to 90% of the final value within 1.45 s with an overshoot of 22%. The smaller samara-II reached 90% of its final value in 1.7 s with an overshoot of 60% for a descent maneuver. The settling time for a climbing maneuver is 0.7 s with a 4% overshoot. It can be seen that the forces induced on the body from a change in collective pitch are substantial compared to the inertia of the vehicle, as increases in heave velocity are quickly damped after excitation.

4.4 Summary

This work presented the identification of a linear model describing the heave dynamics of two robotic samara vehicles for use in future control and state estimation. A visual positioning system was used to collect flight data while the vehicles were piloted in an indoor laboratory. Eigenvalues of the heave dynamic model were estimated by two system identification packages. The identified parameters were used in simulating the vehicles response to heave and collective input perturbations as well as in the development of a PID controller. Closed-loop implementation of the derived controller was demonstrated utilizing the visual tracking system for position and velocity feedback. The characteristically under-damped response to a descent maneuver was found, which differs from the critically damped response to an ascent maneuver.

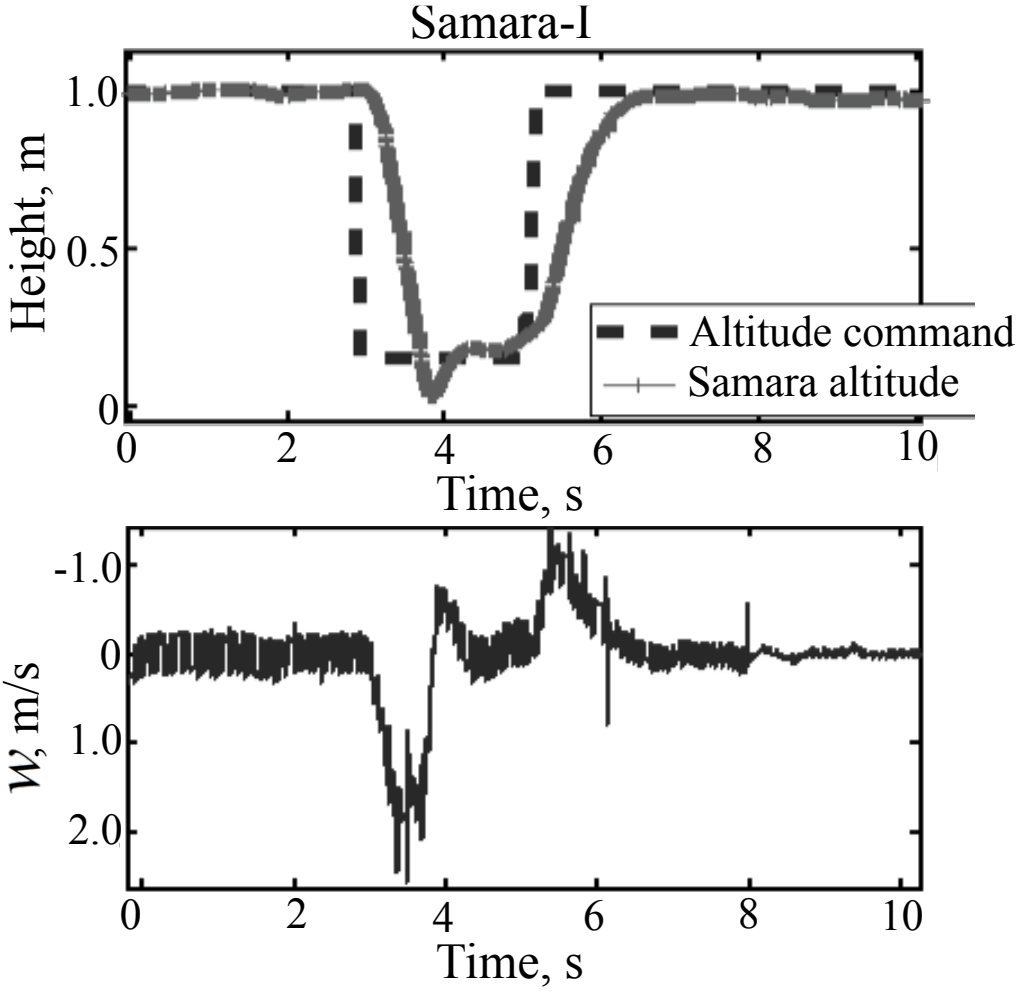

Figure 4.17: Implementation of PID control of Samara-I.

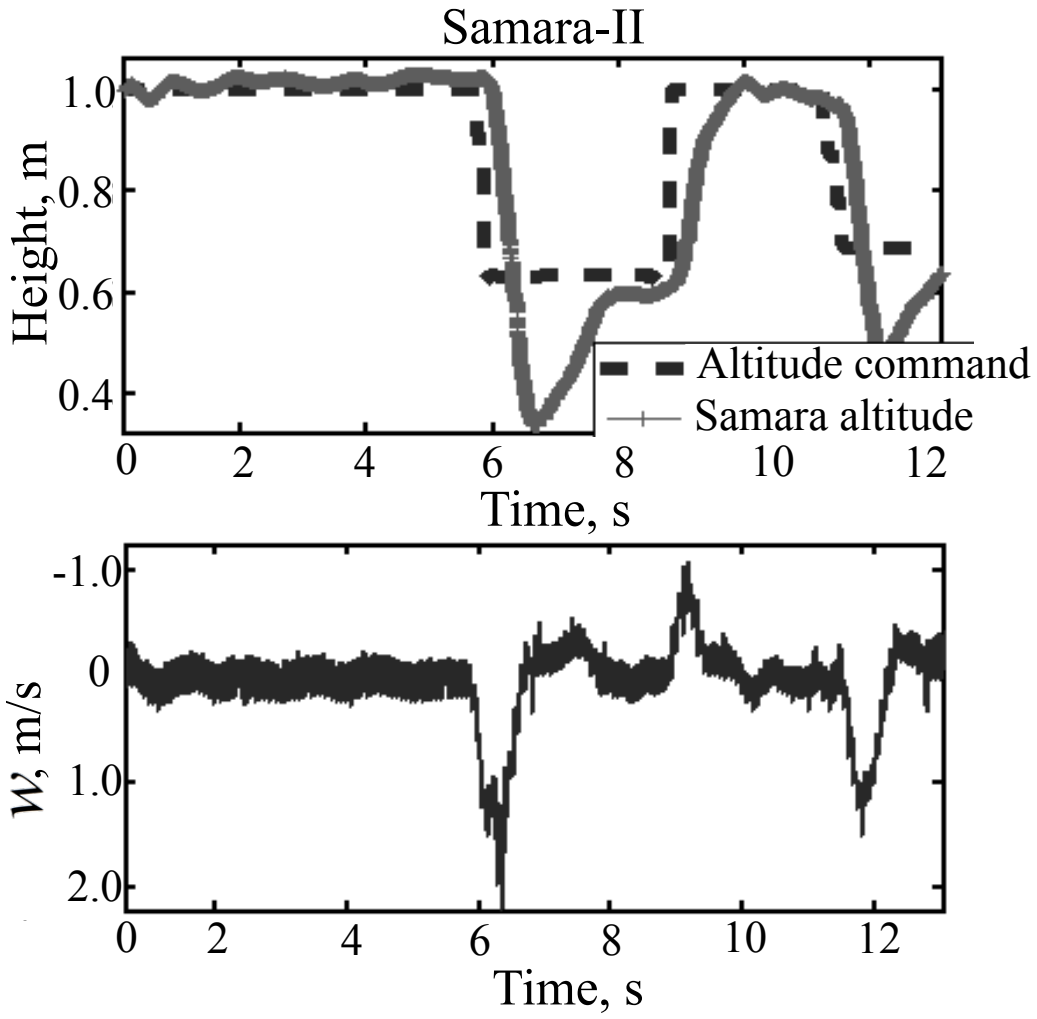

Figure 4.18: Implementation of PID control of Samara-II.

Chapter 5

System Identification, Stability and Control of Lateral Dynamics

5.1 Introduction

This chapter details the lateral flight dynamics and control of a prototype mono-wing rotorcraft that mimics the passive transit of the species of samara (winged seed), *Acer diabolicum Blume*. The chapter begins with a mathematical description of the general rigid body dynamics which are separated into rotor dynamics and particle navigation. These equations are then simplified for a coordinated helical turn flight path, which is then extended to forward flight. Next an experiment is discussed that uses a visual tracking system to record controlled flight for different flight paths. Finally system identification techniques are used to calculate stability derivatives for directional control which does not require the once per revolution flap actuation or high frequency measurement of vehicle orientation.

5.2 Lateral Flight Dynamics

5.2.1 Virtual body model

For the purposes of guidance, navigation, and control, a traditional MAV has a set of six to seven configuration variables corresponding to the 3D position of the center of gravity and the remaining three to four used to describe the orientation of the vehicle relative to an inertial reference frame. For the robotic samara, the body orientation evolves over time, ranging from a steady rotation rate about the $\hat{\imath}_z$ axis in hover to a more complex pitching, rolling, flapping and rotating motion in other flight conditions such as the translational flight condition addressed in the study.

To simplify the description, consider instead the "disk" described by the motion of the wingtip over each revolution, or "tip path plane" (TPP). As defined in traditional rotorcraft analysis, the TPP considered is one that discards the harmonic motion higher than 1/rev, allowing a plane to be defined from the surface. The aerodynamic lift force may be considered to act perpendicular to the TPP.

To describe the dynamics of the samara, consider a virtual (rigid) body connected to the disc center with an ideal hinge, with its center of gravity (CG) located directly below the disc center and with the mass of the samara, as seen in Figure 5.1. No aerodynamic moments may be transmitted across an ideal hinge, splitting the position/orientation dynamics into *rotor dynamics* describing the flapping motion of the blade, and *positional dynamics* of the samara to be described using the translational equations of motion for the motion of a point mass acted upon by the rotor disc forces.

The effect of rotating into a coordinate system where sideslip or v is zero can be seen in Figure 5.2.

The forward flight of the vehicle is most conveniently formulated in a non-rotating frame of reference attached to the virtual body. The orientation of the virtual body

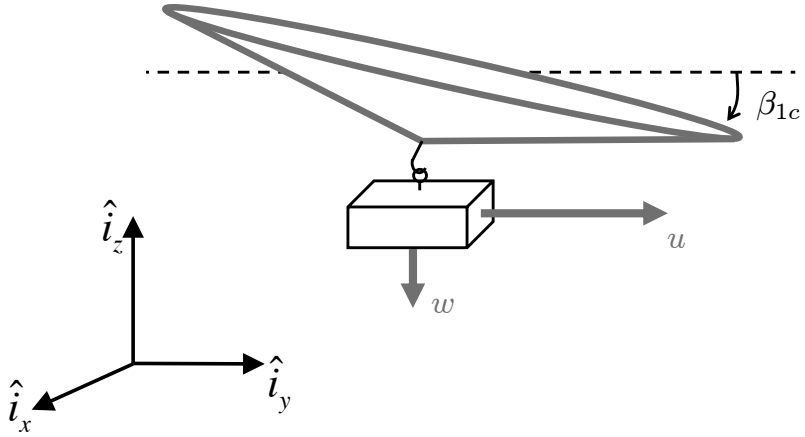

Figure 5.1: Modeling the samara as a rotor with a hinged virtual body.

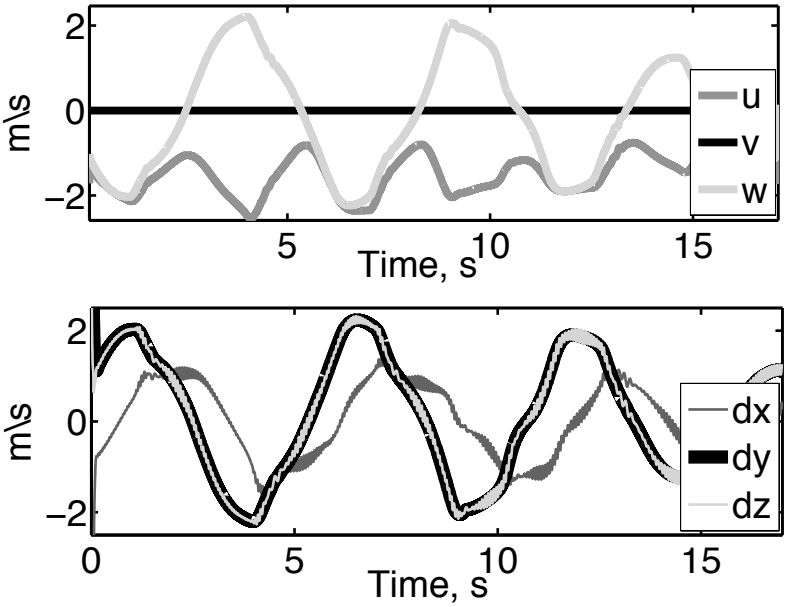

Figure 5.2: Virtual body velocity $[u, v, w]$, Inertial velocity $[\frac{\partial I_x}{\partial t}, \frac{\partial I_y}{\partial t}, \frac{\partial I_z}{\partial t}]$

forward velocity u is defined by the projection of the velocity vector onto the $[\hat{\imath}_x, \hat{\imath}_y]$ plane so that translation can only occur in the u direction and $v = 0$. The heave velocity is parallel to the inertial $\hat{\imath}_z$ axis and is shown in Figure 5.3. Also shown is the equal and opposite definitions of aerodynamic incidence α, and the flight path angle γ in relation to the virtual body velocities, u, w. The cyclic blade flapping is defined as the angle between the wing and the inertial plane $[\hat{\imath}_x, \hat{\imath}_y]$ and is shown in Figure 5.5.

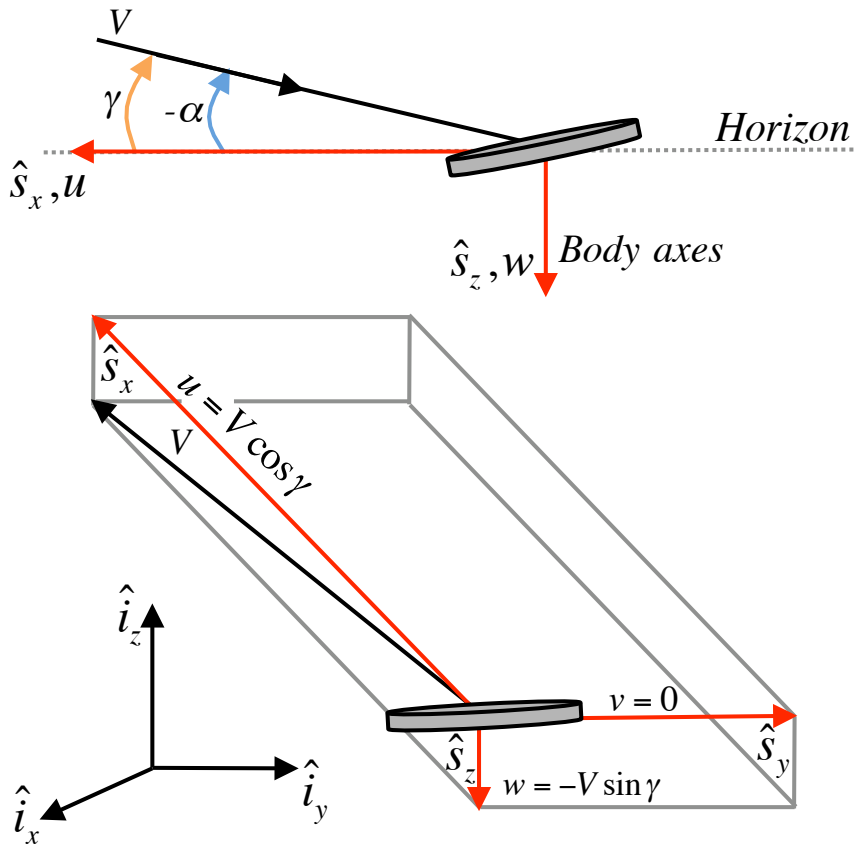

Figure 5.3: Definition of angle of attack and sideslip angle in relation to the velocity components.

$$[u, v, w]^T = [V\cos\gamma, 0, -V\sin\gamma]^T \tag{5.1}$$

5.2.2 Equations of motion for a flapping blade

In steady hovering flight the coning angle $\beta = \beta_0$ is constant and is independent of ψ. In forward flight the cyclically varying airloads induce an additional flapping response that varies about the azimuth ψ. The aerodynamic, centrifugal, and inertial forces acting on the robotic samara wing determine the observed coning angle, Figure 5.5.

We define a positive moment as one which acts to reduce the β. The centrifugal

force can then be written for an element along the span as

$$d(M_{CF}) = (m_w(y)dy)y^2\Omega^2\beta = m_w(y)y^2\Omega^2\beta dy \tag{5.2}$$

and the inertial moment about the flap hinge as

$$d(I) = (m_w(y)dy)y^2\ddot{\beta} = m_w(y)y^2\ddot{\beta}dy. \tag{5.3}$$

Additionally the aerodynamic moment is

$$d(M_\beta) = -L(y)ydy. \tag{5.4}$$

The aerodynamic force on a blade element with chord c, and distance y from the rotational axis can be calculated using blade element theory under the assumption of uniform inflow, [32]. With these considerations the aerodynamic moment about the flap hinge can be shown to be

$$\int_0^R Lydy = \frac{1}{8}\rho\Omega^2 cCl_\alpha R^4(\theta_0\frac{\dot{\beta}}{\Omega} - \frac{4\lambda_i}{3}). \tag{5.5}$$

The equation of motion can then be written as the sum of all the moments,

$$\int_0^R m_w(y)y^2\Omega^2\beta dy + \int_0^R m_w(y)y^2\ddot{\beta}dy + \int_0^R -Lydy. \tag{5.6}$$

The mass moment of inertia of the wing about the flap hinge is

$$I_b = \int_0^R m_w(y)y^2dy, \tag{5.7}$$

so that the equation of motion simplifies to

$$I_b\ddot{\beta} + I_b\Omega^2\beta = \int_0^R Lydy \tag{5.8}$$

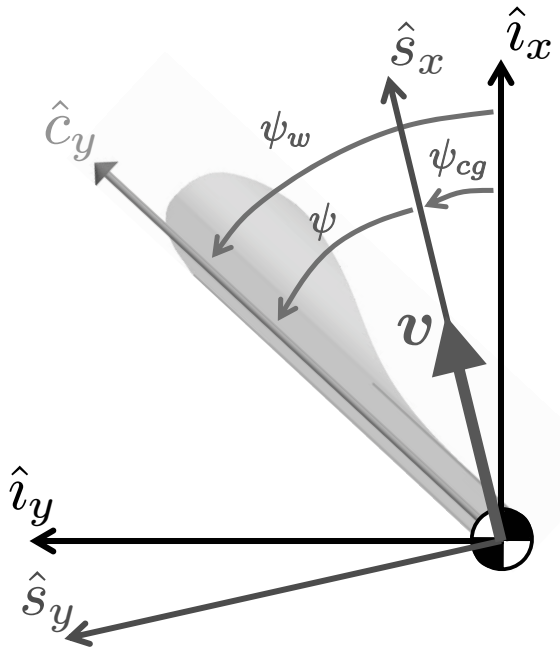

Figure 5.4: Definition of azimuth angles of the wing ψ_w, virtual body ψ_{cg}, and virtual body with respect to the wing ψ.

The sum of the applied moments form the differential equation describing the blade flapping motion. The flap equation can be written as a function of azimuth angle instead of time, where $\psi = \Omega t$ results in the following transformation; $\dot{\beta} = \Omega\overset{*}{\beta}$ and $\ddot{\beta} = \Omega^2\overset{**}{\beta}$. The equation of motion of the robotic samara flapping wing reduces to

$$\overset{**}{\beta} + \frac{\gamma_l}{8}\overset{*}{\beta} + \beta = \frac{\gamma_l}{8}[\theta - \frac{4}{3}\lambda_i] \tag{5.9}$$

where γ_l is the lock number of the robotic samara. The lock number is a function of the aerodynamic and geometric parameters listed in Table 5.1 and is computed as

$$\gamma_l = \frac{\rho\, Cl_\alpha c R^4}{I_b} = 6.75. \tag{5.10}$$

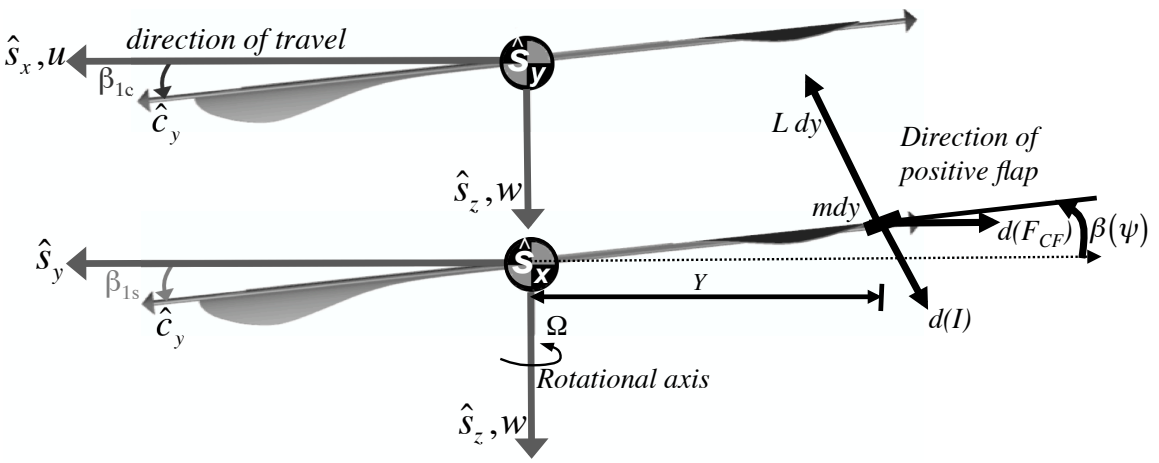

Figure 5.5: Definition of coning angles β_{1s}, β_{1c}. with forces acting on an element of a flapping robotic samara wing.

The coefficients can then be found to reduce to

$$\beta_0 = \gamma[\frac{\theta_0}{8}(1+\mu^2) - \frac{\lambda_i}{6}] \tag{5.11}$$

$$\beta_{1s} = \frac{-\frac{4}{3}\mu\beta_0}{1+\frac{1}{2}\mu^2} \tag{5.12}$$

$$\beta_{1c} = \frac{-\frac{8}{3}\mu[\theta_0 - \frac{3}{4}\lambda_i]}{1-\frac{1}{2}\mu^2} \tag{5.13}$$

Where $\mu = \frac{V}{\Omega R}$ is the advance ratio and θ_0 is the collective pitch angle [32]. Rearranging the solutions for β_{1c} and β_0 yields two expressions for the inflow λ_i as follows:

$$\lambda_i = \frac{2}{3}(1+\mu^2)\theta_0 - \frac{6}{\gamma}\beta_0 \tag{5.14}$$

which for the case of hover ($\mu = 0$) reduces to

$$\lambda_H = \frac{2}{3}\theta_0 - \frac{6}{\gamma}\beta_0. \tag{5.15}$$

For forward flight ($\mu > 0$)

$$\lambda_F = \frac{1}{2\mu}(1 - \frac{1}{2}\mu^2)\beta_{1c} \tag{5.16}$$

Thus given flight test data that corresponds to values of $\beta_{1c}, \mu, \theta_0$ and γ one can easily find values for the infow in both hover and forward flight.

The lift curve slope Cl_α was calculated from a combined blade element and momentum theory model of the robotic samara in hover. The kinematics of the model were based on flight test of the vehicle in hover, and the value of Cl_α presented adequately captures the hover performance of the robotic samara. However, in the analysis that follows the value of γ_l and Cl_α are not required and parameter estimates do not take these values into account.

Detailed numerical and steady state analytic solutions for the flap equation in (5.9) have demonstrated good agreement with a first order harmonic series [[32]]. Harmonic analysis of the flap equation allows a periodic solution of the form

$$\beta = \beta_0 + \beta_{1s}\sin(\psi) + \beta_{1c}\cos(\psi). \tag{5.17}$$

The blade flapping throughout the u-turn is observed to be periodic with respect to the azimuth angle ψ. The periodic coefficients describe the direction of force and can be seen to correlate with both the velocity and acceleration of the virtual body in Figure 5.6. The β_{1c} term influences the magnitude of u and the β_{1s} term influences the magnitude $\|\mathbf{V}_{cg}\|$.

The coefficients β_{1s}, β_{1c} are the out of plane flapping angles that describe the orientation of the wing within the disk. The orientation of the virtual body defines the roll and pitch angles to be $\phi = \beta_{1s}$ and $\theta = \beta_{1c}$ respectively. Thus the flapping of the wing in forward flight describes the instantaneous orientation of the virtual body which includes the coning angle β_0.

Table 5.1: Robotic samara wing properties

Measurement	Symbol	Value	Unit
Air density	ρ	1.225	Kg/m^3
Mean chord	c	3.5	cm
Wing length	R	18	cm
Lift curve slope	$C_{l\alpha}$	3.5	-
Wing inertia	I_b	23.3μ	Kgm^2

5.2.3 Rigid body equations of motion

The rigid body equations of motion are differential equations that describe the evolution of the state variables subject to applied forces. In body-fixed axes the sum of all external forces applied to the center of gravity is

$$m\dot{\mathbf{V}}_{cg} + mS(\boldsymbol{\omega})\mathbf{V}_{cg} = \mathbf{f} \tag{5.18}$$

where m is the vehicle mass, $\mathbf{V}_{cg} = u\hat{s}_x + v\hat{s}_y + w\hat{s}_z$ is the translational velocity of the center of gravity, $\boldsymbol{\omega} = p\hat{s}_x + q\hat{s}_y + r\hat{s}_x$ are the body-fixed roll, pitch and yaw rates, $\mathbf{f} = f_x\hat{s}_x + f_y\hat{s}_y + f_z\hat{s}_z$ are externally applied forces, and $S(.)$ is a skew operator.

The rotational dynamics are governed by the differential equation

$$\mathbf{I}\dot{\boldsymbol{\omega}} + S(\boldsymbol{\omega})\mathbf{I}\boldsymbol{\omega} = \boldsymbol{\tau} \tag{5.19}$$

where $\boldsymbol{\tau}$ is a vector of externally applied torques and $\mathbf{I}$ is a diagonal inertia matrix arising from symmetries in the virtual aircraft.

5.2.4 Coordinated helical turn

The flight path of the vehicle resembles a steady banked turn such that $\dot{\phi}_0$ and $\dot{\theta}_0$ are equal to zero. Additionally γ the flight path angle (> 0 for climbing flight) is

small so that $\sin\gamma = \gamma$ and $\cos\gamma = 1$. The kinematic equations are then

$$p = -\dot{\psi}_{cg} \sin\beta_{1c} \tag{5.20}$$

$$q = \dot{\psi}_{cg} \cos\beta_{1c} \sin\beta_{1s} \tag{5.21}$$

$$r = \dot{\psi}_{cg} \cos\beta_{1c} \cos\beta_{1s}. \tag{5.22}$$

Substituting the derived velocities and modified kinematics into the force equilibrium equations results in the following equations of motion:

$$X = mg \sin\beta_{1c} + m(\dot{u} + wq - vr) \tag{5.23}$$

$$Y = -mg \cos\beta_{1c} \sin\beta_{1s} + m(\dot{v} + ur - wp) \tag{5.24}$$

$$Z = -mg \cos\beta_{1c} \cos\beta_{1s} + m(\dot{w} + vp - uq) \tag{5.25}$$

where $[X, Y, Z]^T$ represent force equilibrium in the body fixed coordinate frame, and g is acceleration due to gravity.

Flight tests conducted with the robotic samara provide a means of verifying the equations of motion. A portion of a flight which fits within the constraints of the proposed analytical model is shown in Figure 5.6.

The variation of $\dot{\psi}_{cg}$ with the turn radius r_{turn} is observed to be linear for most of the trial, where a small but linear change in r_{turn} corresponds to a large change in turn rate $\dot{\psi}_{cg}$. The final portion of the figure shows the linear change in forward speed derivative $\dot{u}$ with respect to r_{turn}.

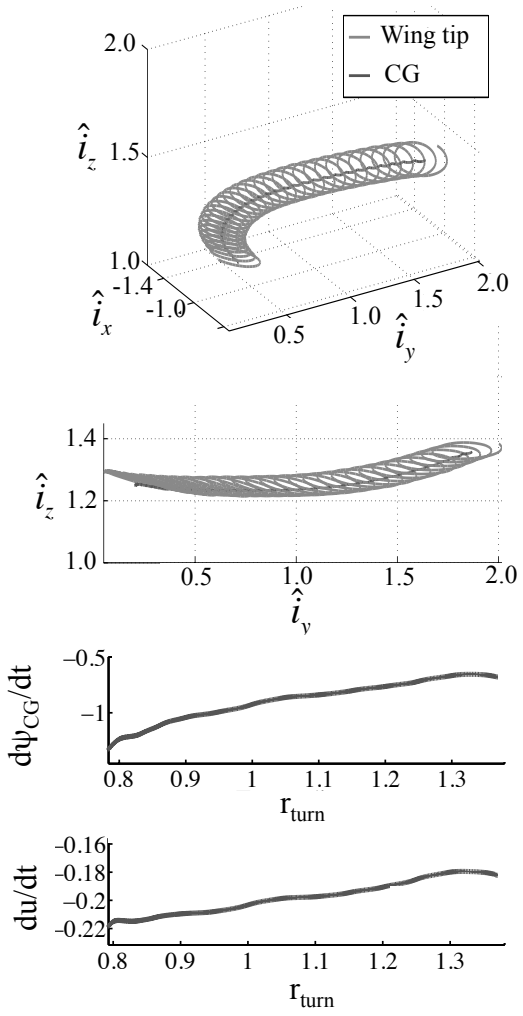

Figure 5.6: Flight data for a steady helical turn, including turn radius r_{turn}, turn rate $\dot{\psi}_{cg}$.

The flight path of the robotic samara is curved and the radius of the curve as it relates to the wing pitch angle and forward velocity is shown for an 18 second flight test. It can be seen that the peaks and valleys of the radius verses forward speed follow a similar trend; as the vehicle increases its speed the flight path radius becomes larger.

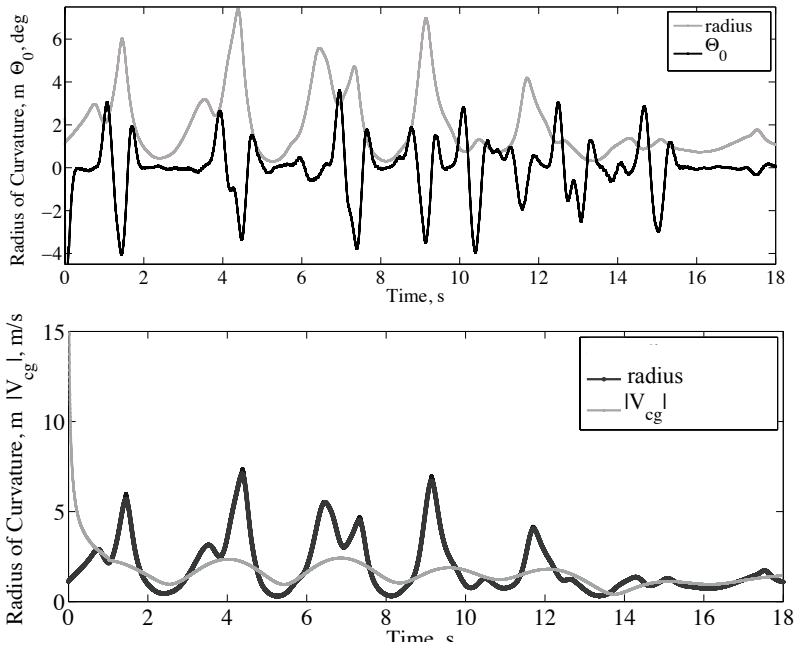

Figure 5.7: Turn radius r_{turn}, and forward velocity u.

5.2.5 Extension to forward flight

Pure longitudinal motion

Consider now straight flight as a special case of a coordinated turn, where $\dot{\psi} = p_0 = q_0 = r_0 = \beta_{1s} = 0$. The equation of motion along the $\hat{s}_x$-axis for forward flight may be written as the combination of a nominal condition (represented by $[]_0$) and a small perturbation $\Delta[]$ as:

$$X_0 + \Delta X - mg[\sin(\beta_{1c0}) + \Delta\beta_{1c}\cos(\beta_{1c0})] = \Delta\dot{u} \tag{5.26}$$

Setting all perturbation quantities to zero $\Delta[]$=0 yields the force equilibrium along trimmed forward flight:

$$\frac{X_0}{m} = g\sin\beta_{1c0} \tag{5.27}$$

Perturbation equations

The trimmed forward flight equation 5.27 can be subtracted from the linearized force equilibrium equation 5.26 leading to a description of small perturbation motion about the equilibrium condition as:

$$\Delta\dot{u} = \Delta X - mg\Delta\beta_{1c}\cos\beta_{1c} \tag{5.28}$$

Separating out the linear effects of the longitudinal variables $[u, w, \beta_0, \beta_{1c}]$ facilitates development of a canonical linear control model, and can be written as:

$$\frac{\Delta X}{m} = X_u\Delta u + X_w\Delta w + X_{\beta_0}\Delta\beta_0 + X_{\beta_{1c}}\Delta\beta_{1c} + \frac{X_c}{m}, \tag{5.29}$$

where $X_{[.]}=(1/m)\partial X/\partial[.]$, and

$$\frac{\Delta X_c}{m} = X_\theta\Delta\theta \tag{5.30}$$

The time-invariant linear system can now be expressed in state space form $\dot{\mathbf{x}} = \mathbf{Ax} + \mathbf{Bu}$ where $\mathbf{x} = [\Delta u, \Delta w, \Delta\beta_0, \Delta\beta_{1c}]^T$, and $\mathbf{u} = [\Delta\theta_0]$. Dropping the $[\Delta]$, the state space model is written in matrix form as:

$$\begin{bmatrix} \dot{u} \\ \dot{w} \\ \dot{\Omega} \\ \dot{\beta}_0 \\ \dot{\beta}_{1c} \end{bmatrix} = \begin{bmatrix} X_u & X_w & 0 & 0 & 0 \\ 0 & 0 & Z_\Omega & Z_{\beta_0} & 0 \\ 0 & 0 & \Omega_\Omega & \Omega_{\beta_0} & 0 \\ 0 & 0 & \beta_{0\Omega} & 0 & 0 \\ \beta_{1c_u} & 0 & \beta_{1c\Omega} & \beta_{1c\beta_0} & 0 \end{bmatrix} \begin{bmatrix} u \\ w \\ \Omega \\ \beta_0 \\ \beta_{1c} \end{bmatrix} + \begin{bmatrix} X_{\theta_0} \\ Z_{\theta_0} \\ 0 \\ \beta_{0\theta_0} \\ 0 \end{bmatrix} \theta_0 \tag{5.31}$$

Table 5.2: Parameter estimates and standard errors

Parameter θ	Equation-Error $\hat{\theta} \pm s(\hat{\theta})$	Output-Error $\hat{\theta} \pm s(\hat{\theta})$
X_u	$+0.42 \pm 0.18$	$+0.90 \pm 0.34$
X_w	$+3.74 \pm 0.57$	$+1.61 \pm 0.44$
X_{θ_0}	-7.99 ± 21.1	$+114 \pm 25.8$
Z_Ω	$+0.25 \pm 0.02$	$+0.22 \pm 0.03$
Z_{β_0}	-57.3 ± 12.3	-17.7 ± 23.3
Z_{θ_0}	-14.7 ± 13.4	$+38.9 \pm 19.5$
Ω_Ω	-1.34 ± 0.21	-2.26 ± 0.59
Ω_{β_0}	$+1001 \pm 63.8$	$+1231 \pm 219$
$\beta_{0\Omega}$	-0.01 ± 0.001	-0.006 ± 0.001
$\beta_{0\theta_0}$	-1.89 ± 0.34	-2.35 ± 0.32
β_{1cu}	-0.59 ± 0.21	$+0.56 \pm 0.21$
$\beta_{1c\Omega}$	-0.11 ± 0.03	$+0.09 \pm 0.05$
$\beta_{1c\beta_0}$	$+24.3 \pm 7.74$	-22.5 ± 15.8

5.3 Experimental Results

Position and orientation of each vehicle was collected at a rate of 500 Hz using a visual tracking system. The open-loop control setup used to pilot the vehicle and record vehicle state information is discussed in Ref. [47]. During a flight test, the tracking system utilizes eight cameras to track the three-dimensional position of three retro-reflective markers placed on the samara wing. A model of the vehicle geometry and the exact locations of the markers are used for least-squares estimates of the position of the center of gravity as well as orientation. The open-loop control setup and measurement noise characteristics are detailed in Ref [47].

The position estimates are precise and position noise variance was estimated by recording data while not moving the vehicle. The precision of the position estimate allows the inertial position to be numerically differentiated, using a central difference scheme, to yield inertial velocity estimates.

Lateral directional flight was recorded in the laboratory for a flight path consisting of an initial trim state and a perturbation about the trim, Figure 5.8. In general, the turn radius is inversely proportional to the collective pitch of the wing. While an impulsive response input changes the heave velocity of the vehicle, a step input changes the turn radius of the flight path. The samara travels in the opposite direction of the motion that would be induced by an impulsive collective input applied at that instant. The finding that the step response spends part of its time going in the "wrong" direction is an indication of a nonminimum phase system, or a right half plane zero, and the vehicle's differing responses to impulsive and step inputs are combined to create a strategy that provides full controllability, where an alternating series of large and small turn radii can be used to steer the vehicle in a specific direction. While a right half plane zero is normally a performance limitation, in this case, the behavior that typically restricts performance has been used in the control strategy to enable a single input to control multiple degrees of freedom.

The velocity components, rotation rate, and blade flap angles are shown in Figure 5.8 as they vary with the input θ_0. The first 0.5s of flight correspond to a near constant u and near zero w. At the time of the u-turn, 1-1.5s, there is an increase in the vertical velocity. The increase is correlated because a collective pitch increase used to change the heave velocity, is also used to change the flight path direction.

The flight data shown in Figure 5.8 was used to perform system identification using algorithms implemented in a MATLAB toolbox called System IDentification Programs for AirCraft (SIDPAC), detailed in Reference [58]. Guided by analytical modeling, modified step-wise regression was used to determine the model structure

using the statistical significance of measured states, resulting in the system shown in Equation 5.31. This model structure was chosen to maximize the model fit using regressors with a significant partial-f ratio, while minimizing the parameter estimate error bounds. A two-step procedure using the equation-error method, followed by the output-error method, was used to estimate the stability derivatives in the model. The equation-error method performs a linear estimation at the acceleration level, which has a deterministic solution that is computationally cheap to compute. The output-error method, widely regarded as more accurate, performs a nonlinear estimation at the level at which measurements were taken. This method requires an iterative numerical solver, but intial guesses using an equation-error estimate typically converge quickly. Parameter estimates and standard errors, corrected for non-white colored residuals, are given in Table 5.2. Model fits to the perturbation data sets are shown in Figure 5.9 for the equation-error and output-error methods, where the measurements are plotted with a solid line and the model outputs are plotted with a dashed line.

The model structure and parameter estimates fit the data well in most cases. In the case of $d\beta_0/dt$ the model failed to capture the higher frequency content, which may be due to non-linear or multi-body effects not captured in the linearized model. The equation-error results had model fits of 0.94, 0.94, 0.91, 0.56, and 0.59 for matching $\dot{\mathbf{x}}$ measurements and fits of 0.85, 0.97, 0.92, 0.83 and 0.12 for matching $\mathbf{x}$ measurements. The equations describing the flap dynamics had low model fits for both methods. Several parameters were estimated consistently by the two methods, lying within two standard deviations of each other. However several estimates did not match well and had large error bounds. These inconsistencies are due to limited excitation present in the flight data and will be remedied in the future with flight tests better suited for system identification.

5.4 Summary

This Chapter presented the derivation of the equations of motion of a robotic samara designed and constructed at the University of Maryland, College Park. An approach to directional control which does not require the once per revolution actuation or high frequency measurement of vehicle orientation has been demonstrated for the first time. Lateral flight is attained through the vehicle's differing responses to impulsive and step inputs which are combined to create a control strategy. Nonlinear Euler equations were used to describe the rigid body dynamics of the vehicle in a steady turn and are then extended to forward flight and linearized about a trim state, resulting in five linearized small perturbation equations in state space form. Flight tests provided high accuracy position information that was reduced to wing flap angles and virtual body velocities that were used to specify a flight condition that fit within the limits of the derived model and allowed for an estimation of the vehicle stability derivatives. The dynamics of the robotic samara during a coordinated turn can be approximated by a linearized model. Future work will validate the model structure and give physical significance to model parameters.

Additionally, several linear relationships were shown to exist including $[r_{turn}, \dot{u}]$, and $[r_{turn}, \dot{\psi}]$. The steady turn discussed here has been observed in scaled versions of the robotic samara. Therefore the open-loop control demonstrated and analyzed is considered appropriate for similar vehicles of reduced size with limited sensing and actuation capabilities.

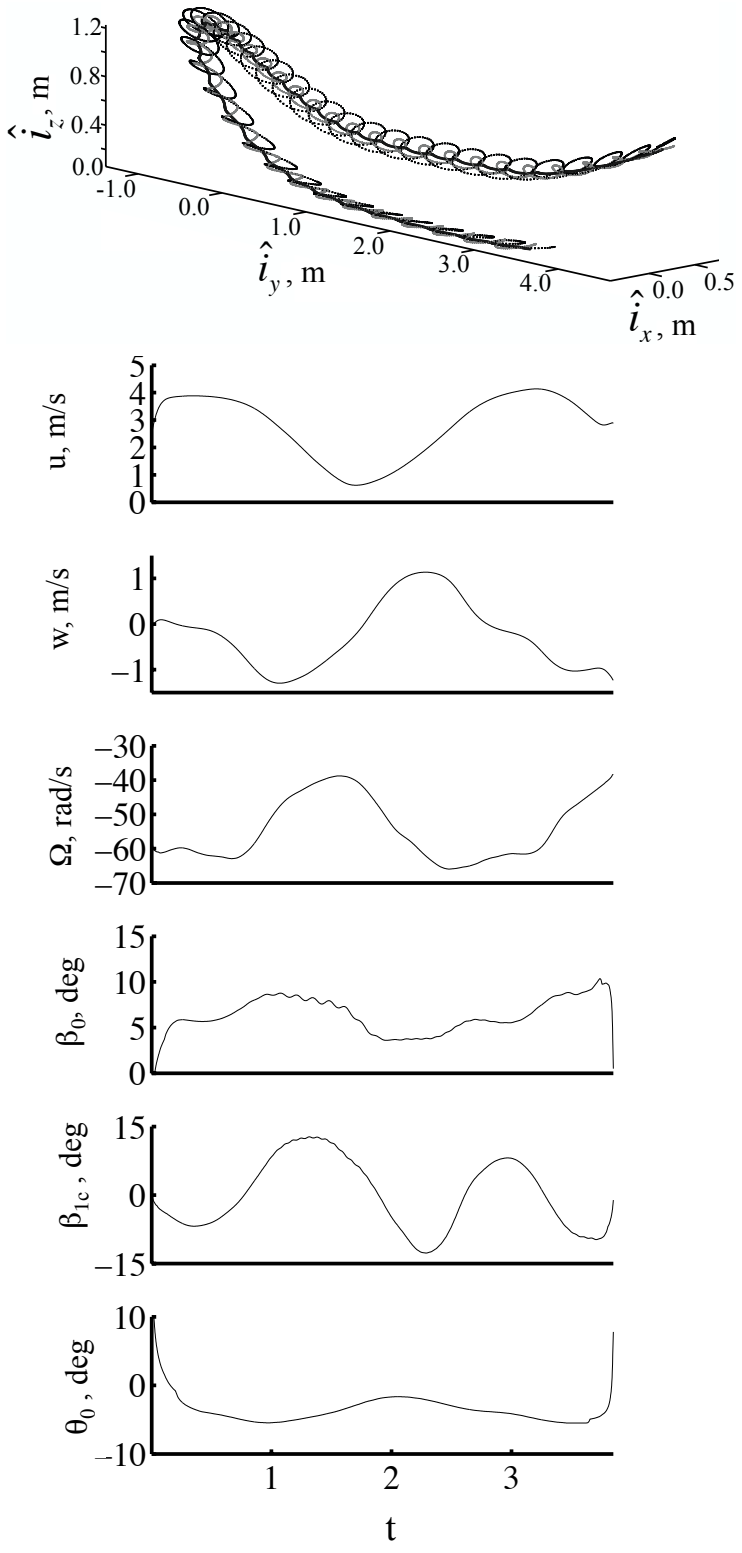

Figure 5.8: State trajectories in a coordinated turn.

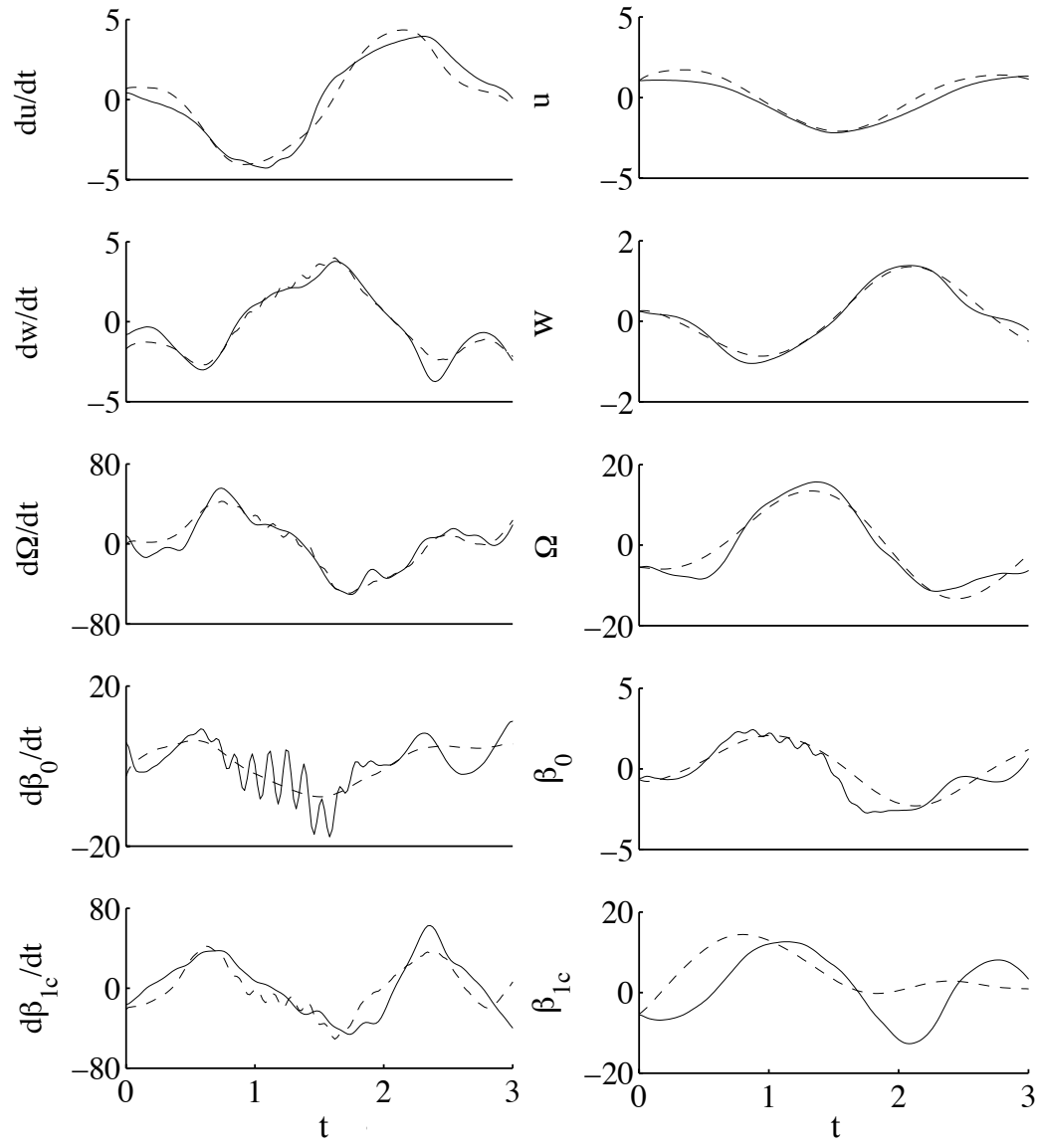

Figure 5.9: Equation-error and output-error model fit to perturbation data. Measurements are plotted with the solid line, and model outputs are plotted with a dashed line.

Chapter 6

Conclusions and Future Recommendations

6.1 Conclusion

Micro/Nano scaled aerial locomotion is one of the remaining frontiers of flight that mankind has yet to master. Among the myriad of natural fliers, insects and birds exhibit an impressive combination of size, endurance and control. Fast sensing, computation and actuation are required for this manner of flight and historically have each been a hurdle in creating a mechanical analogue. Not all natural fliers require brain power and many moving parts to stay aloft. In the case of autorotating plant seeds, uncontrolled and unpowered flight is key to the species survival. This natural rotorcraft is the basis for a new paradigm of micro/nano scaled flight vehicles that are mechanically simple and have limited sensing and actuation capabilities. Open loop directional control is possible with the use of alternating step and low-frequency input to the collective pitch of the wing at a frequency 1/10 that of the rotation rate.

This dissertation sought to design, construct and control a nano-air-vehicle based on natural autorotating plant seeds. Rigorous study of natural systems geometry,

mass properties, and airfoil characteristics led to design and fabrication of scaled up mechanical samara. The test specimens are constructed of an ultraviolet-cured liquid polymer, which is dispensed and cured via the use of a rapid prototyping machine. The results of these experiments identify a geometry for a minimal descent rate as well as producing a quantitative Fourier series representation of the roll and pitch. A new relationship has been established which elucidates trends in samara descent velocity not captured by wing loading or disk loading. Additionally, the experiments yielded observation of two modes of flight in autorotating mechanical samaras. The different flight modalities provided the basis for the design of a control system for a powered robotic samara that does not require the high frequency sensing and actuation typical of micro-scaled rotorcraft.

The two flight modalities identified differ in descent velocity, coning/feathering angle as well as roll, pitch and yaw rate. A prototype mechanical samara with a variable wing pitch angle was constructed and it was found that active control of the feathering angle allowed the variation of the radius of the helix carved by the samara upon descent. This knowledge was used to design a hover capable robotic samara capable of lateral motion through a series of different size circles specified by precise actuation of the feathering angle. Inspection of the flight dynamics reveals substantial similarities in the behavior of the passive descending samara and the powered robotic samara. The trend shared by the passive and powered vehicles is that non-cyclic decrease of the mean wing pitch angle increases both the radius of the circular path and the one-per-revolution amplitude of the wing pitch.

System identification techniques were used to create, from flight data, a linear model describing the heave dynamics of two robotic samara vehicles. A visual positioning system was used to collect flight data while the vehicles were piloted in an indoor laboratory. Eigenvalues of the heave dynamic model were estimated by two system identification packages. The identified parameters were used in simulating

the vehicles response to heave and collective input perturbations, as well as in the development of a PID controller. Closed-loop implementation of the derived controller was demonstrated using the visual tracking system for position and velocity feedback. The characteristically underdamped response to a descent maneuver was found, which differs from the critically damped response to an ascent maneuver.

An approach to directional control that does not require the once-per-revolution actuation or high-frequency measurement of vehicle orientation has been demonstrated for the first time. Lateral flight is attained through the vehicles differing responses to impulsive and step inputs that are leveraged to create a control strategy that provides full controllability. Flight testing revealed several linear relationships, including $[r_{turn}; u_{turn}]$ and $[r_{turn}; \dot{\psi}]$. The steady turn discussed here has been observed in scaled versions of the robotic samara, therefore the open-loop control demonstrated and analyzed is considered to be appropriate for similar vehicles of reduced size with limited sensing and actuation capabilities.

The nonlinear Euler equations were used to describe the rigid-body dynamics of the vehicle in a steady turn and are then extended to forward flight and linearized about a trim state, resulting in five linearized small perturbation equations in state-space form. Flight tests provided high-accuracy position information, which was reduced to wing flap angles and virtual-body velocities, was used to specify a flight condition that fit within the limits of the derived model and allowed for estimation of the vehicles stability derivatives. The dynamics of the robotic samara during a coordinated turn were shown to be well approximated by a linearized model.

6.2 Future Recommendations:

The robotic samara has a number of unknowns which if characterized could lead to performance enhancement and an understanding of the scaling laws as they apply

to both larger and smaller versions of the aircraft.

Additionally for fully autonomous flight the vehicle must be equipped with a means of determining orientation. Given the fast spin rate of the vehicle, a typical commercial rate gyro will saturate and be useless. Accelerometers can detect the rotational acceleration and therefor the rotation rate. An estimate of the azimuth angle can be attained by use of a magnetometer. Cyclic control requires knowledge of the orientation and would be possible with this combination of sensors with an embedded microprocessor to compute the control commands and navigate.

Moving forward, this new type of simple and robust vehicle spawns a number of applications not previously possible. The primary advantage of a robotic samara is in its ability to passively convert wind gusts and jet streams into lift for long range directional control. A larger vehicle with flexible solar panels and large battery stores could remain aloft indefinitely whilst confined to the jet stream. This creates the possibility of having low altitude satellite networks circumnavigating the globe amidst the jet stream, as seen in Figure 6.1.

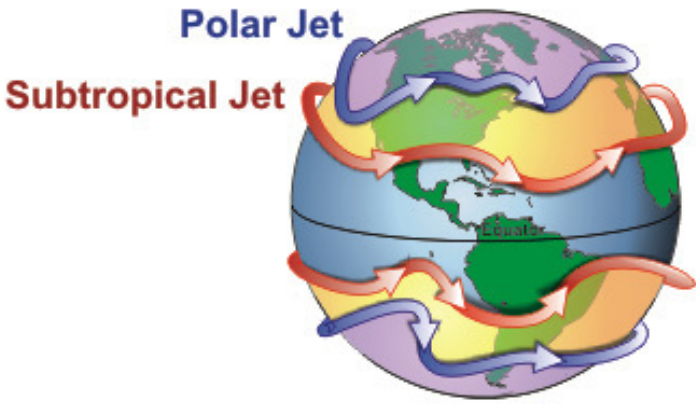

Figure 6.1: Jet stream.

Other applications include the use of samara-type vehicles for the study of large scale weather systems like tropical storms that lead to the formation of hurricanes. Weather is driven by a complex interaction between the ocean and the atmosphere and the collection of *in situ* data is crucial to improving weather prediction. Ocean-

atmosphere coupling in the tropical oceans drive weather patterns globally through teleconnections. Understanding of these interactions has been improved through satellite measurements that provide high spacial resolution. The error associated with the parameters estimated from satellite measurements can be reduced by reducing errors in the measurements used to calibrate the instruments on-board the satellite. High resolution wind profile measurements are possible with GPS enabled dropsonde devices, however the accuracy of the wind profile has been limited by the substantial descent rate of the dropsondes. This measurement uncertainty can be decreased by reducing the descent velocity so as to take more measurements of the vertical column, as well as allowing time for the sensors to respond to abrupt environmental variations. The proposed research seeks to improve *in situ* measurements of wind, temperature, humidity, and pressures. The data will fill a critical gap in the proposed Earth Observing System future science that fails to address the collection of wind measurements in the atmospheric boundary layer. This critical information can improve weather predictions associated with hurricane and tropical storm events potentially saving billions of dollars in false evacuations and more importantly potentially saving lives if the call to evacuate comes in time.

Bibliography

[1] Ward-Smith, A. J. " Biophysical Aerodynamics and the Natural Environment," John Wiley and Sons, New York, 1984, pp. 53–70.

[2] Pines, D. and Bohorquez, F., "Challenges Facing Future Micro-Air-Vehicle Development," *Journal of Aircraft*, Vol. 43, No. 2, 2006, pp. 290–305.

[3] Dickenson, M. H., "Solving the Mysteries of Insect Flight," *Scientific American*, Vol. 284, No. 6, 2000, pp. 49–57.

[4] Bohorquez, F., Samuel, P., Sirohi, J., Pines, D., Rudd, L., and Perel, R., "Design, Analysis and Hover Performance of a Rotary Wing Micro Air Vehicle." *Journal of the American Helicopter Society*, Vol. 48, 2003, pp. 80–90.

[5] Leishman, J.G., *Principals of Helicopter Aerodynamics*, Cambridge University Press, 2006, pp. 352–356.

[6] Kim, J., and Koratkar, N., "Effect of Unsteady Blade Pitching Motion on Aerodynamic Performance of Microrotorcraft", *Journal of Aircraft*, Vol. 42, No. 4, 2005, pp. 874–881.

[7] Yongsheng Lian, Wei Shyy, "Laminar-Turbulent Transition of a Low Reynolds Number Rigid or Flexible Airfoil AIAA Journal, Vol. 45, No. 7, 2007.

[8] Tsuzuki, N., "A Study on a Miniature Rotary-Wing Vehicle for Mars Exploration: Its feasibility and Aerodynamic characteristics of the Rotor", PhD Thesis, Dept. of Aeronautics and Astronautics, University of Tokyo, 2005.

[9] L. Van der Pijl, *Principles of Dispersal in Higher Plants*, Springer-Verlag, Berlin, ed. 3, 1982.

[10] Lugt, H. J., "Autorotation," *Annual Review of Fluid Mechanics*, 1983, Vol. 15, pp. 123–147.

[11] R. Nathan et al., "Mechanisms of long-distance dispersal of seeds by wind," *Nature* 418, 409 2002.

[12] R. Nathan, "Long-distance dispersal of plants," *Science* 313, 786 2006.

[13] McCutchen, C.W., "The Spinning Rotation of Ash and Tulip Tree Samaras," *Science*, 1977, Vol. 197, pp. 691–692.

[14] Green, D. S., "The Terminal Velocity and Dispersal of Spinning Samaras." *Amer. J. Bot.*, Vol.67, No. 8, 1980, pp. 1218–1224.

[15] Azuma, A., *The Biokinetics of Flying and Swimming* Tokyo: Springer- Verlag, 1992, pp. 105–121.

[16] Azuma, A., Yasuda, K., "The Autorotation Boundary of the Flight of Samaras," *Journal of Theoretical Biology*, 1997, pp. 313–320.

[17] Norberg, R. A., "Autorotation, self-stability, and structure of single-winged fruits and seeds (samaras) with comparative remarks on animal flight." *Biol. Rev.*, Vol. 48, 1973, pp. 561–596.

[18] Burrows, F. M., "Wing-Borne Seeds and Fruit Movement," *Journal of New Phytologist*, 1975, 75: 405–418.

[19] Stevens, B. L. and Lewis, F. L., *Aircraft Control and Simulation*, John Wiley and Sons, Inc., Hoboken, New Jersey 2003, pp 25–27.

[20] Seter, D., Rosen, A., "Stability of the Vertical Autorotation of a Single-Winged Samara," *Journal of Applied Mechanics*, 1992, pp. 1064–1071.

[21] Seter, D., Rosen, A., "Vertical Autorotation of a Single-Winged Samara," *Journal of Applied Mechanics*, 1991, pp. 1000–1008.

[22] Jameson, S., Allen, N.,Youngren, H., "SAMARAI Nano Air Vehicle - A Revolution in Flight." DARPA contract W31P4Q-06-C-0324, 2007.

[23] Kellas, A., "The guided Samara: Design and Development of a Controllable Single-Bladed Autorotating Vehicle," Master's Thesis, Massachusetts Institute of Technology, Sept. 2007.

[24] Lentink, D., et al. "Leading-Edge Vortices Elevate Lift of Autorotating Plant Seeds", *Science* 324, 1438, 2009.

[25] Crimi, P. "Analysis of a Samara-Wing Decelerator Steady State Characteristics," *Journal of Aircraft*, Vol. 25, No 1, 1988, pp. 41–47.

[26] Graham, F. *Monocopters*, Perigee Press, East Liverpool Ohio 1999.

[27] http://www.objet.com/3D-Printer/Eden350_Eden350V/

[28] http://www.objet.com/Docs/FullCure_3D%20Modeling_Letter.pdf

[29] http://www.vicon.com/_pdfs/t_cameras.pdf

[30] Ulrich, E., Pines, D., "Effects of Planform Geometry on Mechanical Samara Autorotation Efficiency and Rotational Dynamics" *Journal of the American Helicopter Society*, Vol. 57, 012003 2012.

[31] Johnson, W., Helicopter Theory, Princeton University Press, Princeton, NJ, 1980.

[32] Leishman, J.G., *Principals of Helicopter Aerodynamics*, Cambridge University Press, 2006, pp. 160–190.

[33] Benedict, M., Ramasamy, M., Chopra, I., Leishman, J.G., "Performance of a Cycloidal Rotor Concept for Micro Air Vehicle Applications," *Journal of the American Helicopter Society*, Vol. 55, 2010.

[34] Mayo, D., Leishman, J.G., "Comparison of the Hovering Efficiency of Rotating Wing and Flapping Wing Micro Air Vehicles" *Journal of the American Helicopter Society*, Vol. 55, 2010.

[35] Josephson, R. K., "Power Output from a Flight Muscle of the Bumblebee Bombus, III. Power during Simulated Flight," *Journal of Experimental Biology*, Vol. 200, 1997, pp. 1241–1246.

[36] Lehmann, FO., and Dickinson, M. H., "The Challenges in Power Requirements and Muscle Efficiency During Elevated Force Production in the Fruit Fly Drosophila, *Journal of Experimental Biology*, Vol. 200, 1997, pp. 1133–1143.

[37] Norberg, U. M., Steffensen, J. F., Winter, Y., and Von Versen, O., "The Cost of Hovering and Forward Flight in a Nectar-Feeding Bat, Glossophega soricina, Estimated from Aerodynamic Theory, *Journal of Experimental Biology*, Vol. 182, 1993, pp. 207–227.

[38] Singh, B., and Chopra, I., "Insect-Based Hover-Capable Flapping Wings for Micro Air Vehicles: Experiments and Analysis, *AIAA Journal*, Vol. 46, No 9, 2008, pp. 2115–2135.

[39] Ulrich, E.R., Humbert, J.S., Pines, D., "From Falling to Flying: The Path to Powered Flight of a Robotic Samara Nano Air Vehicle," *Journal of Bioinspired Biomimetics*, Vol. 5, 2010.

[40] Grasmeyer, J., and Keenon, M., "Development of the Black Widow Micro Air Vehicle, AIAA Paper 2001-0127, Jan. 2001.

[41] Samuel P., Sirohi, J., Bohorquez, F., Couch R. "Design and Testing of a Rotary Wing MAV with an Active Structure for Stability and Control." AHS 61st Annual Forum, Grapevine, TX, 1-3 June 2005.

[42] Samuel, P., Sirohi, J., Rudd, L., Pines, D., and Perel, R., "Design and Development of a Micro Coaxial Rotorcraft, Proceedings of the AHS Vertical Lift Aircraft Design Conference, American Helicopter Society, Alexandria, VA, Jan. 2000.

[43] Bohorquez, F., Samuel, P., Sirohi, J., Pines, D., Rudd, L., and Perel, R., "Design, Analysis and Hover Performance of a Rotary Wing Micro Air Vehi- cle, *Journal of the American Helicopter Society*, Vol. 48, No. 2, Apr 2003, pp. 80–90.

[44] Hrishikeshavan, V., Sirohi, J., Tishchenko, M., Chopra, I., "Design, Development, and Testing of a Shrouded Single-Rotor Micro Air Vehicle with Antitorque Vanes" *Journal of the American Helicopter Society*, Vol. 56, 012008, 2011.

[45] Keennon, M., Klingebiel, K., Won, H., and Andriukov, A., "Development of the Nano Hummingbird: A Tailless Flapping Wing Micro Air Vehicle" 50th AIAA Aerospace Sciences Meeting AIAA 2012-0588 Jan. 2012.

[46] Ulrich, E.R., Pines, D., "Planform Geometric Variation, and its Effect on the Autorotation Efficiency of Mechanical Samara," American Helicopter Society 64th Annual Forum, 2008, Vol. 2, pp. 1138.

[47] Ulrich, E.R., Pines, D., Humbert, J.S., "Pitch and Heave Control of Robotic Samara Micro-Air-Vehicles," *Journal of Aircraft*, Vol. 47, No. 4, July 2010.

[48] Barlow, J. B., *Low-Speed Wind Tunnel Testing* John Wiley and Sons, Inc., Hoboken, New Jersey 1999.

[49] Albertani, R., et al. "Validation of a Low Reynolds Number Aerodynamic Characterization Facility," AIAA-2009-880, 2009.

[50] Ulrich, E., Pines, D., Park, J., "Mechanical Samara Deployment and Passive Distribution by a Fixed Wing Unmanned Air Vehicle," AHS International Specialist Meeting on Unmanned Rotorcraft, Phoenix, AZ, January 2009.

[51] Ulrich, E., Faruque, I., Grauer, J., Pines, D., Humbert, J.S., Hubbard, J. "Control Model for Robotic Samara: Dynamics about a Coordinated Helical Turn" American Controls Conference, Baltimore, MD, June 2010.

[52] Conroy, J., Humbert, J.S., Pines, D. "System Identification of a Rotary Wing Micro Air Vehicle," *Journal of the American Helicopter Society*, Vol. 56, No. 2, 2011.

[53] Tischler, M., Remple, R. "Aircraft and Rotorcraft System Identification: Engineering Methods with Flight Test Examples." AIAA, 2006.

[54] Mettler, B., Tischler, M., "System identication of small-size unmanned helicopter dynamics" AHS 55th Forum, 1999.

[55] Baruh, H.,*Analytical Dynamics*, McGrawHill, New York, 1999.

[56] Brodsky, A. K., The Evolution of Insect Flight, Oxford Univ. Press, New York, 1994, pp. 51.

[57] McMasters, J. H., and Henderson, M. L., "Low Speed Single Element Airfoil Synthesis," Technical Soaring, Vol. 6, No. 2, 1980, pp. 1–21.

[58] Klein, V. and Morelli, E., *Aircraft System Identification: Theory and Practice* , AIAA Education Series, American Institute of Aeronautics and Astronautics, Reston, VA, 2006, Chapter 4.

[59] Hochmann, D. and Sadok, M., "Theory of Synchronous Averaging," IEEE Aerospace Conference Proceedings, Institute for Electrical and Electronics Engineers, 2004, pp. 3636–3653.

[60] Samuel, P. and Pines, D., "Helicopter Transmission Diagnostics using Constrained Adaptive Lifting," American Helicopter Society 59th Annual Forum Proceedings, Phoenix, AZ, May 2003.

[61] "Defense Sciences Office Nano Air Vehicle," Tech, Rep. W31P4Q-06-C-0324, DARPA, September 2009.

[62] Keennon, M. T., and Grasmeyer, J. M., "Development of the Black Widow and Microbat MAVs and a Vision of the Future of MAV Design, AIAA 2003-2901, AIAA/ICAS International Air and Space Symposium and Exposition: The Next 100 Years, Dayton, OH, July 1417, 2003.